COLLOIDAL SILVER NANOCRYSTALS

AND THEIR DERIVATIVES:

SYNTHESIS, PROPERTIES, AND APPLICATIONS

A Dissertation
Presented to
The Academic Faculty

by

Yiren Wu

In Partial Fulfillment
of the Requirements for the Degree
Doctor of Philosophy in the
School of Materials Science and Engineering

Georgia Institute of Technology
May 2019

COLLOIDAL SILVER NANOCRYSTALS

AND THEIR DERIVATIVES:

SYNTHESIS, PROPERTIES, AND APPLICATIONS

Approved by:

Dr. Dong Qin, Advisor
School of Materials Science and Engineering
Georgia Institute of Technology

Dr. Vladimir Tsukruk
School of Materials Science and Engineering
Georgia Institute of Technology

Dr. Zhiqun Lin
School of Materials Science and Engineering
Georgia Institute of Technology

Dr. Angus Wilkinson
School of Chemistry and Biochemistry
Georgia Institute of Technology

Dr. Donggang Yao
School of Materials Science and Engineering
Georgia Institute of Technology

Date Approved: November 20th, 2018

Dedicated to my beloved parents and friends who are always with me.

ACKNOWLEDGEMENTS

First and foremost, I would like to express my deepest gratitude to my advisor, Professor Dong Qin, who has guided me throughout my thesis work with her enthusiasm, motivation, knowledge, and continuous support. She brought me into the world of nanomaterials and provided insightful guidance for my projects. I would like to extend my gratitude to Professor Vladimir Tsukruk, Professor Zhiqun Lin, Professor Donggang Yao, and Professor Angus Wilkinson for serving on my dissertation committee and providing all helpful and valuable suggestions to my thesis projects.

I am profoundly grateful to all the members of Qin lab and our collaborators. My special thanks go to Dr. Jumei Li and Dr. Yun Zhang, who were great collaborators and shared many hands-on experiences with me. I am also grateful to current and former group members, Jae Wan Ahn, Zheyu Luo, Shi Shi, Luo Zhang, Bonnie Vannatter, Dr. Xiaojun Sun, Daniel Wang, Jun Ki Kim, Nina Su, Dr. Jiawei Zhang, Zhiwei Zhang, Professor Sarah A. Winget, and Chia-Wei Wang, for their support, help and encouragement over the past four years. I sincerely appreciate the support from our collaborators, Professor Younan Xia, Dr. Dong Su, and Dr. Zhi-Yuan Li, for their input and contribution to the projects.

My sincere thanks go to my friends who are supportive and caring for me. My heartfelt thanks go to Yi Cao, who has always been there for me through my ups and downs. My special thanks go to Xiaohui Luo and Ashley Liu for their spiritual support.

Finally, I would love to express my special thanks to my parents, Jiangchen Wu and Xin You, for their endless love and unconditional support over the years.

TABLE OF CONTENTS

LIST OF TABLES

LIST OF FIGURES

LIST OF SYMBOLS AND ABBREVIATIONS

a	radius
AFM	atomic force microscopy
Ag	silver
$AgNO_3$	silver nitrate
Ag_2O	silver oxide
Al_2O_3	aluminum oxide
4-AP	4-aminophenol
4-ATP	4-aminothiophenol
Au	gold
1,4-BDT	1,4-benzenedithiol
χ	geometry factor
$CaCO_3$	calcium carbonate
CeO_2	cerium oxide
CHEM	chemical enhancement
Co	cobalt
CO	carbon monoxide
4-CPI	4-chlorophenyl isocyanide
CT	charge transfer
Cu	copper
DDA	discrete dipole approximation
DI	deionized
trans-DMAB	*trans*-4,4'-dimercaptoazobenzene

2,6-DMPI	2,6-dimethylphenyl isocyanide
ε_i	imaginary part of dielectric function
ε_m	dielectric constant of external medium
ε_r	real part of dielectric function
EDA	ethylenediamine
EDX/EDS	energy-dispersive X-ray spectroscopy
EELS	electron energy loss spectroscopy
EF	enhancement factor
E-fields	electromagnetic fields
EG	ethylene glycol
EM	electron microscopy
EM	electromagnetic enhancement
$E_{out}(\omega)$	incident excitation
$E_{out}(\omega\text{-}\omega_v)$	Stokes' shifted Raman electromagnetic fields
FDTD	finite difference time domain
Fe	iron
FEM	finite element method
$Fe(NO_3)_3$	iron nitrate
4-FNB	4-fluoronitrobenzene
γ	specific surface free energies
GC-MS	gas chromatography-mass spectrometry
HAADF-STEM	high-angle annular dark-field scanning transmission electron microscopy
$HAsc^-$	ascorbate monoanion
H_2Asc	ascorbic acid
$HAuCl_4$	chloroauric acid

HNO_3	nitric acid
H_2O_2	hydrogen peroxide
ICP-MS	inductively coupled plasma mass spectroscopy
$I_{NRS}(\omega_v)$	normal Raman intensity
Ir	iridium
$I_{SERS}(\omega_v)$	enhanced Raman intensity
λ	wavelength of the incident light
LSP	localized surface plasmon
LSPR	localized surface plasmon resonance
$NaBH_4$	sodium borohydride
NaOH	sodium hydroxide
Na_2PdBr_4	sodium tetrabromopalladate
Na_2PdCl_4	sodium tetrachloropalladate
ν	stretching frequency
NB	nitrobenzene
-NC	isocyanide group
Ni	nickel
NMR	nuclear magnetic resonance
4-NP	4-nitrophenol
N_{surf}	number of molecules bound to the metal surface
4-NTP	4-nitrothiophenol
N_{vol}	number of molecules in the excitation volume
NW	nanowire
PbS	lead sulfide

Pd	palladium
1,4-PDI	1,4-phenylene diisocyanide
PDMS	polydimethylsiloxane
PSP	propagating surface plasmon
Pt	platinum
PVP	poly(vinyl pyrrolidone)
R_{gal}	rate of galvanic replacement reaction
Rh	rhodium
R_{red}	rate of chemical reduction reaction
Ru	ruthenium
SAM	self-assembled monolayer
SAXS	small-angle X-ray scattering
SEM	scanning electron microscopy
SERS	surface-enhanced Raman scattering
SHE	standard hydrogen electrode
SiO_2	silicon dioxide
SnO_2	tin oxide
SP	surface plasmon
TEM	transmission electron microscopy
TEOS	tetraethyl orthosilicate
TERS	tip-enhanced Raman spectroscopy
TiO_2	titanium oxide
UV-vis	ultraviolet–visible
WAXS	wide-angle X-ray scattering
XPS	X-ray photoelectron spectroscopy

SUMMARY

Silver nanocrystals have received growing interests owing to their fascinating localized surface plasmon resonance (LSPR) properties and spectacular applications in surface-enhanced Raman scattering (SERS). Despite remarkable success, Ag nanocrystals are highly susceptible to oxidative etching and only exhibit limited catalytic activities. To address these issues, the first part of my thesis documents the development of synthetic approaches to enrich Ag nanocrystals with a second noble metal for the generation of Ag@Pd-Ag core-frame nanocubes and Ag@SiO_2/Au nanoparticles. I also demonstrated these bimetallic nanocrystals as bifunctional probes for *in situ* monitoring the catalytic reactions by SERS. In the second part of this thesis, I turned the synthesis of Ag@Pd-Ag core-frame nanocubes into a model system for investigating the heterogeneous nucleation in nanocrystal growth with a molecular probe. I demonstrated that 2,6-dimethylphenyl isocyanide was a sensitive probe for *in situ* atomic-level tracking of the heterogeneous nucleation of Pd on Ag nanocubes by SERS. I discovered that the isocyanide group could bind to one, two, and three adjacent Pd atoms to generate the atop, bridge, and hollow binding configurations, respectively, and give different vibrational frequencies, making it possible to characterize Pd atoms being deposited onto different facets of Ag nanocubes. This *in situ* SERS offers an opportunity to investigate the role of reaction temperature and the type of Pd(II) precursor in affecting the reduction, deposition, and surface diffusion involved in heterogeneous nucleation. Collectively, my thesis opens up new possibilities for the rational design and synthesis of bimetallic nanocrystals involving Ag and another noble metal such as Pt, Ru, Rh, and Ir.

CHAPTER 1. INTRODUCTION

1.1 Silver Nanocrystals

Silver is perhaps the best choice of material for plasmonics and related applications owing to its relatively low cost and favorable dielectric functions.[1] Among noble metals, Ag exhibits the highest electric and thermal conductivity. It has been widely used in photography,[2] electrical contacts,[3] coatings,[4] and catalysis in oxidation reactions.[5] Over the past two decades, significant progress has been made in the synthesis of Ag nanocrystals with controlled shapes and sizes to tailor their properties and thus optimize their performance in a range of applications.[6-7] In particular, because of its unique dielectric function satisfying the resonance condition of localized surface plasmon resonance (LSPR), Ag nanocrystals have been prepared with sharp features on the surface to drastically augment their surface-enhanced Raman scattering (SERS) activity,[8] and they have been used widely in the SERS, optical labeling, and near-field probing.[9-11] However, the sharp features tend to vanish due to the high susceptibility of Ag towards oxidative etching.[12] As another pitfall, Ag is limited in terms of catalytic application as it only shows activity towards oxidation reactions such as epoxidation,[13] not reduction reactions.

1.1.1 Plasmonic Properties of Silver Nanocrystals

1.1.1.1 Localized Surface Plasmon Resonance (LSPR)

In a noble metal, the collective oscillation of the free electrons is known as a plasmon. In fact, classic physics has been used to define the oscillation of bulk plasmons.[14] When a bulk metal shrinks to the size that is comparable to its mean-free path of electrons (~50 nm

for silver), plasmons would act in the form of surface plasmons (SPs). As illustrated in Figure 1.1, upon an optical excitation of an incident light, they can turn into standing or propagating surface plasmon modes through a grating or a defect at the metal surface.[14]

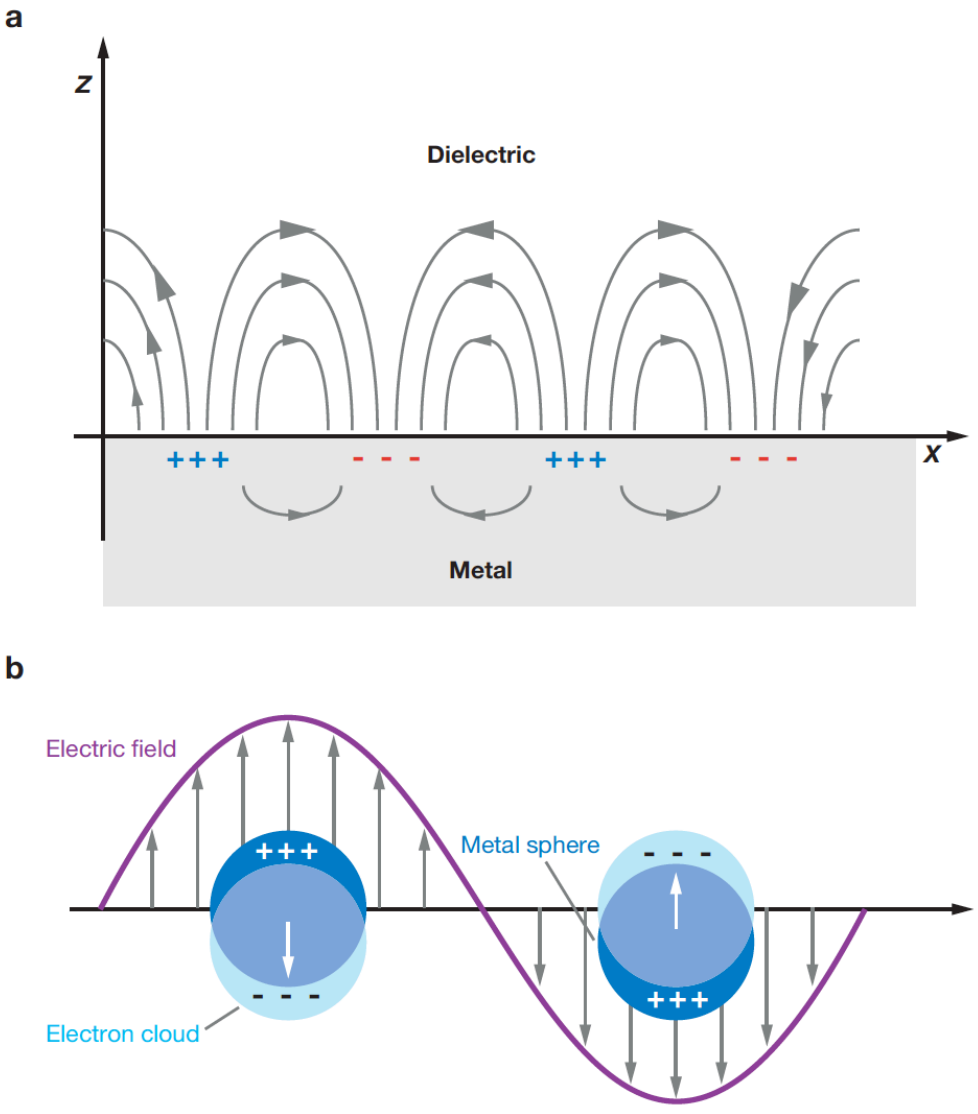

Figure 1.1. Schematic illustration of (a) propagating surface plasmon and (b) localized surface plasmon. Copyright 2007 Annual Reviews.[19]

When the nanoparticles have at least one dimension larger than the wavelength of the incident light, the plasmons would propagate across the metal surface, which is known as propagating surface plasmons (PSPs) (Figure 1.1A). Alternatively, when the size of nanoparticles is much smaller than the wavelength of light, the surface plasmons are confined within the particles, creating localized surface plasmons (LSPs) (Figure 1.1B). When the free electrons oscillate collectively in resonance with incident light at a certain wavelength, localized surface plasmon resonance (LSPR) is achieved.

In 1908, Gustav Mie developed an analytical description of scattering and absorption of light by spherical particles.[15] Although the Mie theory has been used to calculate the extinction cross section of a metal nanosphere and thus elucidate the contribution from absorption and scattering, its utility has been limited to spherical particles only. In 1912, Richard Gans extended the model to spheroidal particles using small particle approximation.[16] He established the Gans theory for the description of the cross sections of a prolate spheroid, which involved the consideration of particle geometry.

When the nanoparticle is dissembled to N finite polarizable elements interacting with the applied electric field, the extinction spectrum of the metal nanosphere is defined as[15, 17-19]

$$\mathrm{E}(\lambda) = \frac{24\pi^2 N a^3 \varepsilon_m^{3/2}}{\lambda \ln(10)} \left[\frac{\varepsilon_i(\lambda)}{(\varepsilon_r(\lambda) + \chi\varepsilon_m)^2 + \varepsilon_i(\lambda)^2}\right] \quad (1.1)$$

where a represents the radius of the sphere, ε_m is the dielectric constant of the external medium, λ is the wavelength of the incident light, ε_r and ε_i are the real and imaginary components of the metal dielectric function. The value of factor χ, strongly depends on the

geometry of the particle. In the case of spheres, χ equals 2; for the geometry with higher aspect ratio, χ takes larger values.

Based on Equation 1.1, the extinction will be maximized if $\varepsilon_r(\lambda)=-\chi\varepsilon_m$ in the denominator is attained, suggesting that extinction would strongly depend on the dielectric function of materials and the dielectric constant of the medium (Figure 1.2).[14] It is also worth mentioning that the imaginary component of the dielectric function ε_i is related to plasmon damping. Strong resonance would occur when the imaginary part is close to zero.

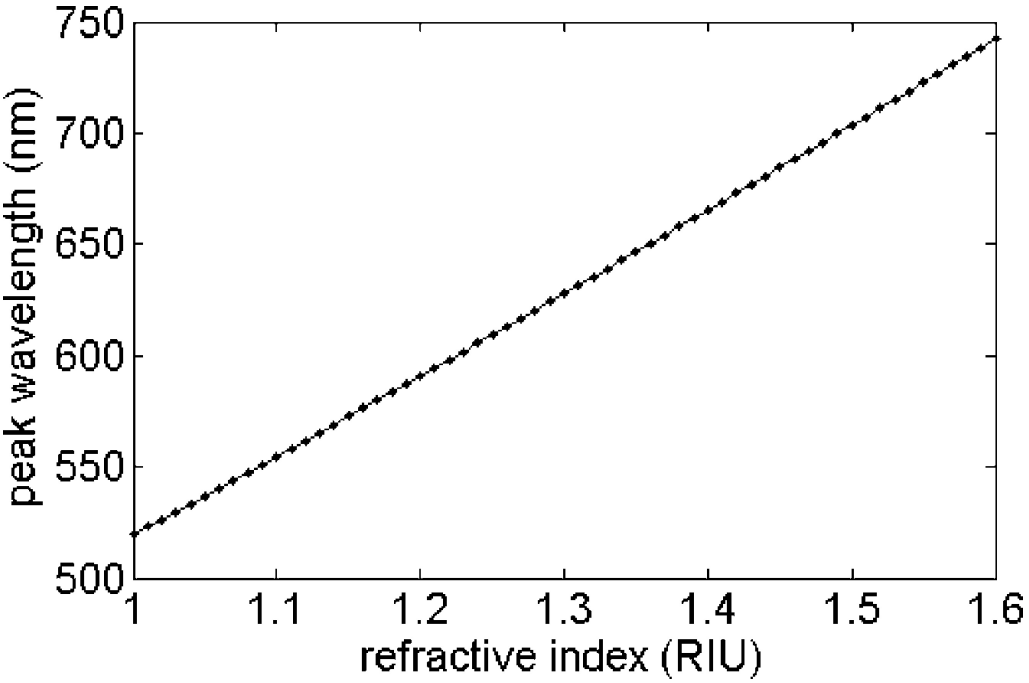

Figure 1.2. The linear dependence of LSPR peak wavelength on the refractive index of the medium surrounding the metal, based on the Drude model. Copyright 2011 American Chemical Society.[14]

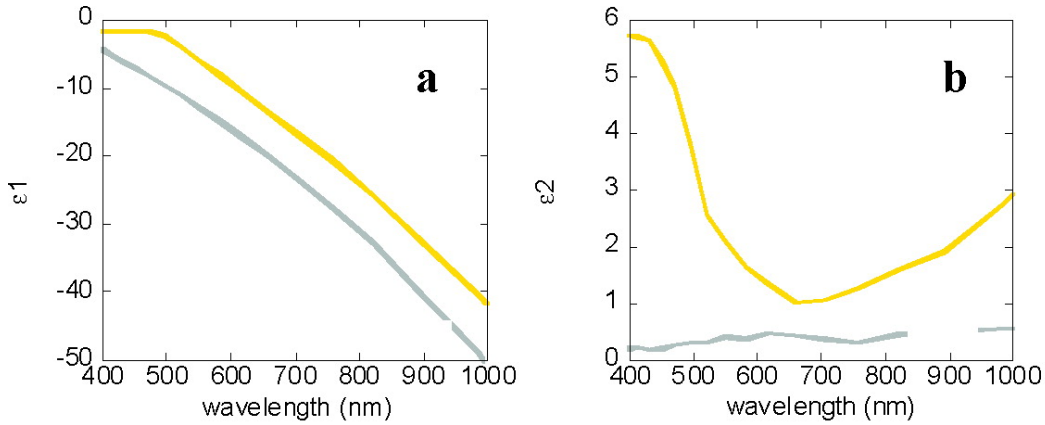

Figure 1.3. Dielectric function of Ag (lower) and Au (upper) as a function of wavelength: (a) real component and (b) imaginary component. Copyright 2011 American Chemical Society.[14]

Figure 1.3, A and B, gives the dielectric function of bulk silver and gold over a broad range of wavelength from 400 nm to 1000 nm.[14] Unlike standard dielectrics of other materials with ε_r values between 1 and 50,[20] ε_r of Ag and Au exhibits a negative value, which is essential for reaching the resonance condition. Additionally, the imaginary component of Ag is close to zero, which naturally satisfies the resonance condition. To this end, Ag is able to support a strong surface plasmon over the spectrum from 300 to 1200 nm. In comparison, Au has an inter-band transition located around 500 nm, making it only available to support the LSPR excitation at longer excitation wavelength.[21] Because Au is resistant to oxidation with an excellent biocompatibility, it remains a great choice for plasmonic applications. To extend the LSPR properties of Au nanoparticles to the wavelength below 500 nm, El-Sayed and his coworkers have done a careful study to tune the LSPR peak positions of Ag/Au alloys nanoparticles by changing their compositions.[22]

As shown in Figure 1.4, they successfully demonstrated the linear dependence of the LSPR peak position as function of Au mole fraction.[22]

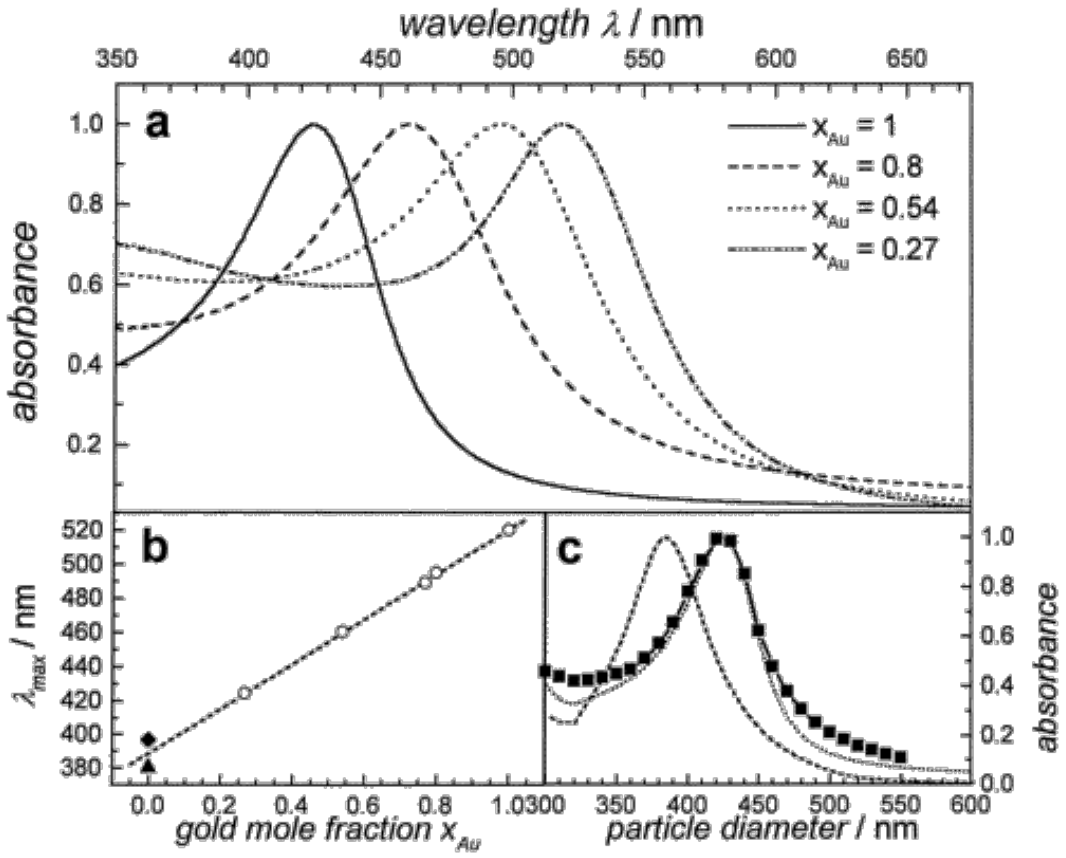

Figure 1.4. (a) Plasmon resonance peak of Ag-Au alloy nanoparticles with different composition. (b) Linear relationship between gold mole fraction and LSPR peak position. (c) Experimental and simulated spectra of the alloyed nanoparticles. Copyright 1999 American Chemical Society.[22]

In additional to the composition of materials, the size and shape of the nanoparticles would have a significant impact on the LSPR property. Figure 1.5 shows the calculated

and experimental spectra of Ag and Au nanospheres with different diameters.[23] In practice, for the nanoparticles beyond spheres and spheroids, numerical methods such as finite difference time domain (FDTD),[24] discrete dipole approximation (DDA),[25] and finite element method (FEM)[26] have been developed. Figure 1.6 gives a comparison of extinction spectra of Ag sphere, cube, octahedron, and right bipyramid from experimental and calculation data based on the Mie theory and the DDA method, respectively.[1]

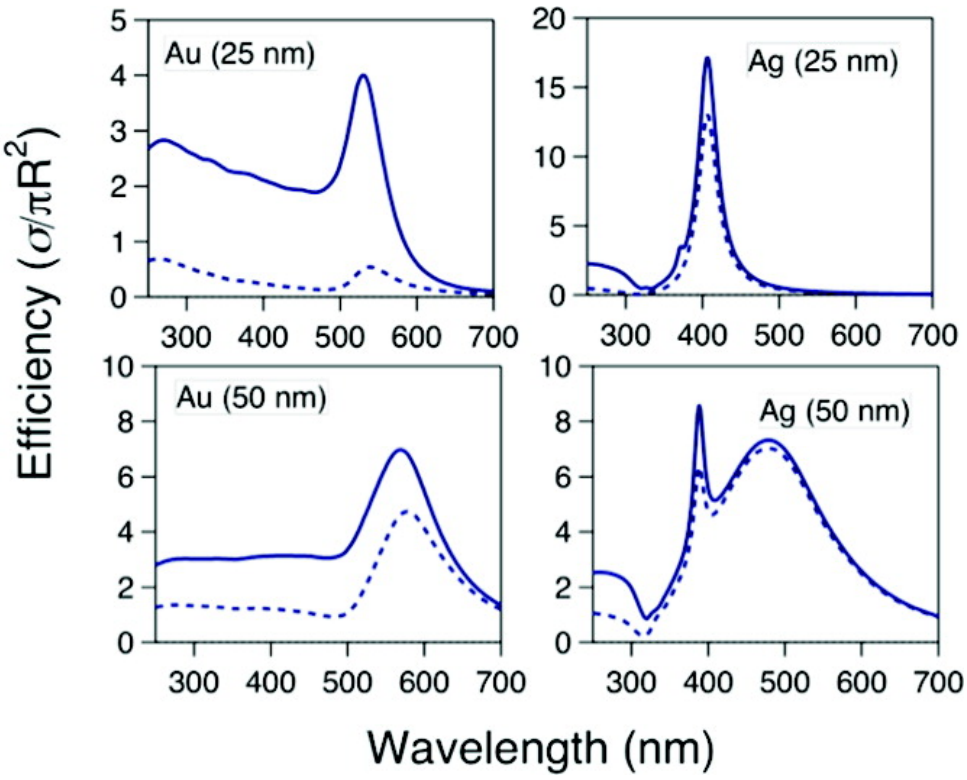

Figure 1.5. Calculated extinction (solid line) and scattering spectra (dash line) for Ag and Au nanoparticles with different sizes in the medium of water. Copyright 2011 American Chemical Society.[23]

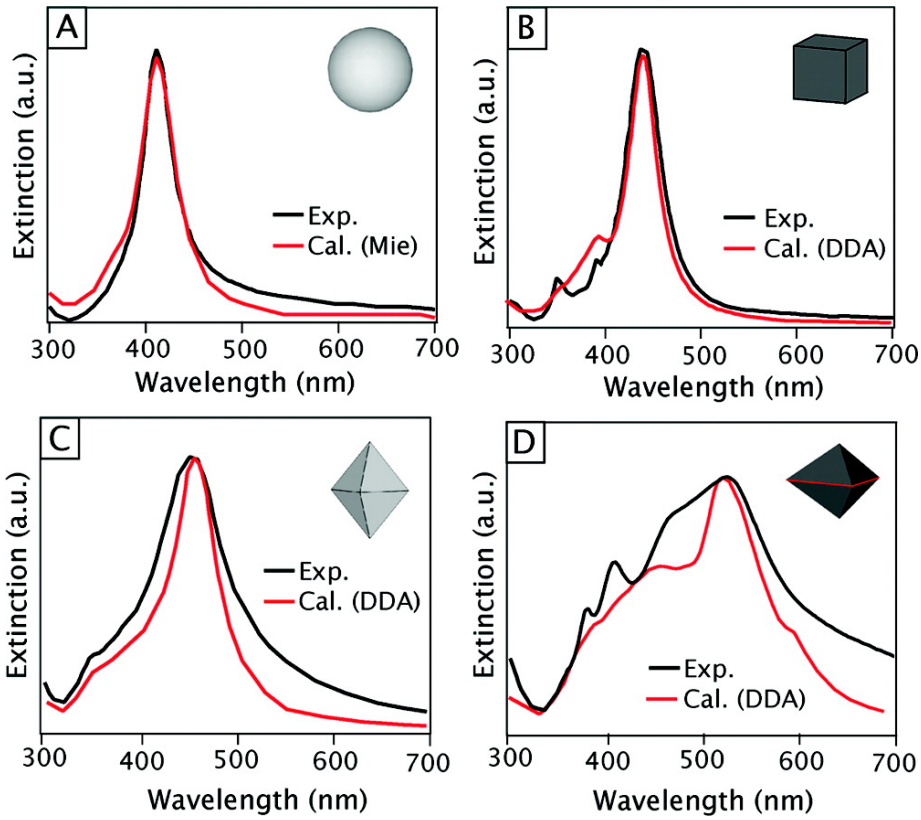

Figure 1.6. The experimental (black) and calculated (red) extinction spectra of (A) Ag spheres with a diameter of 40 nm; (B) cubes with an edge length of 40 nm; (C) octahedrons with an edge length of 40 nm; and (D) right bipyramids with an edge length of 75 nm. Copyright 2011 American Chemical Society.[1]

1.1.1.2 Surface-Enhanced Raman Scattering (SERS)

Surface-enhanced Raman scattering (SERS) is a near-field phenomenon by which the Raman signals of molecules are amplified due to the electromagnetic interaction of light with metals. To achieve SERS, the probe molecules need to be adsorbed onto the metal surface in the proximity of the interaction regime.[27] At the plasmon resonance, the amplification could go up to several orders of magnitude comparing to the original scattering. Based on inelastic Stokes-Raman scattering of the molecules, Raman

spectroscopy provides the "fingerprint" information of molecules from their vibrational transitions. Since the discovery by Van Duyne and Fleischmann in the early 1970s,[28-29] SERS has become a powerful technique for the detection of molecules adsorbed on the surface of metals with sensitivity.[27]

In a typical SERS measurement, enhancement factor (EF) is often used to quantify the effect of the amplification by using the following equation:[30-31]

$$EF_{SERS}(\omega_\upsilon)=\frac{\left|E_{out}(\omega)^2\right|\left|E_{out}(\omega-\omega_\upsilon)^2\right|}{E_0^4}=\frac{[I_{SERS}(\omega_\upsilon)/N_{surf}]}{[I_{NRS}(\omega_\upsilon)/N_{vol}]} \qquad (1.2)$$

where $E_{out}(\omega)$ and $E_{out}(\omega-\omega_\upsilon)$ are the incident excitation and the resulting Stokes' shifted Raman electromagnetic fields, respectively. In practice, EF is calculated by the enhanced Raman intensity $I_{SERS}(\omega_\upsilon)$, the number of molecules bound to the metal surface N_{surf}, the normal Raman intensity $I_{NRS}(\omega_\upsilon)$, and the number of molecules in the excitation volume N_{vol}. The major challenge in calculating EF arises from the challenges in the accurate estimation of the number of molecules adsorbed on the surface.

In literature, there are four proposed mechanisms accounting for the Raman enhancement (Figure 1.7).[1, 32-36] The first mechanism is defined as chemical enhancement (CHEM), which is due to the non-resonant interactions between the adsorbate and the metal (Figure 1.7A). The second mechanism is known as the resonance mechanism when the incident light is in resonance with the molecular excitation (Figure 1.7B). Thirdly, charge transfer mechanism (CT) occurs due to the resonance of the incident light and the excitation from metal to the molecule adsorbed on the surface (Figure 1.7C). Electromagnetic

mechanism (EM), which results from the resonance of the incident beam with the surface plasmons on the metal, usually plays the most significant role in SERS (Figure 1.7D). The EM mechanism is considered to contribute most of the enhancement by 10^5 to 10^8, while other mechanisms contribute only by 10 to 10^3.[1, 36] It is worth mentioning that the EF is often a sum of contributions from these four different mechanisms.

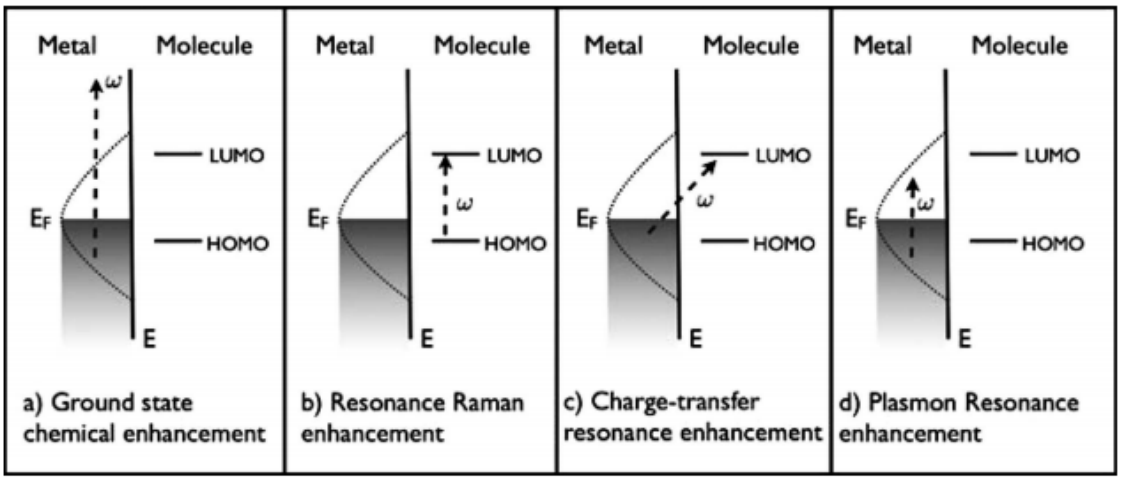

Figure 1.7. Schematic illustration of different enhancement mechanisms for SERS. Copyright 2008 Royal Society of Chemistry.[33]

In my thesis work, I will focus on the LSPR and SERS properties of Ag nanocubes with their dimensions described in Figure 1.8A. Based on the finite element method (FEM), Figure 1.8B shows the calculated E-field strength distribution of the nanocube.[37] Because the edges of a Ag nanocube, including the regions on Ag {100} and Ag {111}, would embrace the electromagnetic field enhancement, it is anticipated that these sites could serve

as hot spots to significantly enhance the Raman cross-section of molecules in proximity. Figure 1.8C shows the simulation results of two Ag nanocubes situated side by side with a narrow gap. While the edges of nanocubes are still remained as the enhanced regions, two nanocubes would create an interparticle hot spot within the gap.

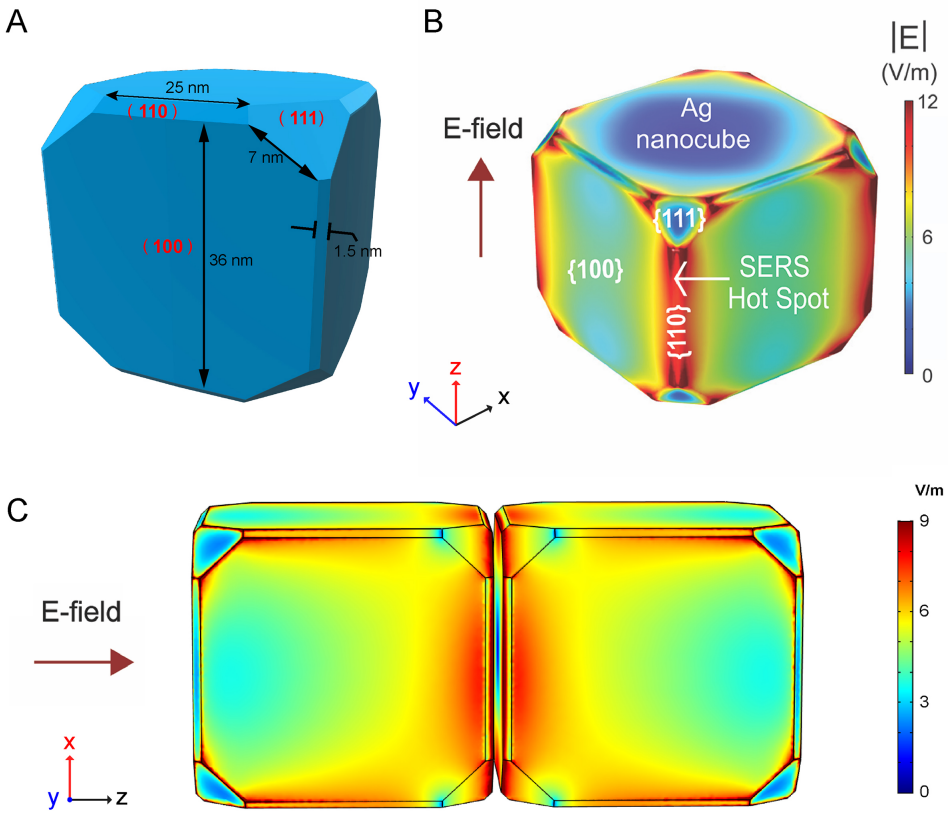

Figure 1.8. (A) Schematic illustration of a 39-nm Ag nanocube enclosed by {100}, {111}, and {110} facets. (B) Plot of electric field on the surface of a single Ag nanocube with edge length of 39 nm calculated by finite element method. (C) Plot of electric field on the surface of two Ag nanocubes with edge length of 39 nm situated side by side with a 1.2 nm gap.

1.1.2 Catalytic Activities of Ag Nanocrystals

Different from the other noble metals such as palladium or platinum with ability to catalyze reduction reactions, silver has been extensively utilized as a catalyst for oxidation reactions.[5, 38-40] For instance, silver catalyst has been commercial available for the oxidation of ethylene to ethylene oxide,[41-44] which provides important chemical reagents for organic chemistry synthesis. The catalytic activities have also been extended to oxidation of olefins, including direct epoxidation of propylene[45-46] and oxidation of styrene.[47-48] The other reactions catalyzed by silver include oxidation of methanol,[5] the production of hydrogen from ammonia borane,[49] oxidation of nitroaromatics,[50] and electroreduction of carbon dioxide to carbon monoxide (CO).[51]

1.2 Synthesis of Bimetallic and Hybrid Nanocrystals

1.2.1 Synthesis of Silver Nanocrystals

The dielectric function of Ag has made itself a perfect material to naturally fit into the resonance condition for LSPR. Because the size and shape of Ag nanostructures would affect their plasmonic properties, the morphology-controlled synthesis of Ag nanocrystals is of great importance. Many groups have demonstrated the generation of Ag nanocrystals with controlled sizes and shapes with various routes that include wet chemical synthesis, template-directed growth, and lithographic fabrication.[1] Among those, wet chemical synthesis is the most commonly used method due to the easy procedure and low cost. In a typical process, one could start with a reduction reaction of a silver precursor by a reducing agent to generate Ag clusters, followed by the nucleation and growth into desired shape and size in presence of a capping agent and a stabilizer. For example, the syntheses of Ag

nanocrystals rely on several different reactions, including (but not limited to) citrate reduction,[52-53] silver mirror reaction,[54-55] polyol process,[6-7, 56] seeded growth,[57-59] and light-mediated growth.[60-62]

The polyol process involves a Ag precursor, a stabilizer, and a polyol acting as both a solvent and a reducing agent. The polyol, for instance, ethylene glycol (EG), would turn into a strong reductant when heated with oxygen. Initially, the Ag clusters formed in the early stage would nucleate into single crystalline, single twinned, or multiply twinned "seeds" with which they could further grow into different shapes in presence of a capping agent to maneuver the surface energies of crystalline facets. Polyol method has been well documented in the literatures to produce Ag nanocubes, nanosheres, spheroids, plates, and wires.[1, 7, 63]

The LaMer model can be used to understand the shape-controlled synthesis of Ag nanocrystals (Figure 1.9).[6, 64-65] At early stage, the precursor is decomposed and then metal atoms are generated with time, leading to a continuous increase in the atomic concentration. After reaching a minimum supersaturation concentration, the atoms would self-nucleate into small nuclei until the atomic concentration drops below the minimum supersaturation concentration. At this time point, the newly generated atoms would continue the growth on the existing nuclei. Depending on the capping agents involved in the reaction solution to tailor the surface energies of different facets and thus their growth rates, nanocrystals would be transformed into different equilibrium shapes. As illustrated in Figure 1.9, it's important to control the selective growth on single crystalline seeds and etch away the multiply twinned particles with the addition of oxygen or chloride ions for producing a batch of uniform Ag nanocubes.[58, 66]

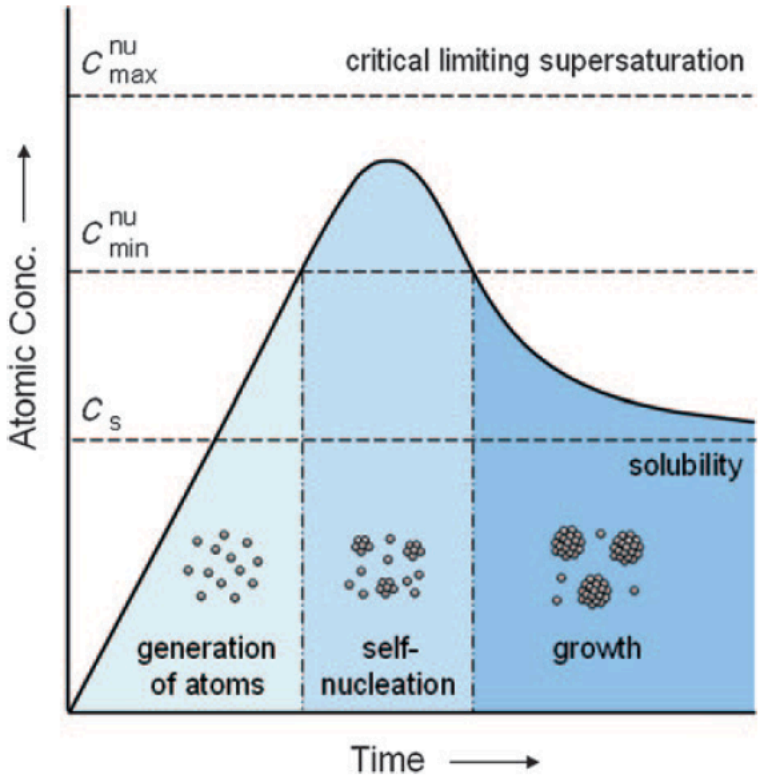

Figure 1.9. Schematic illustration of the atomic concentration in a function of time during homogeneous nucleation. Copyright 2009 WILEY-VCH Verlag GmbH & Co. KGaA, Weinheim.[6]

1.2.2 Synthesis of Silver-Based Bimetallic Nanocrystals

Noble-metal nanocrystals have found applications in areas ranging from catalysis to photonics, electronics, sensing, imaging, and biomedical research.[67-71] Bimetallic nanocrystals, in particular, have received ever growing interest in recent years because of their enhanced properties relative to their monometallic counterparts.[72-76] By controlling the ratio and spatial distributions of the elements, one can engineer and enrich the properties of bimetallic nanocrystals to greatly expand their scope of applications. There

are two major general strategies that have been documented for the syntheses of bimetallic nanocrystals.

Galvanic replacement reaction could serve as a facile approach to the fabrication of bimetallic or multi-metallic nanocrystals. It relies on the oxidation of one metal from the template for the reduction of the precursor of another metal to generate atoms followed by their deposition on the template.[77] The driving force for this reaction is based on the reduction potential differences of the two metals (Table 1.1).[78] For example, Schlücker and his coworker documented the synthesis of Au@Pt/Au core-shell nanoscale raspberries by depositing Ag on Au nanoparticles, followed by the galvanic replacement reaction between Ag and Pt/Au precursors.[79] Xia and co-workers reported that galvanic replacement reaction occurred between Ag and metal precursors to Pt/Pd for the generation of Pd-Ag or Pt-Ag nanocubes.[80] Because galvanic replacement often results in the loss of Ag content in the nanocrystals, and ultimately deteriorates in SERS activity of Ag nanocrystals,[80] one should fight against galvanic replacement reaction between the Ag seeds and the precursor of second metal, allowing the deposition of second metal onto Ag in the layer-by-layer manner for the generation of core-shell or core-frame nanostructures.

Seeded growth offers one of the most effective routes to the facile synthesis of bimetallic nanocrystals by using the preformed nanocrystals as "seeds" to direct and dictate the deposition of the second metal.[81-84] Specifically, when a precursor to the second metal is introduced into a mixture containing the seeds, reducing agent, capping agent, and colloidal stabilizer, it will be reduced to zero-valent atoms, which then heterogeneously nucleate and grow from the surface of the seeds to generate bimetallic nanocrystals. By carefully choosing a proper combination of seeds, metal precursor, and other experimental

Table 1.1. Reduction potentials of metals relative to the standard hydrogen electrode (SHE). Copyright 2016 American Chemical Society.[72]

Reduction Reaction	E_0 (V vs SHE)[a]
$Au^{3+} + 3e^- \rightarrow Au$	1.50
$Pt^{2+} + 2e^- \rightarrow Pt$	1.18
$Ir^{3+} + 3e^- \rightarrow Ir$	1.16
$Pd^{2+} + 2e^- \rightarrow Pd$	0.95
$Ag^{+} + e^- \rightarrow Ag$	0.80
$Rh^{3+} + 3e^- \rightarrow Rh$	0.76
$Ru^{3+} + 3e^- \rightarrow Ru$	0.45
$Cu^{2+} + 2e^- \rightarrow Cu$	0.34
$Ni^{2+} + 2e^- \rightarrow Ni$	-0.25
$Co^{2+} + 2e^- \rightarrow Co$	-0.28
$Fe^{2+} + 2e^- \rightarrow Fe$	-0.44

[a]Standard conditions: 25 °C and 1 atm. SHE: standard hydrogen electrode.

conditions, one can obtain bimetallic nanocrystals with well-defined compositions, sizes, shapes, and structures to meet the requests of different applications.[1, 6, 72, 85-86] In general, the second metal can be deposited on the seed conformally or in a site-selected fashion. When conformal deposition is involved, the seed is typically made of a plasmonic metal while the catalytic activity will be provided by the second metal. For site-selected deposition, however, one can even generate a dual catalyst of which the catalytic properties exhibited by both the seed and the second metal. For example, the similar lattices constant

of Ag and Au[87-89] would lead to conformal deposition of Au layer onto Ag seeds. In the case of Pt and Ag, anisotropic growth is in favor due to the lattice mismatch, leading to the growth of Ag nanowires on Pt seeds.[90]

1.2.3 Synthesis of Silver-Based Hybrid Nanocrystals

Hybrid nanoparticles are generally defined as the products constructed from more than one component phase.[91] Because these nanoparticles often integrate the multi-functionalities from the components, they have been extensively used in the applications including gene delivery,[92-93] sensing,[93] catalysis,[74] and SERS.[1, 94]

One of intriguing bimetallic systems is based upon Ag and Au. Silver nanocrystals embrace LSPR in the visible region for SERS,[58, 95] and they can also serve as a superb catalyst for oxidation reactions, including the epoxidation of ethylene by O_2.[96] On the other hand, Au is well known for its intrinsic inertness. However, it has been demonstrated that the catalytic activity of Au can be drastically enhanced by substantially downsizing the nanoparticles.[97-100] To this end, Haruta and co-workers discovered that the catalytic activity of TiO_2-supported Au nanoparticles toward CO oxidation increased significantly as their sizes were reduced down to 5 nm and below.[99] In principle, by simply coating the surface of Ag nanocrystals with discrete Au islands of less than 5 nm in size, one could design a useful bimetallic system with a unique integration of SERS and catalytic properties originating from the Ag and Au components, respectively.

Although it appears straightforward to prepare the aforementioned Ag-Au bimetallic system, the synthesis inherits a number of challenges. First of all, the galvanic replacement between Ag and $AuCl_4^-$ precludes the use of a protocol that involves the

reduction of $AuCl_4^-$ in the presence of Ag nanocrystals.[78] Even when the galvanic replacement is suppressed through the introduction of a strong reducing agent, the deposition of Au atoms tends to take a layer-by-layer rather than island growth mode.[101] It is possible to deposit pre-synthesized Au nanoparticles onto the surface of Ag nanocrystals through careful manipulation of surface charges, but it will be difficult to prevent the Au nanoparticles from touching and merging into larger structures. In addition, the tiny Au particles with an enormous surface-to-volume ratio have a strong tendency to coagulate during operation, ultimately losing their catalytic activity. One approach to improve the stability against coagulation is to encapsulate the Au nanoparticles with a thin, porous oxide layer, such as SiO_2, SnO_2, CeO_2, or TiO_2. To this end, it has been demonstrated that the oxide layer could serve as a physical barrier to isolate and confine the metal nanoparticles for a variety of systems.[102-107]

Silicon dioxide is one kind of silicone polymers derived from tetraethyl orthosilicate (TEOS). It is chemically inert especially in biological systems and it has high resistance to acid condition and heat. It is well known that different functional groups can be added to SiO_2 due to the presence of silanol groups on its surface. In fact, many groups have reported the capability to decorate SiO_2 shells on both metallic nanocrystals[108] and magnetic nanoparticles.[105, 109] It has been argued that such a thin layer of SiO_2 on the surfaces of nanoparticles would effectively avoid aggregation.

There are two general methods for the syntheses of silica-coated nanoparticles. The first method relies on the Stöber process that involves hydrolysis and polymerization of TEOS.[110] This approach has been implemented to coat a uniform and conformal layer of SiO_2 onto the surface of Ag, Au, and metal oxide nanoparticles.[106, 108, 111-112] Many groups

have demonstrated the use of this sol-gel process to coat SiO_2 on spherical nanoparticles[105, 109] and 1-D nanowires.[108, 112] Microemulsion synthesis represents another strategy that involves micelles or inverse micelles for the synthesis of the SiO_2 coating.[113-114]

1.3 Understanding Heterogeneous Nucleation of Second Metal on Noble Metal Nanocrystals

1.3.1 Homogenous and Heterogeneous Nucleation in the Nanocrystal Growth

In the synthesis of colloidal nanocrystals, nucleation stage is the most important stage that would determine the growth pattern and final structure of the products. The nucleation process could be categorized into homogeneous and heterogeneous nucleation. The two processes can be easily distinguished by the number of metallic species involved in the nucleation.[6, 65] In homogeneous nucleation, the seeds are generated *in situ* and the nucleation and growth are composed of the same chemical species. In heterogeneous nucleation, the preformed seeds will be added to a new system containing the precursors made of different species. The separation of nucleation and growth would result in an easy control of the size and morphology. In this case, the activation energy of heterogeneous nucleation is significantly lower than that of homogeneous nucleation,[115] which makes it possible for heterogeneous nucleation to occur at a relatively lower temperature or with a relatively mild reducing agent. Many bimetallic or hybrid nanocrystals can be fabricated *via* heterogeneous nucleation with precise control of size and morphology.[72, 74]

1.3.2 Current Methodologies for In Situ Monitoring Nanocrystal Growth

Although site-selective deposition has been successfully demonstrated for a set of bimetallic systems, including Pd-Rh, Pd-Pt, Ag-Au, and Ag-Pd (with the former being the seed and the latter the metal deposited),[1, 82, 116-120] it has been extremely challenging to resolve the second metal deposited on the surface of a nanocrystal, in particular, when the deposited amount is below one monolayer. Two different approaches are commonly used in the literature. The first is based upon elemental mapping using energy-dispersive X-ray spectroscopy (EDX) or electron energy loss spectroscopy (EELS) and the second involves selective etching of the original seed, followed by electron microscopy (EM) characterization of the remaining structure.[72, 78, 117, 119-122] Both EDX and EELS are well known for their superb spatial resolutions but it is nontrivial to obtain reliable data when the deposited metal is below one monolayer.[123] These techniques also require the use of advanced EM facilities and cannot be used to directly analyze a sample without drying and additional processing. The second approach, on the other hand, only works if the amount of the deposited metal is sufficient for the generation of a robust, free-standing hollow structure. During sample preparation, the adatoms can move around by diffusion, causing alternations to the original structure.

With the development of novel characterization tools, new technology has been developed for *in situ* characterization. Based on the traditional TEM, *in situ* liquid cell TEM has been developed for monitoring the nucleation during the growth process.[78, 123-124] By using the liquid cell, Ross *et al.* demonstrate the capability to watch the dynamic nucleation and growth of nanoscale Cu clusters during the process of electrodeposition.[124] Evans *et al.* implemented a continuous flow *in situ* liquid stage for aberration corrected STEM to monitor the growth of PbS nanoparticle over time.[125] X-ray scattering has also

been applied to nanoparticle structural characterization with atomic resolution and *in situ* monitoring capacity, under the original growth conditions.[126] Atomic diffraction, wide-angle X-ray scattering (WAXS) and small-angle X-ray scattering (SAXS) and other X-ray related tools have been used for various studies.[126-129] However, the *in situ* TEM and X-ray scattering often involves photochemical reactions between the beam source and the nanocrystals, leading to structural change or even sample damage.[126] It remains challenging to reveal the mechanistic details during the nucleation process and a new methodology is in need.

1.3.3 *In Situ SERS Monitoring of Heterogeneous Nucleation in the Nanocrystal Growth with a Molecular Probe*

We can address the challenge by taking a paradigm shift through the development of metal-sensitive SERS probes for better understanding the heterogeneous nucleation and early-stage deposition of metal atoms (M) on the edges of Ag nanocubes. Our central hypothesis is that the vibrational frequency of a metal-sensitive SERS probe can serve as a distinctive reporter for the metal being deposited on the surface of a Ag nanocrystal, with a detection limit well below one monolayer. More significantly, such an analysis can be conducted while the particles are still suspended in the original reaction solution for *in situ* characterization of the heterogeneous nucleation and early-stage deposition.

Focusing on a well-defined model system based upon Ag nanocubes with slight truncation at the corners and edges, according to the simulation results obtained using the discrete dipole approximation (DDA) method, intensified electric fields will be created on the edges of a Ag nanocube upon excitation of LSPR, generating hot spots for ultrasensitive

detection by SERS (see Figure 1.8B).[123] Remarkably, these hot spots coincide with the sites preferred for the heterogeneous nucleation and deposition of the second metal during seeded overgrowth because of their high surface free energies. As a result, it is feasible to elucidate the fundamental details by introducing a metal-sensitive SERS probe capable of differentiating the deposited M atoms from the original Ag atoms.

Conventionally, SERS probes are based on thiol molecules, with notable examples including 4-nitrothiophenol (4-NTP) and 1,4-benzenedithiol (1,4-BDT). The vibrational modes associated with their benzene rings are strong enough to allow for ultrasensitive detection of these molecules upon adsorption onto the surface of Ag or Au nanocrystals.[130-133] However, these vibrational modes exhibit essentially no dependence on the metal surface, making them invalid for the differentiation of different metals. In comparison, SERS probes based on isocyanide compounds (R–NC) can bind to metals differently, leading to the difference in the stretching frequency of the -NC bond (ν_{NC}) (Figure 1.10).[123] For example, σ donation from the anti-bonding σ* orbital of the -NC group to the *d*-band of the metal would strengthen the NC bond, resulting in a blue shift for ν_{NC}.[134] In contrast, π-back donation from the metal *d*-band to the π* anti-bonding orbital of the -NC group would weaken the -NC bond, leading to a red shift for ν_{NC}.[135] To this end, we argue that the isocyanide-based SERS probe could serve as a distinctive reporter for investigating the heterogeneous nucleation and early stage deposition of the transition metal such as Pt on the plasmonic Ag nanocrystals by monitoring the change to the frequency of ν_{NC} with *in situ* SERS. As the first proof-of-concept demonstration, we reported the use of 2,6-dimethylphenyl isocyanide (2,6-DMPI) as a SERS probe for watching the overgrowth of Pt on Ag nanocubes in the original growth solution.[123] By monitoring the stretching

frequencies and the peak intensities of ν_{NC} in real time, we demonstrated that *in situ* SERS had the sensitivity to detect as few as 27 Pt atoms being deposited onto each edge of a 39-nm Ag nanocube.[123] Despite the remarkable detection sensitivity, we only observed one peak for ν_{NC} when 2,6-DMPI bound to Pt atoms in the atop configuration, making it impossible to further characterize the atomic arrangement of Pt atoms during the heterogeneous nucleation and early-stage deposition events.

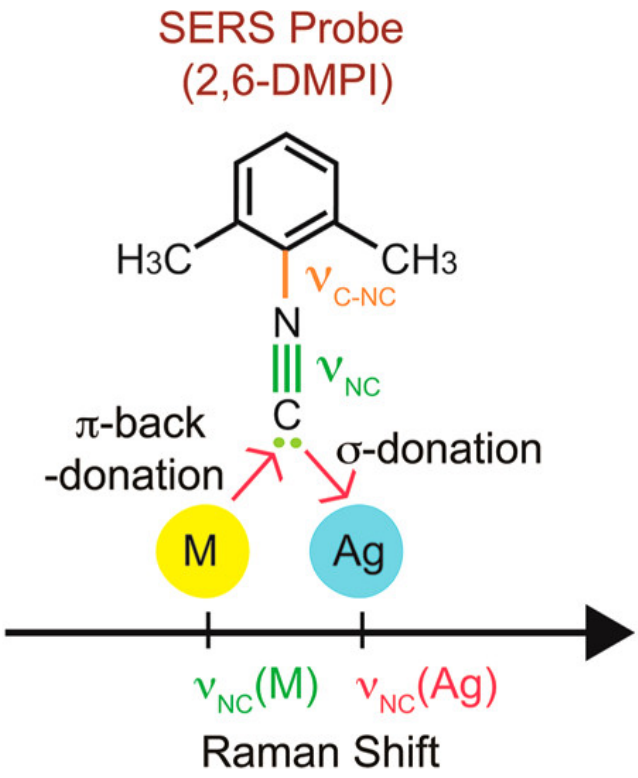

Figure 1.10. Schematic illustration showing the change of stretching frequency of –NC band when the –NC group binds to Ag and M atoms. Copyright 2017 American Chemical Society.[123]

1.4 In Situ SERS Monitoring of Catalytic Reactions on Plasmonically Active Metal Nanocrystals

Noble metal nanoparticles often exhibit high catalytic activities toward a wide range of reactions.[5, 13, 74-75, 105, 117-118, 136] Despite rapid development metallic nanoparticles for catalysis, the underlying reaction mechanism on the surface remains elusive. The reaction usually comes in a multi-phase system, making it more difficult to separate and detect reaction intermediates during the process. It is challenging to use the conventional techniques such as gas chromatography and nuclear magnetic resonance (NMR) spectroscopy, to monitor the catalytic reaction on the metallic nanoparticles in the real time.[137] SERS offers a powerful route to monitor the change of vibrational fingerprints of the molecules in proximity to the surface of plasmonically active nanocrystals such as Ag and Au, making it feasible to monitor the catalytic reactions in the real time.

1.4.1 Model Catalytic Reduction and Oxidation System

Based on the electrochemical model proposed by Haber,[138-139] Figure 1.11 shows two distinct routes for the hydrogenation of an aromatic nitro compound. In the direct route, the aromatic nitro compound is sequentially reduced to a nitroso compound, hydroxylamine, and finally an aniline derivative. Alternatively, in the indirect route, the nucleophilic hydroxylamine can react with the electrophilic nitroso to produce an azoxy compound, followed by consecutive steps for the formation of azo, hydrazo, and aniline compounds. In previous studies,[140-143] people have demonstrated the Pt-catalyzed reduction of a nitro compound to an aniline compound. However, it remains a grand challenge to tightly control the partial hydrogenation of an aromatic nitro compound to produce

thermodynamically unfavorable but industrially important compounds such as hydroxylamine and azo compounds with high selectivity.

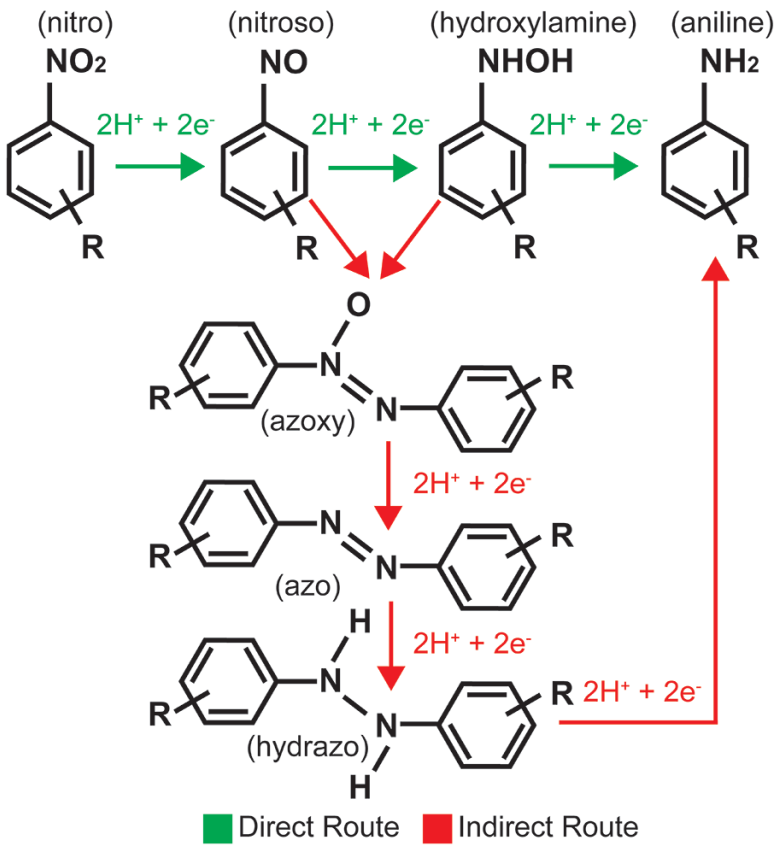

Figure 1.11. Two routes proposed to account for the hydrogenation of an aromatic nitro compound to the corresponding aniline.

1.4.2 In Situ SERS Monitoring of Reduction of 4-Nitrothiophenol and Oxidation of 4-Aminothiophenol

Thanks to the progress in controlling the synthesis of colloidal metal nanocrystals,

recent years has witnessed the successful development of bifunctional nanocrystals as a unique probe for investigating the mechanisms of catalytic reactions using surface-enhanced Raman scattering (SERS).[77, 85, 137] Although Au or Ag nanocrystals can serve as both catalytic and SERS substrates, one can greatly expand the range of catalytic reactions to be probed by depositing another metal such as Pt, Pd, Rh, and Ir on the surface of Au or Ag nanocrystals to generate bimetallic structures with dual functionality. To this end, many groups have made significant contributions to the fabrication and utilization of Au-M (M = Pt, Pd, and Ag) bimetallic nanocrystals, with Au in the core serving as a SERS substrate and Pd, Pt, or Ag in the shell (complete or incomplete) as a catalytic material.[140-141, 143] All these nanocrystals were further exploited for characterizing the reduction of 4-nitrothiophenol (4-NTP) to 4-aminothiophenol (4-ATP) by $NaBH_4$ *in situ* and in real time. On the other hand, our group has actively explored the fabrication and use of Ag@M (M=Pt, Pd, Au, and Rh) nanocubes with a core-frame, core-shell, or core-satellite structure for probing various catalytic reactions through SERS fingerprinting.[118, 142, 144-145] As a major advantage over the counterpart built upon a Au core, the system based on a Ag core offers a stronger plasmonic resonance and thus stronger SERS activity in the visible region because of the elimination of inter-band transition.[146]

It was established that the Au-catalyzed reduction of 4-NTP by $NaBH_4$ follows a condensation route, involving the formation of *trans*-4,4'-dimercaptoazobenzene (*trans*-DMAB) and 4-ATP as the intermediate and final product, respectively.[132, 144, 147-148] In comparison, Ag nanoparticles were found to have no catalytic activity for the reduction reaction under similar conditions.[118] As for Au-Pd or Au-Pt bimetallic nanoparticles, it was shown that the reduction occurred at much faster rates than the Au-based system, making

it challenging to capture the intermediate.[79, 141, 149] On the other hand, there are a number of reports on the formation of *trans*-DMAB from 4-ATP immobilized on the surface of Au or Ag nanoparticles through oxidation under ambient conditions.[150-151] In this case, it is well-known that primary aromatic amines can react with O_2 to form azobenzene derivatives.[152] Alternatively, it was proposed that the Au or Ag nanoparticles could interact with light through the excitation of localized surface plasmon resonance (LSPR) for the generation of hot electrons, which could then react with O_2 to generate reactive oxygen species in the presence of H_2O and thus enable the oxidation of 4-ATP to *trans*-DMAB.[133, 151-155] A systematic study of the reduction of an aromatic nitro compound by SERS not only allow for the elucidation of mechanisms by capturing the intermediates involved in the reactions but also offer insightful guidelines for the future design of more effective catalysts.

1.5 Scope of the Research

The aim of this work is to develop Ag nanocrystals and their derivatives with integrated plasmonic and catalytic properties for SERS applications. Despite the excellent LSPR and SERS properties of Ag nanocrystals, they are highly susceptible towards oxidative etching. One approach to provide a solution is to deposit a second metal on Ag nanocrystals to generate their derivatives for the potential applications in plasmonics and catalysis. This dissertation is organized into three parts: *i*) enriching silver nanocrystals with a second noble metal, *ii*) *in situ* SERS monitoring heterogeneous nucleation in nanocrystal growth with an isocyanide molecular probe, and *iii*) *in situ* SERS monitoring catalytic reactions on the surface of $Ag@SiO_2$/Au nanoparticles.

In Chapter 2, I describe two general methods for depositing a second metal on the surfaces of Ag nanocrystals without involving galvanic replacement and thus facile fabrication of bimetallic nanocrystals with a well-defined core-frame or core-shell structure. The success relies on the introduction of a parallel reduction reaction to compete with and thus suppress the galvanic replacement. In one approach, ascorbic acid is used at pH around 11.9 for generating ascorbate monoanion with a strong reduction power and thus defeating the galvanic replacement. Alternatively, the precursor is co-titrated with Ag^+ ions into a suspension of Ag nanocubes in the presence of ascorbic acid at a pH around 3.2. In this case, the presence of sufficient Ag^+ ions can push back the galvanic replacement, facilitating the deposition of an alloy onto the edges, corners, and part of the side faces of Ag nanocubes for the generation of core-frame nanocubes with increasingly thicker ridges. The plasmonic properties of the Ag nanocubes are essentially preserved while the second metal offers new capabilities. As a unique application, we demonstrate that the Ag@Pd-Ag core-frame nanocubes can serve as a dual catalyst for the Pd-catalyzed reduction of nitroaromatics to aromatic amines and then the Ag-catalyzed oxidation of amines to azo compounds while both reactions can be monitored and analyzed using SERS.

In Chapter 3, I report the synthesis of bifunctional $Ag@SiO_2$/Au nanoparticles with an "islands in the sea" configuration by titrating $HAuCl_4$ solution into an aqueous suspension of $Ag@SiO_2$ core-shell nanocubes in the presence of NaOH, ascorbic acid, and poly(vinylpyrrolidone) at pH=11.9. The NaOH plays an essential role in generating small pores in the SiO_2 shell *in situ*, followed by the epitaxial deposition of Au from the Ag surface through the pores, leading to the formation of Au islands (6–12 nm in size) immersed in a SiO_2 sea. By controlling the amount of $HAuCl_4$ titrated into the reaction

system, the Au islands can be made to pass through and protrude from the SiO_2 shell, embracing catalytic activity toward the reduction of 4-nitrophenol to 4-aminophenol by $NaBH_4$. While the Ag in the core provides a strong SERS activity, the SiO_2 sea helps maintain the Au component as compact, isolated, and stabilized islands. The $Ag@SiO_2/Au$ nanoparticles can serve as a bifunctional probe to monitor the stepwise Au-catalyzed reduction of 4-NTP to 4-ATP by $NaBH_4$ and Ag-catalyzed oxidation of 4-ATP to *trans*-DMAB by the O_2 from air in the same reaction system.

In Chapter 4, I demonstrate the use of 2,6-DMPI as a spectroscopic probe to study the heterogeneous nucleation and deposition of Pd on Ag nanocubes under different conditions by SERS. As a major advantage, the spectroscopic analysis can be performed *in situ* and in real time with the nanoparticles still suspended in the reaction solution. The success of this method relies on the distinctive stretching frequencies (ν_{NC}) of the isocyanide group in 2,6-DMPI when it binds to Ag and Pd atoms through σ donation and π-back donation, respectively. Significantly, we discover that ν_{NC} is sensitive to the arrangement of Pd adatoms on the Ag surface. For example, when the isocyanide group binds to one, two, and three Pd atoms, we would observe the atop, bridge, and hollow configurations, respectively, at different ν_{NC} frequencies. As such, the ν_{NC} band could serve as a characteristic reporter for the Pd adatoms being deposited onto different types of facets on Ag nanocubes with atomic-level sensitivity. Introducing 2,6-DMPI molecules into the reaction solution, we demonstrate *in situ* tracking of heterogeneous nucleation and early-stage deposition of Pd on Ag nanocubes by monitoring the evolution of ν_{NC} bands for both Ag and Pd surface atoms as a function of reaction time.

1.6 Notes to Chapter 1

Part of this chapter is adapted from the paper "Enriching Silver Nanocrystals with a Second Noble Metal" published in *Accounts of Chemical Research*, "Bifunctional Ag@SiO_2/Au Nanoparticles for Probing Sequential Catalytic Reactions by Surface-Enhanced Raman Spectroscopy" published in *ChemNanoMat*, "*In Situ* Atomic-Level Tracking of Heterogeneous Nucleation in Nanocrystal Growth with an Isocyanide Molecular Probe" in *Journal of the American Chemical Society*, and "Rational Design and Synthesis of Bifunctional Metal Nanocrystals for Probing Catalytic Reactions by Surface-Enhanced Raman Scattering" published in *Journal of Materials Chemistry C*.

1.7 References

[1] Rycenga, M.; Cobley, C. M.; Zeng, J.; Li, W.; Moran, C. H.; Zhang, Q.; Qin, D.; Xia, Y., Controlling the Synthesis and Assembly of Silver Nanostructures for Plasmonic Applications. *Chem. Rev.* **2011,** *111*, 3669-3712.

[2] Hamilton, J. F., The Silver Halide Photographic Process. *Adv. Phys.* **1988,** *37*, 359-441.

[3] William, K. C., Electrical Contact. U.S. Patent 2,241,262, May 6, 1941.

[4] Wang, L.; Sun, Y.; Wang, J.; Zhu, X.; Jia, F.; Cao, Y.; Wang, X.; Zhang, H.; Song, D., Sensitivity Enhancement of SPR Biosensor with Silver Mirror Reaction on the Ag/Au Film. *Talanta* **2009,** *78*, 265-269.

[5] Nagy, A.; Mestl, G., High Temperature Partial Oxidation Reactions over Silver Catalysts. *Appl. Catal., A* **1999,** *188*, 337-353.

[6] Xia, Y.; Xiong, Y.; Lim, B.; Skrabalak, S. E., Shape-Controlled Synthesis of Metal Nanocrystals: Simple Chemistry Meets Complex Physics? *Angew. Chem. Int. Ed.* **2009,** *48*, 60-103.

[7] Wiley, B.; Sun, Y.; Xia, Y., Synthesis of Silver Nanostructures with Controlled Shapes and Properties. *Acc. Chem. Res.* **2007,** *40*, 1067-1076.

[8] Xia, X.; Zeng, J.; McDearmon, B.; Zheng, Y.; Li, Q.; Xia, Y., Silver Nanocrystals with Concave Surfaces and Their Optical and Surface-Enhanced Raman Scattering Properties. *Angew. Chem. Int. Ed.* **2011,** *50*, 12542-12546.

[9] Cang, H.; Sun, T.; Li, Z.-Y.; Chen, J.; Wiley, B. J.; Xia, Y.; Li, X., Gold Nanocages as Contrast Agents for Spectroscopic Optical Coherence Tomography. *Opt. Lett.* **2005,** *30*, 3048-3050.

[10] Chen, J.; Saeki, F.; Wiley, B. J.; Cang, H.; Cobb, M. J.; Li, Z.-Y.; Au, L.; Zhang, H.; Kimmey, M. B.; Xia, Y., Gold Nanocages: Bioconjugation and Their Potential Use as Optical Imaging Contrast Agents. *Nano Lett.* **2005,** *5*, 473-477.

[11] Yang, X.; Skrabalak, S. E.; Li, Z.-Y.; Xia, Y.; Wang, L. V., Photoacoustic Tomography of a Rat Cerebral Cortex *in vivo* with Au Nanocages as an Optical Contrast Agent. *Nano Lett.* **2007,** *7*, 3798-3802.

[12] McLellan, J. M.; Siekkinen, A.; Chen, J.; Xia, Y., Comparison of the Surface-Enhanced Raman Scattering on Sharp and Truncated Silver Nanocubes. *Chem. Phys. Lett.* **2006,** *427*, 122-126.

[13] Christopher, P.; Xin, H.; Linic, S., Visible-Light-Enhanced Catalytic Oxidation Reactions on Plasmonic Silver Nanostructures. *Nat. Chem.* **2011,** *3*, 467-472.

[14] Mayer, K. M.; Hafner, J. H., Localized Surface Plasmon Resonance Sensors. *Chem. Rev.* **2011,** *111*, 3828-3857.

[15] Mie, G., Beiträge zur Optik trüber Medien, speziell kolloidaler Metallösungen. *Ann. Phys. (Berlin)* **1908,** *330*, 377-445.

[16] Gans, R., Über die Form ultramikroskopischer Goldteilchen. *Ann. Phys. (Berlin)* **1912,** *342*, 881-900.

[17] Bohren, C. F.; Huffman, D. R., *Absorption and Scattering of Light by Small Particles*. John Wiley & Sons: 1983; pp 82-129.

[18] Mulvaney, P., Surface Plasmon Spectroscopy of Nanosized Metal Particles. *Langmuir* **1996,** *12*, 788-800.

[19] Willets, K. A.; Van Duyne, R. P., Localized Surface Plasmon Resonance Spectroscopy and Sensing. *Annu. Rev. Phys. Chem.* **2007,** *58*, 267-297.

[20] Kelly, K. L.; Coronado, E.; Zhao, L. L.; Schatz, G. C., The Optical Properties of Metal Nanoparticles: The Influence of Size, Shape, and Dielectric Environment. *J. Phys. Chem. B* **2003**, *107*, 668-677.

[21] Wang, H.; Tam, F.; Grady, N. K.; Halas, N. J., Cu Nanoshells: Effects of Interband Transitions on the Nanoparticle Plasmon Resonance. *J. Phys. Chem. B* **2005,** *109*, 18218-18222.

[22] Link, S.; El-Sayed, M. A., Spectral Properties and Relaxation Dynamics of Surface Plasmon Electronic Oscillations in Gold and Silver Nanodots and Nanorods. *J. Phys. Chem. B* **1999,** *103*, 8410-8426.

[23] Hartland, G. V., Optical Studies of Dynamics in Noble Metal Nanostructures. *Chem. Rev.* **2011,** *111*, 3858-3887.

[24] Yee, K., Numerical Solution of Initial Boundary Value Problems Involving Maxwell's Equations in Isotropic Media. *IEEE Trans. Antennas Propag.* **1966,** *14*, 302-307.

[25] Yang, W. H.; Schatz, G. C.; Van Duyne, R. P., Discrete Dipole Approximation for Calculating Extinction and Raman Intensities for Small Particles with Arbitrary Shapes. *J. Chem. Phys.* **1995,** *103*, 869-875.

[26] Zhao, J.; Pinchuk, A. O.; McMahon, J. M.; Li, S.; Ausman, L. K.; Atkinson, A. L.; Schatz, G. C., Methods for Describing the Electromagnetic Properties of Silver and Gold Nanoparticles. *Acc. Chem. Res.* **2008,** *41*, 1710-1720.

[27] Le Ru, E.; Etchegoin, P., *Principles of Surface-Enhanced Raman Spectroscopy: and Related Plasmonic Effects*. Elsevier: 2008.

[28] Fleischmann, M.; Hendra, P. J.; McQuillan, A. J., Raman Spectra of Pyridine Adsorbed at a Silver Electrode. *Chem. Phys. Lett.* **1974,** *26*, 163-166.

[29] Jeanmaire, D. L.; Van Duyne, R. P., Surface Raman Spectroelectrochemistry: Part I. Heterocyclic, Aromatic, and Aliphatic Amines Adsorbed on the Anodized Silver Electrode. *J. Electroanal. Chem.* **1977,** *84*, 1-20.

[30] Van Duyne, R. P., *Chemical and Biochemical Applications of Lasers*. Academic: 1979, Vol. 4, p 101.

[31] McFarland, A. D.; Young, M. A.; Dieringer, J. A.; Van Duyne, R. P., Wavelength-Scanned Surface-Enhanced Raman Excitation Spectroscopy. *J. Phys. Chem. B* **2005,** *109*, 11279-11285.

[32] Campion, A.; Kambhampati, P., Surface-Enhanced Raman Scattering. *Chem. Soc. Rev.* **1998,** *27*, 241-250.

[33] Jensen, L.; Aikens, C. M.; Schatz, G. C., Electronic Structure Methods for Studying Surface-Enhanced Raman Scattering. *Chem. Soc. Rev.* **2008,** *37*, 1061-1073.

[34] Morton, S. M.; Jensen, L., Understanding the Molecule-Surface Chemical Coupling in SERS. *J. Am. Chem. Soc.* **2009,** *131*, 4090-4098.

[35] Zhao, L.; Jensen, L.; Schatz, G. C., Pyridine-Ag_{20} Cluster: A Model System for Studying Surface-Enhanced Raman Scattering. *J. Am. Chem. Soc.* **2006,** *128*, 2911-2919.

[36] Morton, S. M.; Silverstein, D. W.; Jensen, L., Theoretical Studies of Plasmonics Using Electronic Structure Methods. *Chem. Rev.* **2011,** *111*, 3962-3994.

[37] Jin, J., *The Finite Element Method in Electromagnetics*, John Willey & Sons: 2002.

[38] Tamaru, K., *In situ* Surface Dynamics in Heterogeneous Catalysis. *Appl. Catal., A* **1997,** *151*, 167-177.

[39] Lu, J.; Luo, M.; Lei, H.; Bao, X.; Li, C., Epoxidation of Propylene on NaCl-Modified $VCe_{1-x}Cu_x$ Oxide Catalysts with Direct Molecular Oxygen as the Oxidant. *J. Catal.* **2002,** *211*, 552-555.

[40] Allpress, J.; Sanders, J., The Structure and Orientation of Crystals in Deposits of Metals on Mica. *Surf. Sci.* **1967,** *7*, 1-25.

[41] Özbek, M. O.; Önal, I.; van Santen, R. A., Ethylene Epoxidation Catalyzed by Silver Oxide. *ChemCatChem* **2011,** *3*, 150-153.

[42] Van den Hoek, P.; Baerends, E. J.; van Santen, R. A., Ethylene Epoxidation on Silver(110): the Role of Subsurface Oxygen. *J. Phys. Chem.* **1989,** *93*, 6469-6475.

[43] Van Santen, R. A.; Kuipers, H., *Advances in Catalysis*, Elsevier: 1987; Vol. 35, pp 265-321.

[44] Shiraishi, Y.; Toshima, N., Colloidal Silver Catalysts for Oxidation of Ethylene. *J. Mol. Catal. A: Chem.* **1999,** *141*, 187-192.

[45] Lu, J.; Luo, M.; Lei, H.; Li, C., Epoxidation of Propylene on NaCl-Modified Silver Catalysts with Air as the Oxidant. *Appl. Catal., A* **2002,** *237*, 11-19.

[46] Zemichael, F. W.; Palermo, A.; Tikhov, M. S.; Lambert, R. M., Propene Epoxidation over K-Promoted Ag/$CaCO_3$ Catalysts: The Effect of Metal Particle Size. *Catal. Lett.* **2002,** *80*, 93-98.

[47] Chimentão, R. J.; Kirm, I.; Medina, F.; Rodríguez, X.; Cesteros, Y.; Salagre, P.; Sueiras, J. E., Different Morphologies of Silver Nanoparticles as Catalysts for the Selective Oxidation of Styrene in the Gas Phase. *Chemical Commun.* **2004,** *7*, 846-847.

[48] Xu, R.; Wang, D.; Zhang, J.; Li, Y., Shape-Dependent Catalytic Activity of Silver Nanoparticles for the Oxidation of Styrene. *Chem. Asian J.* **2006,** *1*, 888-893.

[49] Fuku, K.; Hayashi, R.; Takakura, S.; Kamegawa, T.; Mori, K.; Yamashita, H., The Synthesis of Size- and Color-Controlled Silver Nanoparticles by Using Microwave Heating and Their Enhanced Catalytic Activity by Localized Surface Plasmon Resonance. *Angew. Chem.* **2013,** *125*, 7594-7598.

[50] Li, J.; Wu, Y.; Sun, X.; Liu, J.; Winget, S. A.; Qin, D., A Dual Catalyst with SERS Activity for Probing Stepwise Reduction and Oxidation Reactions. *ChemNanoMat* **2016,** *2*, 786-790.

[51] Hsieh, Y.-C.; Senanayake, S. D.; Zhang, Y.; Xu, W.; Polyansky, D. E., Effect of Chloride Anions on the Synthesis and Enhanced Catalytic Activity of Silver Nanocoral Electrodes for CO_2 Electroreduction. *ACS Catal.* **2015,** *5*, 5349-5356.

[52] Koh, A. L.; Bao, K.; Khan, I.; Smith, W. E.; Kothleitner, G.; Nordlander, P.; Maier, S. A.; McComb, D. W., Electron Energy-Loss Spectroscopy (EELS) of Surface Plasmons in Single Silver Nanoparticles and Dimers: Influence of Beam Damage and Mapping of Dark Modes. *ACS nano* **2009,** *3*, 3015-3022.

[53] Sint, K.; Wang, B.; Král, P., Selective Ion Passage through Functionalized Graphene Nanopores. *J. Am. Chem. Soc.* **2009,** *130*, 16448-16449.

[54] Yin, Y.; Li, Z.-Y.; Zhong, Z.; Gates, B.; Xia, Y.; Venkateswaran, S., Synthesis and Characterization of Stable Aqueous Dispersions of Silver Nanoparticles through the Tollens Process. *J. Mater. Chem.* **2002,** *12*, 522-527.

[55] Shen, L.; Ji, J.; Shen, J., Silver Mirror Reaction as an Approach to Construct Superhydrophobic Surfaces with High Reflectivity. *Langmuir* **2008,** *24*, 9962-9965.

[56] Tao, A.; Sinsermsuksakul, P.; Yang, P., Polyhedral Silver Nanocrystals with Distinct Scattering Signatures. *Angew. Chem. Int. Ed.* **2006,** *45*, 4597-4601.

[57] Wiley, B. J.; Wang, Z.; Wei, J.; Yin, Y.; Cobden, D. H.; Xia, Y., Synthesis and Electrical Characterization of Silver Nanobeams. *Nano Lett.* **2006,** *6*, 2273-2278.

[58] Zhang, Q.; Li, W.; Moran, C.; Zeng, J.; Chen, J.; Wen, L.-P.; Xia, Y., Seed-Mediated Synthesis of Ag Nanocubes with Controllable Edge Lengths in the Range of 30-200 nm and Comparison of Their Optical Properties. *J. Am. Chem. Soc.* **2010,** *132*, 11372-11378.

[59] Jana, N. R.; Gearheart, L.; Murphy, C. J., Seed-Mediated Growth Approach for Shape-Controlled Synthesis of Spheroidal and Rod-Like Gold Nanoparticles Using a Surfactant Template. *Adv. Mater.* **2001,** *13*, 1389-1393.

[60] Pietrobon, B.; McEachran, M.; Kitaev, V., Synthesis of Size-Controlled Faceted Pentagonal Silver Nanorods with Tunable Plasmonic Properties and Self-Assembly of These Nanorods. *ACS nano* **2009,** *3*, 21-26.

[61] Jin, R.; Cao, Y. C.; Hao, E.; Métraux, G. S.; Schatz, G. C.; Mirkin, C. A., Controlling Anisotropic Nanoparticle Growth through Plasmon Excitation. *Nature* **2003,** *425*, 487-490.

[62] Zhang, J.; Li, S.; Wu, J.; Schatz, G. C.; Mirkin, C. A., Plasmon-Mediated Synthesis

of Silver Triangular Bipyramids. *Angew. Chem. Int. Ed*. **2009,** *48*, 7787-7791.

[63] Cobley, C. M.; Rycenga, M.; Zhou, F.; Li, Z.-Y.; Xia, Y., Controlled Etching as a Route to High Quality Silver Nanospheres for Optical Studies. *J. Phys. Chem. C* **2009,** *113*, 16975-16982.

[64] LaMer, V. K.; Dinegar, R. H., Theory, Production and Mechanism of Formation of Monodispersed Hydrosols. *J. Am. Chem. Soc.* **1950,** *72*, 4847-4854.

[65] Tao, A. R.; Habas, S.; Yang, P., Shape Control of Colloidal Metal Nanocrystals. *Small* **2008,** *4*, 310-325.

[66] Zhang, Q.; Li, W.; Wen, L. P.; Chen, J.; Xia, Y., Facile Synthesis of Ag Nanocubes of 30 to 70 nm in Edge Length with CF_3COOAg as a Precursor. *Chem. Eur. J.* **2010,** *16*, 10234-10239.

[67] El-Sayed, M. A., Some Interesting Properties of Metals Confined in Time and Nanometer Space of Different Shapes. *Acc. Chem. Res.* **2001,** *34*, 257-264.

[68] Jones, M. R.; Osberg, K. D.; Macfarlane, R. J.; Langille, M. R.; Mirkin, C. A., Templated Techniques for the Synthesis and Assembly of Plasmonic Nanostructures. *Chem. Rev.* **2011,** *111*, 3736-3827.

[69] Xia, Y.; Li, W.; Cobley, C. M.; Chen, J.; Xia, X.; Zhang, Q.; Yang, M.; Cho, E. C.; Brown, P. K., Gold Nanocages: From Synthesis to Theranostic Applications. *Acc. Chem. Res.* **2011,** *44*, 914-924.

[70] Lal, S.; Clare, S. E.; Halas, N. J., Nanoshell-Enabled Photothermal Cancer Therapy: Impending Clinical Impact. *Acc. Chem. Res.* **2008,** *41*, 1842-1851.

[71] Haes, A. J.; Haynes, C. L.; McFarland, A. D.; Schatz, G. C.; Van Duyne, R. P.; Zou, S., Plasmonic Materials for Surface-Enhanced Sensing and Spectroscopy. *MRS Bull.* **2005,** *30*, 368-375.

[72] Gilroy, K. D.; Ruditskiy, A.; Peng, H.-C.; Qin, D.; Xia, Y., Bimetallic Nanocrystals: Syntheses, Properties, and Applications. *Chem. Rev.* **2016,** *116*, 10414-10472.

[73] Zhang, H.; Jin, M.; Xia, Y., Enhancing the Catalytic and Electrocatalytic Properties

of Pt-Based Catalysts by Forming Bimetallic Nanocrystals with Pd. *Chem. Soc. Rev.* **2012,** *41*, 8035-8049.

[74] Wang, D.; Li, Y., Bimetallic Nanocrystals: Liquid-Phase Synthesis and Catalytic Applications. *Adv. Mater.* **2011,** *23*, 1044-1060.

[75] Peng, Z.; Yang, H., Designer Platinum Nanoparticles: Control of Shape, Composition in Alloy, Nanostructure and Electrocatalytic Property. *Nano Today* **2009,** *4*, 143-164.

[76] DeSantis, C. J.; Weiner, R. G.; Radmilovic, A.; Bower, M. M.; Skrabalak, S. E., Seeding Bimetallic Nanostructures as a New Class of Plasmonic Colloids. *J. Phys. Chem. Lett.* **2013,** *4*, 3072-3082.

[77] Zhang, Y.; Wu, Y.; Qin, D., Rational Design and Synthesis of Bifunctional Metal Nanocrystals for Probing Catalytic Reactions by Surface-Enhanced Raman Scattering. *J. Mater. Chem. C* **2018,** *6*, 5353-5362.

[78] Xia, X.; Wang, Y.; Ruditskiy, A.; Xia, Y., 25th Anniversary Article: Galvanic Replacement: A Simple and Versatile Route to Hollow Nanostructures with Tunable and Well-Controlled Properties. *Adv. Mater.* **2013,** *25*, 6313-6333.

[79] Xie, W.; Herrmann, C.; Kömpe, K.; Haase, M.; Schlücker, S., Synthesis of Bifunctional Au/Pt/Au Core/Shell Nanoraspberries for *in situ* SERS Monitoring of Platinum-Catalyzed Reactions. *J. Am. Chem. Soc.* **2011,** *133*, 19302-19305.

[80] Chen, J.; Wiley, B.; McLellan, J.; Xiong, Y.; Li, Z.-Y.; Xia, Y., Optical Properties of Pd-Ag and Pt-Ag Nanoboxes Synthesized via Galvanic Replacement Reactions. *Nano Lett.* **2005,** *5*, 2058-2062.

[81] Sanedrin, R. G.; Georganopoulou, D. G.; Park, S.; Mirkin, C. A., Seed-Mediated Growth of Bimetallic Prisms. *Adv. Mater.* **2005,** *17*, 1027-1031.

[82] Habas, S. E.; Lee, H.; Radmilovic, V.; Somorjai, G. A.; Yang, P., Shaping Binary Metal Nanocrystals through Epitaxial Seeded Growth. *Nat. Mater.* **2007,** *6*, 692-697.

[83] DeSantis, C. J.; Sue, A. C.; Bower, M. M.; Skrabalak, S. E., Seed-Mediated Co-Reduction: A Versatile Route to Architecturally Controlled Bimetallic Nanostructures. *ACS nano* **2012,** *6*, 2617-2628.

[84] Xia, Y.; Gilroy, K. D.; Peng, H. C.; Xia, X., Seed-Mediated Growth of Colloidal Metal Nanocrystals. *Angew. Chem. Int. Ed*. **2017,** *56*, 60-95.

[85] Wu, Y.; Sun, X.; Yang, Y.; Li, J.; Zhang, Y.; Qin, D., Enriching Silver Nanocrystals with a Second Noble Metal. *Acc. Chem. Res.* **2017,** *50*, 1774-1784.

[86] Liu, H.; Liu, T.; Zhang, L.; Han, L.; Gao, C.; Yin, Y., Etching-Free Epitaxial Growth of Gold on Silver Nanostructures for High Chemical Stability and Plasmonic Activity. *Adv. Funct. Mater.* **2015,** *25*, 5435-5443.

[87] Yoo, H.; Millstone, J. E.; Li, S.; Jang, J.-W.; Wei, W.; Wu, J.; Schatz, G. C.; Mirkin, C. A., Core-Shell Triangular Bifrustums. *Nano Lett.* **2009,** *9*, 3038-3041.

[88] Tsuji, M.; Miyamae, N.; Lim, S.; Kimura, K.; Zhang, X.; Hikino, S.; Nishio, M., Crystal Structures and Growth Mechanisms of Au@Ag Core-Shell Nanoparticles Prepared by the Microwave-Polyol Method. *Cryst. Growth Des.* **2006,** *6*, 1801-1807.

[89] Seo, D.; Yoo, C. I.; Jung, J.; Song, H., Ag-Au-Ag Heterometallic Nanorods Formed through Directed Anisotropic Growth. *J. Am. Chem. Soc.* **2008,** *130*, 2940-2941.

[90] Sun, Y.; Yin, Y.; Mayers, B. T.; Herricks, T.; Xia, Y., Uniform Silver Nanowires Synthesis by Reducing $AgNO_3$ with Ethylene Glycol in the Presence of Seeds and Poly(Vinyl Pyrrolidone). *Chem. Mater.* **2002,** *14*, 4736-4745.

[91] Cortie, M. B.; McDonagh, A. M., Synthesis and Optical Properties of Hybrid and Alloy Plasmonic Nanoparticles. *Chem. Rev.* **2011,** *111*, 3713-3735.

[92] Guo, S.; Wang, E., Functional Micro/Nanostructures: Simple Synthesis and Application in Sensors, Fuel Cells, and Gene Delivery. *Acc. Chem. Res.* **2011,** *44*, 491-500.

[93] Salem, A. K.; Searson, P. C.; Leong, K. W., Multifunctional Nanorods for Gene Delivery. *Nat. Mater.* **2003,** *2*, 668-671.

[94] Sivanesan, A.; Witkowska, E.; Adamkiewicz, W.; Dziewit, Ł.; Kamińska, A.; Waluk, J., Nanostructured Silver-Gold Bimetallic SERS Substrates for Selective Identification of Bacteria in Human Blood. *Analyst* **2014,** *139*, 1037-1043.

[95] Michaels, A. M.; Nirmal, M.; Brus, L. E., Surface Enhanced Raman Spectroscopy of Individual Rhodamine 6G Molecules on Large Ag Nanocrystals. *J. Am. Chem. Soc.* **1999,** *121*, 9932-9939.

[96] Christopher, P.; Linic, S., Engineering Selectivity in Heterogeneous Catalysis: Ag Nanowires as Selective Ethylene Epoxidation Catalysts. *J. Am. Chem. Soc.* **2008,** *130*, 11264-11265.

[97] Hammer, B.; Norskov, J. K., Why Gold is the Noblest of all the Metals. *Nature* **1995,** *376*, 238-240.

[98] Overbury, S. H.; Schwartz, V.; Mullins, D. R.; Yan, W.; Dai, S., Evaluation of the Au Size Effect: CO Oxidation Catalyzed by Au/TiO_2. *J. Catal.* **2006,** *241*, 56-65.

[99] Haruta, M., Size- and Support-Dependency in the Catalysis of Gold. *Catal. Today* **1997,** *36*, 153-166.

[100] Janssens, T. V.; Carlsson, A.; Puig-Molina, A.; Clausen, B. S., Relation between Nanoscale Au Particle Structure and Activity for CO Oxidation on Supported Gold Catalysts. *J. Catal.* **2006,** *240*, 108-113.

[101] Yang, Y.; Liu, J.; Fu, Z.-W.; Qin, D., Galvanic Replacement-Free Deposition of Au on Ag for Core-Shell Nanocubes with Enhanced Chemical Stability and SERS Activity. *J. Am. Chem. Soc.* **2014,** *136*, 8153-8156.

[102] Yu, K.; Wu, Z.; Zhao, Q.; Li, B.; Xie, Y., High-Temperature-Stable Au@SnO_2 Core/Shell Supported Catalyst for CO Oxidation. *J. Phys. Chem. C* **2008,** *112*, 2244-2247.

[103] Lee, J.; Park, J. C.; Song, H., A Nanoreactor Framework of a Au@SiO_2 Yolk/Shell Structure for Catalytic Reduction of *p*-Nitrophenol. *Adv. Mater.* **2008,** *20*, 1523-1528.

[104] Arnal, P. M.; Comotti, M.; Schüth, F., High-Temperature-Stable Catalysts by Hollow Sphere Encapsulation. *Angew. Chem. Int. Ed*. **2006,** *45*, 8224-8227.

[105] Ge, J.; Zhang, Q.; Zhang, T.; Yin, Y., Core-Satellite Nanocomposite Catalysts Protected by a Porous Silica Shell: Controllable Reactivity, High Stability, and Magnetic Recyclability. *Angew. Chem.* **2008,** *120*, 9056-9060.

[106] Dai, Y.; Lim, B.; Yang, Y.; Cobley, C. M.; Li, W.; Cho, E. C.; Grayson, B.; Fanson, P. T.; Campbell, C. T.; Sun, Y.; Xia, Y., A Sinter-Resistant Catalytic System Based on Platinum Nanoparticles Supported on TiO_2 Nanofibers and Covered by Porous Silica. *Angew. Chem. Int. Ed*. **2010,** *49*, 8165-8168.

[107] Lu, P.; Campbell, C. T.; Xia, Y., A Sinter-Resistant Catalytic System Fabricated by Maneuvering the Selectivity of SiO_2 Deposition onto the TiO_2 Surface versus the Pt Nanoparticle Surface. *Nano Lett.* **2013,** *13*, 4957-4962.

[108] Yin, Y.; Lu, Y.; Sun, Y.; Xia, Y., Silver Nanowires Can Be Directly Coated with Amorphous Silica to Generate Well-Controlled Coaxial Nanocables of Silver/Silica. *Nano Lett.* **2002,** *2*, 427-430.

[109] Deng, Y.-H.; Wang, C.-C.; Hu, J.-H.; Yang, W.-L.; Fu, S.-K., Investigation of Formation of Silica-Coated Magnetite Nanoparticles via Sol-Gel Approach. *Colloids Surf. A* **2005,** *262*, 87-93.

[110] Stöber, W.; Fink, A.; Bohn, E., Controlled Growth of Monodisperse Silica Spheres in the Micron Size Range. *J. Colloid Interface Sci.* **1968,** *26*, 62-69.

[111] Ocana, M.; Hsu, W. P.; Matijević, E., Preparation and Properties of Uniform-Coated Colloidal Particles. 6. Titania on Zinc Oxide. *Langmuir* **1991,** *7*, 2911-2916.

[112] Ohmori, M.; Matijević, E., Preparation and Properties of Uniform Coated Colloidal Particles. VII. Silica on Hematite. *J. Colloid Interface Sci.* **1992,** *150*, 594-598.

[113] Santra, S.; Tapec, R.; Theodoropoulou, N.; Dobson, J.; Hebard, A.; Tan, W., Synthesis and Characterization of Silica-Coated Iron Oxide Nanoparticles in Microemulsion: The Effect of Nonionic Surfactants. *Langmuir* **2001,** *17*, 2900-2906.

[114] Darbandi, M.; Thomann, R.; Nann, T., Single Quantum Dots in Silica Spheres by Microemulsion Synthesis. *Chem. Mater.* **2005,** *17*, 5720-5725.

[115] Vesselinov, M. I., *Crystal Growth for Beginners: Fundamentals of Nucleation, Crystal Growth and Epitaxy*. World Scientific: 2016.

[116] Tsao, Y.-C.; Rej, S.; Chiu, C.-Y.; Huang, M. H., Aqueous Phase Synthesis of Au-Ag Core–Shell Nanocrystals with Tunable Shapes and Their Optical and Catalytic Properties. *J. Am. Chem. Soc.* **2013,** *136*, 396-404.

[117] Park, J.; Zhang, L.; Choi, S.-I.; Roling, L. T.; Lu, N.; Herron, J. A.; Xie, S.; Wang, J.; Kim, M. J.; Mavrikakis, M.; Xia, Y., Atomic Layer-By-Layer Deposition of Platinum on Palladium Octahedra for Enhanced Catalysts toward the Oxygen Reduction Reaction. *ACS nano* **2015,** *9*, 2635-2647.

[118] Li, J.; Liu, J.; Yang, Y.; Qin, D., Bifunctional Ag@Pd-Ag Nanocubes for Highly Sensitive Monitoring of Catalytic Reactions by Surface-Enhanced Raman Spectroscopy. *J. Am. Chem. Soc.* **2015,** *137*, 7039-7042.

[119] Xie, S.; Lu, N.; Xie, Z.; Wang, J.; Kim, M. J.; Xia, Y., Synthesis of Pd-Rh Core-Frame Concave Nanocubes and Their Conversion to Rh Cubic Nanoframes by Selective Etching of the Pd Cores. *Angew. Chem. Int. Ed*. **2012,** *51*, 10266-10270.

[120] Fan, Z.; Zhang, H., Template Synthesis of Noble Metal Nanocrystals with Unusual Crystal Structures and Their Catalytic Applications. *Acc. Chem. Res.* **2016,** *49*, 2841-2850.

[121] Egerton, R. F., *Electron Energy-Loss Spectroscopy in the Electron Microscope*. Springer Science & Business Media: 2011.

[122] Zhao, M.; Wang, X.; Yang, X.; Gilroy, K. D.; Qin, D.; Xia, Y., Hollow Metal Nanocrystals with Ultrathin, Porous Walls and Well-Controlled Surface Structures. *Adv. Mater.* **2018**, 1801956.

[123] Zhang, Y.; Liu, J.; Ahn, J.; Xiao, T.-H.; Li, Z.-Y.; Qin, D., Observing the Overgrowth of a Second Metal on Silver Cubic Seeds in Solution by Surface-Enhanced Raman Scattering. *ACS nano* **2017,** *11*, 5080-5086.

[124] Williamson, M. J.; Tromp, R. M.; Vereecken, P. M.; Hull, R.; Ross, F. M., Dynamic Microscopy of Nanoscale Cluster Growth at the Solid-Liquid Interface. *Nat. Mater.* **2003,** *2*, 532-536.

[125] Evans, J. E.; Jungjohann, K. L.; Browning, N. D.; Arslan, I., Controlled Growth of Nanoparticles from Solution with *in situ* Liquid Transmission Electron Microscopy. *Nano Lett.* **2011,** *11*, 2809-2813.

[126] Li, T.; Senesi, A. J.; Lee, B., Small Angle X-Ray Scattering for Nanoparticle Research. *Chem. Rev.* **2016,** *116*, 11128-11180.

[127] Jin, R., Quantum Sized, Thiolate-Protected Gold Nanoclusters. *Nanoscale* **2010,** *2*, 343-362.

[128] Abécassis, B.; Testard, F.; Kong, Q.; Francois, B.; Spalla, O., Influence of Monomer Feeding on a Fast Gold Nanoparticles Synthesis: Time-Resolved XANES and SAXS Experiments. *Langmuir* **2010,** *26*, 13847-13854.

[129] Zheng, H.; Smith, R. K.; Jun, Y.-W.; Kisielowski, C.; Dahmen, U.; Alivisatos, A. P., Observation of Single Colloidal Platinum Nanocrystal Growth Trajectories. *Science* **2009,** *324*, 1309-1312.

[130] Suzuki, S.; Kaneko, S.; Fujii, S.; Marqués-González, S.; Nishino, T.; Kiguchi, M., Effect of the Molecule-Metal Interface on the Surface-Enhanced Raman Scattering of 1,4-Benzenedithiol. *J. Phys. Chem. C* **2016,** *120*, 1038-1042.

[131] Joo, S. W.; Han, S. W.; Kim, K., Adsorption of 1,4-Benzenedithiol on Gold and Silver Surfaces: Surface-Enhanced Raman Scattering Study. *J. Colloid Interface Sci.* **2001,** *240*, 391-399.

[132] Zhang, Q.; Blom, D. A.; Wang, H., Nanoporosity-Enhanced Catalysis on Subwavelength Au Nanoparticles: A Plasmon-Enhanced Spectroscopic Study. *Chem. Mater.* **2014,** *26*, 5131-5142.

[133] Zhao, L.-B.; Chen, J.-L.; Zhang, M.; Wu, D.-Y.; Tian, Z.-Q., Theoretical Study on Electroreduction of *p*-Nitrothiophenol on Silver and Gold Electrode Surfaces. *J. Phys. Chem. C* **2015,** *119*, 4949-4958.

[134] Hu, J.; Tanabe, M.; Sato, J.; Uosaki, K.; Ikeda, K., Effects of Atomic Geometry and Electronic Structure of Platinum Surfaces on Molecular Adsorbates Studied by Gap-Mode SERS. *J. Am. Chem. Soc.* **2014,** *136*, 10299-10307.

[135] Hu, J.; Hoshi, N.; Uosaki, K.; Ikeda, K., Vibrational Spectroscopic Observation of Atomic-Scale Local Surface Sites Using Site-Selective Signal Enhancement. *Nano Lett.* **2015,** *15*, 7982-7986.

[136] Li, P.; Ma, B.; Yang, L.; Liu, J., Hybrid Single Nanoreactor for *in situ* SERS Monitoring of Plasmon-Driven and Small Au Nanoparticles Catalyzed Reactions. *Chem. Commun.* **2015,** *51*, 11394-11397.

[137] Xie, W.; Schlücker, S., Surface-Enhanced Raman Spectroscopic Detection of Molecular Chemo- and Plasmo-Catalysis on Noble Metal Nanoparticles. *Chem. Commun.* **2018,** *54*, 2326-2336.

[138] Haber, F.; Schmidt, C., The Reduction Procedure with the Electrical Reduction of the Nitrobenzene. *Z. Phys. Chem* **1900,** *32*, 271-287.

[139] Haber, F., Gradual Electrolytic Reduction of Nitrobenzene with Limited Cathode Potential. *Elektrochem. Angew. Phys. Chem* **1898,** *22*, 506-514.

[140] Jing, H.; Zhang, Q.; Large, N.; Yu, C.; Blom, D. A.; Nordlander, P.; Wang, H., Tunable Plasmonic Nanoparticles with Catalytically Active High-Index Facets. *Nano Lett.* **2014,** *14*, 3674-3682.

[141] Huang, J.; Zhu, Y.; Lin, M.; Wang, Q.; Zhao, L.; Yang, Y.; Yao, K. X.; Han, Y., Site-Specific Growth of Au-Pd Alloy Horns on Au Nanorods: A Platform for Highly Sensitive Monitoring of Catalytic Reactions by Surface Enhancement Raman Spectroscopy. *J. Am. Chem. Soc.* **2013,** *135*, 8552-8561.

[142] Zhang, Z.; Ahn, J.; Kim, J.; Wu, Z.; Qin, D., Facet-Selective Deposition of Au and Pt on Ag Nanocubes for the Fabrication of Bifunctional Ag@Au-Pt Nanocubes and Trimetallic Nanoboxes. *Nanoscale* **2018,** *10*, 8642-8649.

[143] Jing, H.; Wang, H., Structural Evolution of Ag-Pd Bimetallic Nanoparticles through Controlled Galvanic Replacement: Effects of Mild Reducing Agents. *Chem. Mater.* **2015,** *27*, 2172-2180.

[144] Zhang, J.; Winget, S. A.; Wu, Y.; Su, D.; Sun, X.; Xie, Z.-X.; Qin, D., Ag@Au Concave Cuboctahedra: A Unique Probe for Monitoring Au-Catalyzed Reduction and Oxidation Reactions by Surface-Enhanced Raman Spectroscopy. *ACS nano* **2016,** *10*, 2607-2616.

[145] Zhang, Y.; Ahn, J.; Liu, J.; Qin, D., Syntheses, Plasmonic Properties, and Catalytic Applications of Ag-Rh Core-Frame Nanocubes and Rh Nanoboxes with Highly Porous Walls. *Chem. Mater.* **2018,** *30*, 2151-2159.

[146] Beversluis, M. R.; Bouhelier, A.; Novotny, L., Continuum Generation from Single Gold Nanostructures through Near-Field Mediated Intraband Transitions. *Phys. Rev. B* **2003,** *68*, 115433.

[147] Xie, W.; Walkenfort, B.; Schlücker, S., Label-Free SERS Monitoring of Chemical Reactions Catalyzed by Small Gold Nanoparticles Using 3D Plasmonic Superstructures. *J. Am. Chem. Soc.* **2012,** *135*, 1657-1660.

[148] van Schrojenstein Lantman, E. M.; Deckert-Gaudig, T.; Mank, A. J.; Deckert, V.; Weckhuysen, B. M., Catalytic Processes Monitored at the Nanoscale with Tip-Enhanced Raman Spectroscopy. *Nat. Nanotechnol.* **2012,** *7*, 583-586.

[149] Joseph, V.; Engelbrekt, C.; Zhang, J.; Gernert, U.; Ulstrup, J.; Kneipp, J., Characterizing the Kinetics of Nanoparticle-Catalyzed Reactions by Surface-Enhanced Raman Scattering. *Angew. Chem. Int. Ed.* **2012,** *51*, 7592-7596.

[150] Huang, Y.-F.; Wu, D.-Y.; Zhu, H.-P.; Zhao, L.-B.; Liu, G.-K.; Ren, B.; Tian, Z.-Q., Surface-Enhanced Raman Spectroscopic Study of *p*-Aminothiophenol. *Phys. Chem. Chem. Phys.* **2012,** *14*, 8485-8497.

[151] Sun, M.; Xu, H., A Novel Application of Plasmonics: Plasmon-Driven Surface-Catalyzed Reactions. *Small* **2012,** *8*, 2777-2786.

[152] Konaka, R.; Kuruma, K.; Terabe, S., Mechanisms of Oxidation of Aniline and Related Compounds in Basic Solution. *J. Am. Chem. Soc.* **1968,** *90*, 1801-1806.

[153] Linic, S.; Christopher, P.; Ingram, D. B., Plasmonic-Metal Nanostructures for Efficient Conversion of Solar to Chemical Energy. *Nat. Mater.* **2011,** *10*, 911-921.

[154] Huang, Y.-F.; Zhu, H.-P.; Liu, G.-K.; Wu, D.-Y.; Ren, B.; Tian, Z.-Q., When the Signal Is not from the Original Molecule to Be Detected: Chemical Transformation of *para*-Aminothiophenol on Ag during the SERS Measurement. *J. Am. Chem. Soc.* **2010,** *132*, 9244-9246.

[155] Xu, P.; Kang, L.; Mack, N. H.; Schanze, K. S.; Han, X.; Wang, H.-L., Mechanistic Understanding of Surface Plasmon Assisted Catalysis on a Single Particle: Cyclic Redox of 4-Aminothiophenol. *Sci. Rep.* **2013,** *3*, 2997.

CHAPTER 2. ENRICHING SILVER NANOCRYSTALS WITH A SECOND NOBLE METAL

2.1 Introduction

Silver is perhaps the best choice of material for plasmonics and related applications owing to its relatively low cost and favorable dielectric functions.[1] Over the past two decades, significant progress has been made in the synthesis of Ag nanocrystals with controlled shapes and sizes to tailor their properties and thus optimize their performance in a range of applications.[2,3] In particular, Ag nanocrystals have been prepared with sharp features on the surface to drastically augment their surface-enhanced Raman scattering (SERS) activity.[4] However, the sharp features tend to vanish due to the high susceptibility of Ag towards oxidative etching,[5] leading to the deterioration of SERS. As another pitfall, Ag is limited in terms of catalytic application as it only shows activity towards oxidation reactions such as epoxidation,[6] not reduction reactions.

One can address the aforementioned limitations of Ag nanocrystals by introducing a second noble metal (M) such as Au, Pd, or Pt to generate Ag-M bimetallic nanocrystals.[7] The inclusion of a second metal can enhance the properties, and ultimately greatly expand the application landscape by bringing in new capabilities. In principle, Ag-M bimetallic nanocrystals can take at least three different configurations, in the form of alloy, core-frame, and core-shell, respectively. An alloy is a solid solution, in which the Ag and M atoms are miscible to each other at the atomic scale. In the case of Ag and Au, alloy nanocrystals with tunable compositions can be obtained *via* a co-reduction route.[8] However, it is

challenging to control the shape taken by the alloy nanocrystals, primarily due to the lack of a capping agent that can selectively bind to the same facet of different metals. As for the Ag-M core-frame and core-shell nanocrystals, they can be readily prepared using seeded growth by simply depositing M atoms on the surface of preformed Ag nanocrystals. This approach immediately benefits from the large number of Ag nanocrystals that have been prepared with well-controlled shapes.[3] When the M atoms are conformally deposited on the entire surface, a Ag@M core-shell nanocrystal is created.[9] In this case, the M shell can greatly improve the chemical stability of the particle, in addition to the new catalytic properties associated with M. If the shell is kept below 1–2 nm thick, the excellent plasmonic and SERS properties of the Ag core can still be leveraged. Alternatively, when the M atoms are selectively deposited on the edges of a Ag nanocrystal, for example, a Ag@M core-frame nanocrystal is formed.[10] In this structure, the excellent plasmonic and SERS properties of the Ag core are still retained while the deposited M brings in new catalytic capabilities. Significantly, both SERS and catalytic properties can be integrated in the core-shell and core-frame nanocrystals to offer a unique probe for *in situ* detection and analysis of catalytic reactions by SERS.

Seeded growth offers a powerful route to the synthesis of bimetallic nanocrystals with a core-frame or core-shell structure.[2] This approach is built upon the concept that preformed nanocrystals with uniform, a well-controlled size, shape, and structure can serve as seeds to template and direct the deposition of metal atoms. Despite its remarkable versatility to deposit another metal on Pd or Pt seeds,[7] its capability is limited by the possible galvanic replacement between the precursor to M and Ag seeds.[11-15] When the seeds are destroyed to a large extent, they can no longer serve as physical templates to

control the growth pattern and thus obtain the desired products. Many groups had attempted to suppress the galvanic replacement between Ag nanocrystals with a salt precursor to the second metal,[16-21] but it remained a challenge to apply seeded growth to the fabrication of Ag@M nanocrystals until a few years ago when we successfully developed an effective strategy.[9-10]

Our strategy relies on the use of a parallel reaction to compete with and thus suppress the galvanic reaction. Specifically, when Ag nanocrystals are mixed with a salt precursor to the second metal in the presence of a reducing agent, the added precursor can be reduced by both the Ag seeds (*via* galvanic replacement at a rate of R_{gal}) and reducing agent (*via* chemical reduction at a rate of R_{red}). Under $R_{red} > R_{gal}$, the precursor will be primarily reduced by the reducing agent instead of participating in the galvanic replacement. If self-nucleation is eliminated by titrating the precursor in a dropwise fashion, the metal atoms derived from the chemical reduction can be directed to nucleate from the surface of the Ag seeds, generating bimetallic nanocrystals with a core-frame or core-shell structure.

Using Ag nanocubes as a model system, Figure 2.1 illustrates two approaches to the fabrication of core-frame and core-shell nanocrystals in an aqueous solution under ambient conditions. The first approach involves the titration of aqueous M^{n+} precursor into an aqueous mixture of Ag nanocubes, ascorbic acid (H_2Asc, a reducing agent), poly(vinylpyrrolidone) (PVP, a colloidal stabilizer), and NaOH in the pH range of 10.3−11.9. The presence of OH^- can affect the deposition of M atoms in a number of ways.[22] For example, the H_2Asc should be neutralized by OH^- to give ascorbate monoanion ($HAsc^-$) under alkaline condition, the actual reducing agent associated with H_2Asc, achieving the condition of $R_{red} > R_{gal}$ needed for suppressing the galvanic reaction. Because

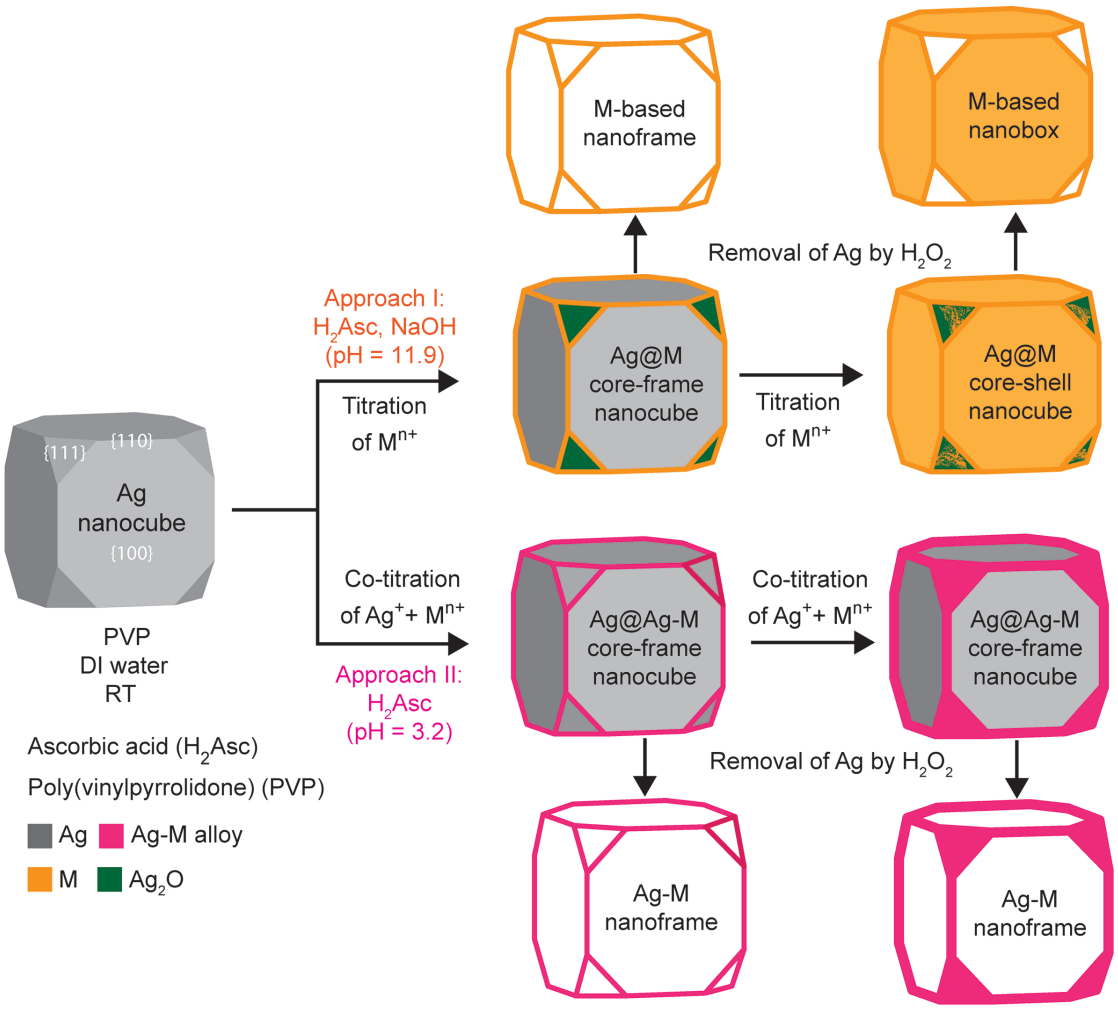

Figure 2.1. Schematic illustration of two proposed pathways for the deposition of a second metal M on a Ag nanocube seed for the generation of (top) a Ag@M core-frame and then core-shell nanocube and (bottom) a Ag@Ag-M core-frame nanocube, together with the resultant M-based nanoframe/nanobox and Ag-M nanoframes with ridges of different thicknesses after the removal of Ag core, respectively.

PVP binds more strongly to the {100} facets on Ag nanocubes, the specific surface free energies of the low-index facets on Ag nanocubes decrease in the order of $\gamma_{(110)} > \gamma_{(111)} > \gamma_{(100)}$.[2] As such, the M atoms derived from the reduction by $HAsc^-$ are sequentially deposited on the edges, corners, and side faces for the formation of Ag@M core-frame and

then core-shell nanocubes. It is worth mentioning that the site-selective deposition may also arise from a bipolar mechanism, in which reduction of M^{n+} and oxidation of $HAsc^-$ occur at different sites on the surface of a seed.[23]

In the case of Au deposition, with the involvement of OH^-, the titrated $AuCl_4^-$ precursor can undergo ligand exchange to generate $AuCl(OH)_3^-$ and $Au(OH)_4^-$ with lower reduction potentials and thus slower rates for both the reduction and galvanic reactions than the original precursor. In this case, galvanic replacement can still occur between the first few drops of $AuCl_4^-$ precursor and the Ag atoms situated at the corners. We argue that the released Ag^+ ions can react with OH^- instantaneously to generate Ag_2O patches at the corner sites, protecting the underlying Ag from further galvanic oxidation. After a few drops, the precursor is mostly reduced by $HAsc^-$ for the generation of Au atoms, followed by their deposition on the edges, side faces, and then corners for the generation of Ag@Au core-frame and then core-shell nanocubes. The core-frame nanocubes can be converted to Au-based nanoframes by directly etching away the Ag. For the core-shell nanocubes, they can be transformed into Au-based nanoboxes with well-defined openings at corners by dissolving the Ag_2O patches with a weak acid, followed by the removal of Ag.

The second approach involves the co-titration of aqueous Ag^+ and M^{n+} ions into an aqueous mixture of Ag nanocubes, H_2Asc, and PVP at a pH around 3.2.[10] When the added Ag^+ ions are able to push the galvanic replacement backward, R_{gal} can be reduced to attain $R_{red} > R_{gal}$ even at the slow reduction rate of H_2Asc rather than $HAsc^-$. Again, the Ag and M atoms derived from chemical co-reduction by H_2Asc are initially deposited on the edges, followed by sequential deposition on the corners and side faces, respectively. Upon the selective removal of Ag, Ag-M alloy nanoframes with different ridge thicknesses are

obtained.

In this chapter, we use Ag@Pd-Ag core-frame nanocubes as a case study to demonstrate the fabrication of Ag@M core-frame nanocubes with integrated SERS and catalytic properties. In a typical synthesis, we co-titrate $AgNO_3$ and Na_2PdCl_4 into an aqueous suspension containing Ag nanocubes, ascorbic acid (H_2Asc) and poly(vinylpyrrolidone) (PVP) in the ambient condition. We demonstrate that the galvanic replacement reaction between Ag nanocubes and $PdCl_4^{2-}$ would be effectively suppressed, when the molar ratio of $AgNO_3$ and Na_2PdCl_4 is at 0.5. As a result, Ag and Pd atoms derived from the co-reduction of $AgNO_3$ and Na_2PdCl_4 by H_2Asc would be deposited on the edges and corners for the generation of Ag@Pd-Ag core-frame nanocubes. By simply varying the co-titration volumes of each precursor, we would be able to tailor the elemental composition of the bimetallic nanocubes. We further demonstrate the utility of Ag@Pd-Ag core-frame nanocubes as a dual catalyst for probing the stepwise conversion of 4-nitrothiophenol (4-NTP) to *trans*-4,4'-dimercaptoazobenzene (*trans*-DMAB) under ambient conditions. The *in situ* SERS study reveals three sequential processes including (*i*) the Pd-catalyzed reduction of 4-NTP to 4-aminothiophenol (4-ATP) by hydrogen, (*ii*) a period during which the 4-ATP remain unchanged until all hydrogen has depleted, and (*iii*) the Ag-catalyzed oxidation of 4-ATP to *trans*-DMAB by the O_2 from air.

2.2 Experimental Section

Chemical and Materials. Poly(vinylpyrrolidone) with an average molecular weight of 29,000 (PVP-29K) or 55,000 (PVP-55K), silver nitrate ($AgNO_3$, ≥99.0%), silver trifluoroacetate (CF_3COOAg, ≥99.99% trace metal basis), sodium tetrachloropalladate (II),

(Na_2PdCl_4, 99.995%), sodium hydrosulfide hydrate ($NaHS{\cdot}xH_2O$), aqueous hydrochloric acid (HCl, 37%), L-ascorbic acid (H_2Asc, ≥98%), ethanol (CH_3CH_2OH, 200 proof), sodium borohydride ($NaBH_4$, 99.99%), and hydrogen peroxide (H_2O_2, 30 wt.% in H_2O) were all purchased from Sigma-Aldrich. Ethylene glycol ($HOCH_2CH_2OH$, EG) was obtained from J. T. Baker. Acetone (C_3H_6O, HPLC grade, 99.5+%) was obtained from Alfa Aesar. 4-Nitrothiophenol (4-NTP, $C_6H_5NO_2S$) was purchased from Oakwood Chemical. All chemicals were used as received. All aqueous solutions were prepared using deionized (DI) water with a resistivity of 18.2 MΩ·cm.

Synthesis of Ag Nanocubes. The Ag nanocubes were prepared using a published protocol[24] including the use of silver trifluoroacetate as a precursor and ethylene glycol (EG) as a reducing agent and solvent. Firstly, 5 mL of EG was added into a 100-mL round-bottom flask and heated to 150 °C in an oil bath under magnetic stirring. Next, 0.06 mL of 3 mM NaHS/EG solution was quickly injected. After 2 min, 0.5 mL of 3 mM HCl/EG was added, followed by 1.25 mL of 20 mg/mL PVP-55K/EG solution after another 2 min. After another 4 min, 0.4 mL of 282 mM CF_3COOAg/EG solution was injected. During the entire procedure, the flask was capped with a glass stopper, except for the introduction of reagents. After the major LSPR peak of the Ag nanocubes had shifted to 436 nm, the flask was immersed in an ice-water bath to terminate the reaction. The nanocubes were washed with acetone and deionized (DI) water three times through centrifugation and re-dispersion, followed by the dispersion in DI water for further use.

Synthesis of Ag@Pd-Ag Core-Frame Nanocubes. In a standard synthesis, we introduced 2 mL of 1 mM PVP-29K aqueous solution into a 23-mL glass vial, followed by

the addition of 0.5 mL of 100 mM aqueous ascorbic acid solution and 8 μL of the aqueous suspension of Ag nanocubes (1.01×10^{11} particles) under magnetic stirring. Next, we co-titrated different volumes of Na_2PdCl_4 (0.2 mM) and $AgNO_3$ (0.1 mM) aqueous solutions into the vial using a syringe pump at a rate of 0.02 mL/min. After 1 h, we collected the products by centrifugation at 7000 rpm for 15 min, washed with DI water three times, and then dispersed them in DI water for further use. The etching of Ag content was carried out by mixing the as-obtained sample (3.7×10^{10} particles in total) with 1 mL of 2.3% aqueous H_2O_2 at room temperature for 1 h. The resultant nanostructures were centrifuged and washed twice with DI water and dispersed in DI water for TEM characterization.

SERS Monitoring of Stepwise Reaction of 4-Nitrothiophenol. The Ag@Pd-Ag nanocubes were incubated in 2.5 mL of ethanol containing 4-nitrothiophenol (4-NTP, 10^{-6} M) for 1 h under ambient condition. The 4-NTP-functionalized nanocubes were washed with DI water twice and re-suspended in DI water to attain a concentration of approximately 8.7×10^{10} particles/mL. Then 200 μL of the nanocube suspension was mixed with 200 μL of 0.1 mg/mL aqueous $NaBH_4$ solution in a 1.5-mL centrifuge tube. An aliquot of 20 μL of the reaction solution was withdrawn at different time intervals and placed in a PDMS sample cell. The SERS spectra were recorded from the solution phase with laser excitation at 532 nm, together with a 5x objective lens, laser power of 50 mW and a collection time of 7 s for all samples.

Instrumentation and Characterization. Transmission electron microscopy (TEM) images were captured using a Hitachi HT7700 microscope (Hitachi, Japan) operated at 120 kV. The UV-vis spectra were collected using a Cary 50 spectrometer (Agilent Technologies, Santa Clara, CA). The Pd and Ag contents in each sample were analyzed

using an inductively coupled plasma mass spectrometer (ICP-MS, NexION 300Q, PerkinElmer, Waltham, MA). A conventional centrifuge (Eppendorf 5430) was used for the collection and washing of the as-prepared samples. High-angle annular dark field scanning TEM (HAADF-STEM) and energy dispersive spectroscopy (EDS) mapping were performed with a JEOL 2200FS STEM/TEM microscope equipped with a CEOS GmbH probe corrector operated at 200 kV. The SERS spectra were recorded using a Renishaw inVia Raman spectrometer (Wotton-under-Edge, UK) coupled with a Leica microscope (Wetzlar, Germany). The excitation wavelength was 532 nm and the scattered light was dispersed using a holographic notch filter with a grating of 2400 lines/mm.

2.3 Results and Discussion

2.3.1 Ag@Pd-Ag Core-Frame Nanocubes and Derivatives

As illustrated by the approach II in Figure 2.1, we can obtain Ag@Pd-Ag core-frame nanocubes by co-titrating aqueous $AgNO_3$ and Na_2PdCl_4 into an aqueous mixture containing Ag nanocubes, H_2Asc, and PVP at pH = 3.2.[10,25,26] Because the reduction potential of $PdCl_4^{2-}$ is lower than that of $AuCl_4^-$ and the Pd(II) precursor is added as a salt rather than an acid, the lower limit of molar ratio between $AgNO_3$ and Na_2PdCl_4 can be reduced to 0.5.[10] By varying the titration volume for each precursor, we could vary the elemental composition of the resultant structures. Figure 2.2 shows the TEM image of Ag nanocubes with an edge length of 39.2±1.6 nm. Figure 2.3, A–C, shows TEM images of the Ag@Pd-Ag core-frame nanocubes when the titration volume of each precursor was 0.1 mL, 0.2 mL and 0.3 mL, respectively. We noticed that no pits were observed in the resultant structures, indicating the successful suppression of galvanic replacement reaction.

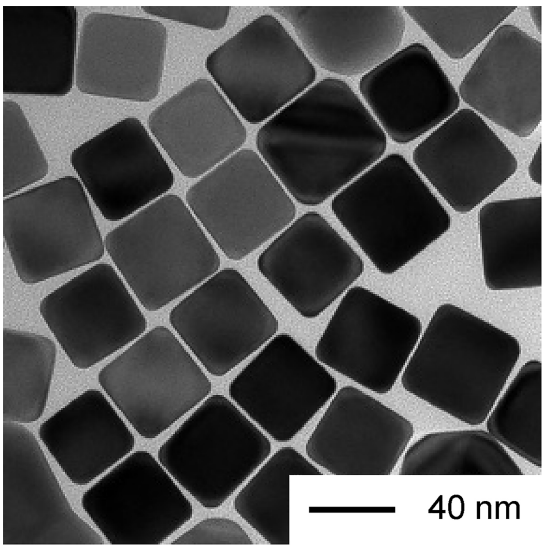

Figure 2.2. TEM images of the Ag nanocubes with an edge length of 39.2±1.6 nm.

The edges and corners of the nanocubes were even sharpened, suggesting the selective deposition sites of newly generated Pd and Ag atoms. At titration volume of 0.3 mL, we noticed the edge length of the nanocubes was increased from 39.2±1.6 nm (Figure 2.2) to 41.5±1.4 nm (Figure 2.3C). To confirm the deposition sites of Pd and Ag, we further etched the products with 2.3% H_2O_2 to remove the Ag content while Pd would remain intact. Figure 2.3, D–F, shows the corresponding Ag-Pd nanostructures after the removal of Ag cores. At the titration volume of 0.1 mL for each precursor, we obtained nanoframes with thin ridges and little coverage of corners (Figure 2.3D). When the titration volume was increased to 0.2 mL and 0.3 mL, we obtained nanoframes with thick ridges (Figure 2.3E) and nanocages (Figure 2.3F), respectively, consistent with our proposed mechanism in Figure 2.1. We also used inductively coupled plasma mass spectroscopy (ICP-MS) to determine Ag and Pd content in the product. At titration volume of 0.1 mL, 0.2 mL and

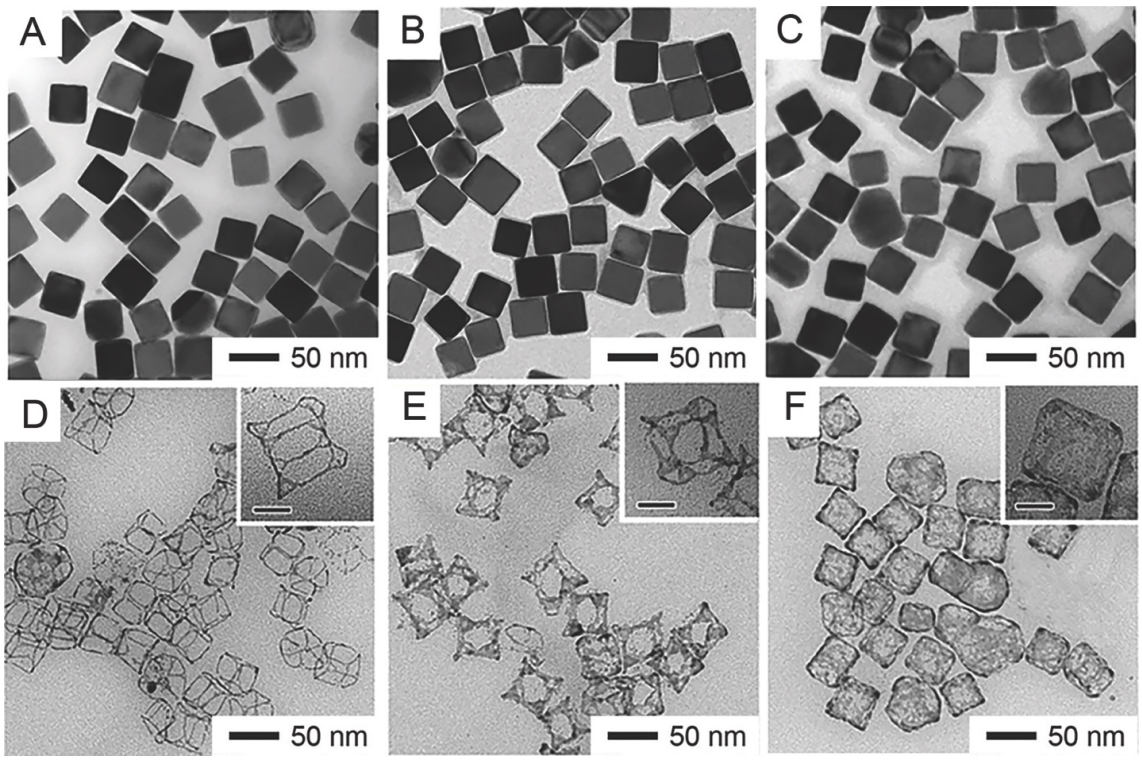

Figure 2.3. (A–C) TEM images of Ag@Pd-Ag nanocubes prepared by co-titrating aqueous Na_2PdCl_4 (0.2 mM) and $AgNO_3$ (0.1 mM), at 0.1, 0.2, and 0.3 mL for each precursor, respectively, into an aqueous suspension of Ag nanocubes in the presence of H_2Asc and PVP. (D–F) TEM images of the resultant structures after etching of samples shown in (A–C) with 3% H_2O_2. The scale bars in the insets are 20 nm.

0.3 mL, the Pd content was 2.2±0.2 wt.%, 3.6±0.3 wt.% to 4.6±0.3 wt.%, respectively.[10] To further confirm the deposition site of Pd on the Ag nanocubes, we used aberration-corrected high-angle annular dark-field scanning transmission electron microscopy (HAADF-STEM) to analyze the Ag@Pd-Ag nanocubes. Figure 2.4, A and B, shows the STEM images of the sample obtained at a co-titration volume of 0.2 mL for each precursor. Figure 2.4, C and D, shows energy dispersive X-ray spectroscopy (EDS) of the sample. The EDS mapping shows the elemental composition of Ag (blue) and Pd (red), suggesting

that most of the Pd atoms were preferentially located at the edge and corner sites of the nanocube for the generation of a core-frame structure.

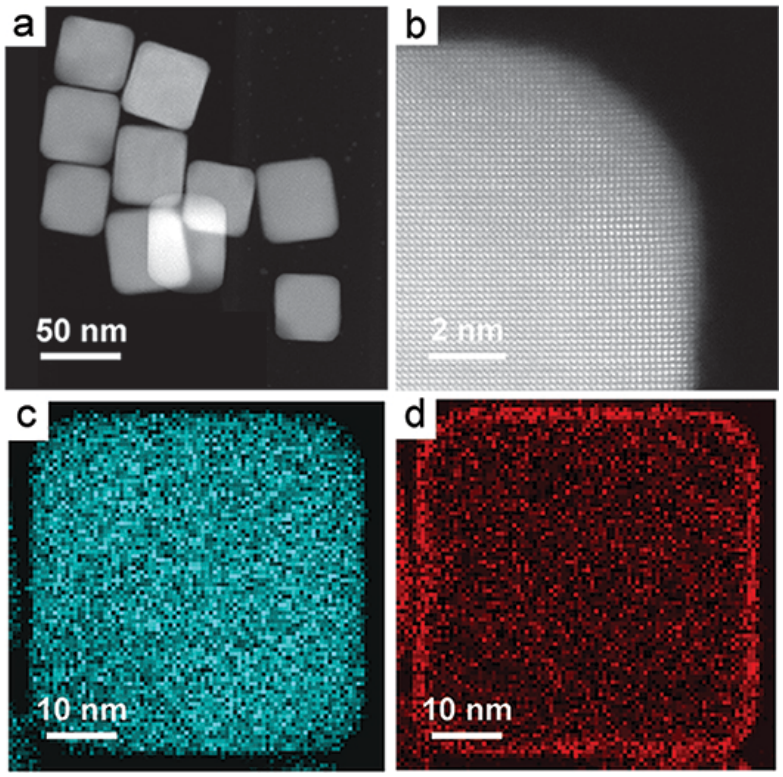

Figure 2.4. (A) HAADF-STEM image of a typical sample prepared with a titration volume of 0.2 mL for Na_2PdCl_4 and $AgNO_3$. (B) High-resolution HAADF-STEM image taken from one of the corners of an individual nanocube. (C, D) EDS mapping of a Ag@Pd-Ag nanocube (blue: Ag; red: Pd).

2.3.2 Ag@Pd-Ag Nanocubes for In Situ SERS Monitoring Chemical Reactions by SERS

Although many groups have demonstrated the use of bimetallic nanocrystals as a SERS probe for monitoring the catalytic reduction of 4-nitrothiophenol (4-NTP) by $NaBH_4$

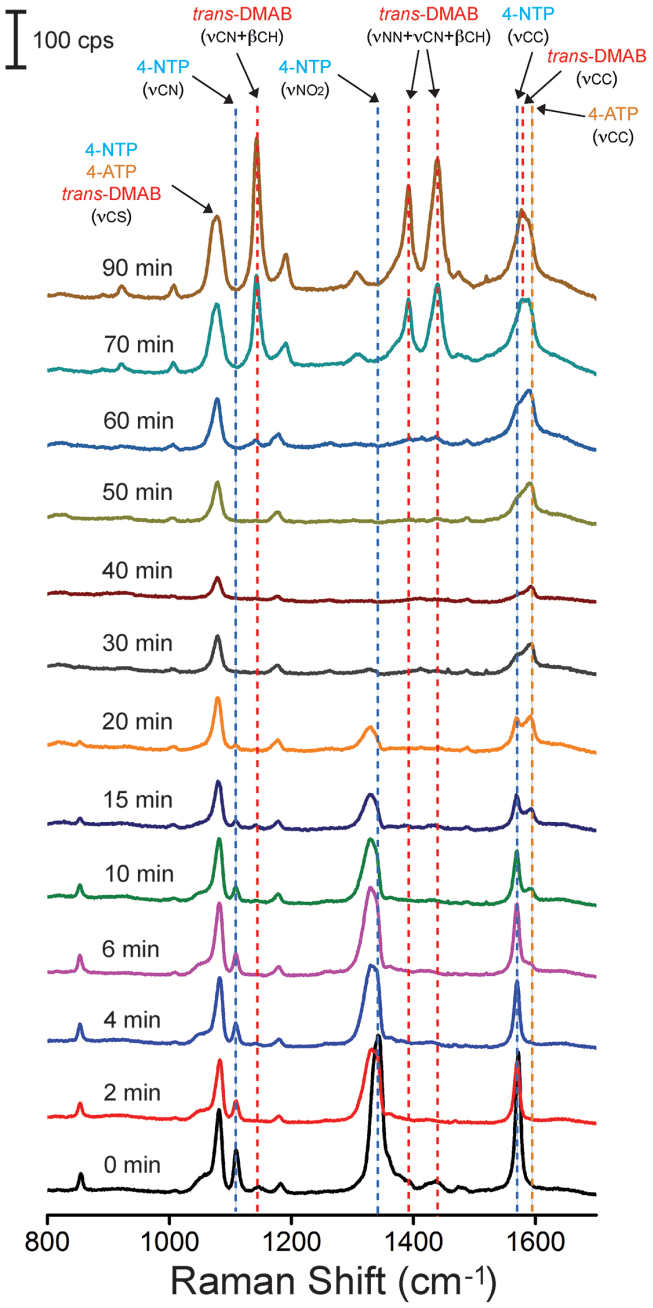

Figure 2.5. Time-dependent SERS spectra for monitoring the reduction of 4-NTP by $NaBH_4$ on Ag@Pd-Ag nanocubes with 2.2 wt.% Pd using laser excitation wavelength at 532 nm. The catalyst was prepared with the co-titration of 0.1 mL of Na_2PdCl_4 and $AgNO_3$ solution.

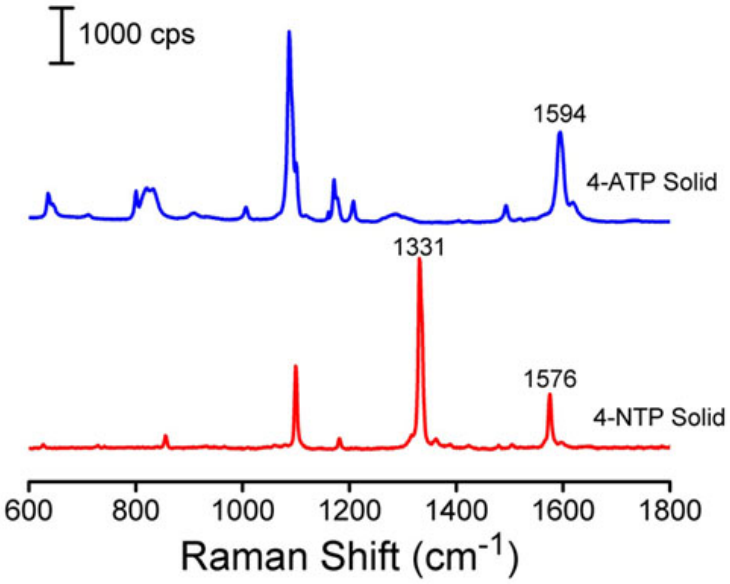

Figure 2.6. The ordinary Raman spectra of 4-NTP and 4-ATP.

to produce 4-aminothiophenol (4-ATP),[27] we are among the first to report the use of Ag@Pd-Ag core-shell nanocubes as a dual catalytic system capable of probing the Pd-catalyzed reduction of 4-NTP to 4-ATP and the subsequent Ag-catalyzed oxidation of 4-ATP to *trans*-DMAB by the O_2 from air.[28] Figure 2.5 shows the time-resolved SERS spectra collected from the 4-NTP absorbed on the Ag@Pd-Ag core-frame nanocubes containing 2.2 wt.% of Pd. Figure 2.6 provides an ordinary Raman spectrum of 4-NTP and 4-ATP with their peak assignments shown in Table 2.1.[29, 30] At t = 0 min, we observed three characteristic bands of 4-NTP at 1108 cm^{-1} (ν_{CN}), 1336 cm^{-1} (ν_{NO2}), and 1572 cm^{-1} (ν_{CC}). Upon the introduction of $NaBH_4$, the ν_{NO2} band was slightly shifted from 1336 to 1330 cm^{-1} at t = 2 min, while other bands remained essentially the same. At t = 6 min, a shoulder peak appeared at 1595 cm^{-1}, which can be assigned to the ν_{CC} of 4-ATP. As the

Table 2.1. The SERS and ordinary Raman shifts of 4-NTP and 4-ATP and their assignments.

	SERS (cm^{-1})	Ordinary Raman (cm^{-1})	Assignment[a]
4-NTP	854	854	C-H wagging
4-NTP	1080	1100	C-S stretching
4-NTP	1108	1098	O-N-O stretching
4-NTP	1336	1331	O-N-O stretching
4-NTP	1572	1576	phenyl-ring mode
4-ATP	1078	1080	C-S stretching
4-ATP	1173	1170	C-H in plane bending
4-ATP		1494	C-N stretching
4-ATP	1591	1594	phenyl-ring mode

[a]Ref. 29, 30.

reaction further progressed to 20 min, the ν_{CC} band of 4-ATP increased in intensity while both ν_{NO2} and ν_{CN} bands decreased in intensity. At t = 30 min, both the ν_{CN} and ν_{NO2} bands of 4-NTP could be no longer resolved. By 40 min, all the three bands of 4-NTP disappeared and the remaining peaks can be assigned to the ν_{CS}, β_{CH}, and ν_{CC} of 4-ATP, respectively, indicating the complete conversion from 4-NTP to 4-ATP. In the next 20 min, the three peaks of 4-ATP remained the same in peak position while their intensities were increased. At t = 70 min, we observed three new peaks at 1142 cm^{-1}, 1388 cm^{-1}, and 1429 cm^{-1}, which can be assigned to the $\beta_{CH}+\nu_{CN}$, $\nu_{NN}+\nu_{CN}$, and $\nu_{NN}+\beta_{CH}$ of *trans*-DMAB, respectively.[31]

These bands remained unaltered up to 90 min, except for slight increase in intensity.

When Ag-Pd nanocubes with 4.6 wt.% Pd was used as a dual catalyst, Figure 2.7 shows the time-resolved SERS spectra. At t = 0 min, we observed a 20% decrease in intensity for the 4-NTP peak at 1572 cm^{-1} (ν_{CC}). It is anticipated that the deposition of more Pd atoms on each Ag nanocube could deteriorate the SERS activity of Ag.[33] The drop in peak intensity might also indicate a weaker binding of 4-NTP molecules to the Pd surface. At t = 2 min, we observed four bands that can be assigned to 4-NTP and 4-ATP. As the reaction progressed to 4 min, we only observed the bands of 4-ATP, indicating the complete reduction of 4-NTP to 4-ATP at this time point. Taken together, we believe that the reduction of 4-NTP by $NaBH_4$ can be accelerated by increasing the proportion of Pd atoms on the surface of a catalytic particle. From 4 to 20 min, the spectrum remained essentially unaltered, echoing the "stable" period shown in Figure 2.5. At t = 30 min, three bands characteristic of *trans*-DMAB appeared. Again, 4-ATP was oxidized within a 10-min window (t = 20-30 min), similar to the case with a lower Pd content. At t = 60 min, the ν_{CS} band remained essentially the same but the intensities of other *trans*-DMAB bands increased, indicating the possible formation of hot spots due to particle aggregation. These data suggest that the oxidation of 4-ATP by the O_2 from air proceeded at comparable rate for both catalysts, with no correlation with the Pd content. We believe it is Ag that is responsible for the activation of O_2 dissolved in the reaction solution for the oxidation of 4-ATP to *trans*-DMAB.

Based on the SERS data, Figure 2.8 proposes a plausible mechanism. In the first step, the 4-NTP molecules adsorb on the Ag surface through the Ag–S linkage. Because

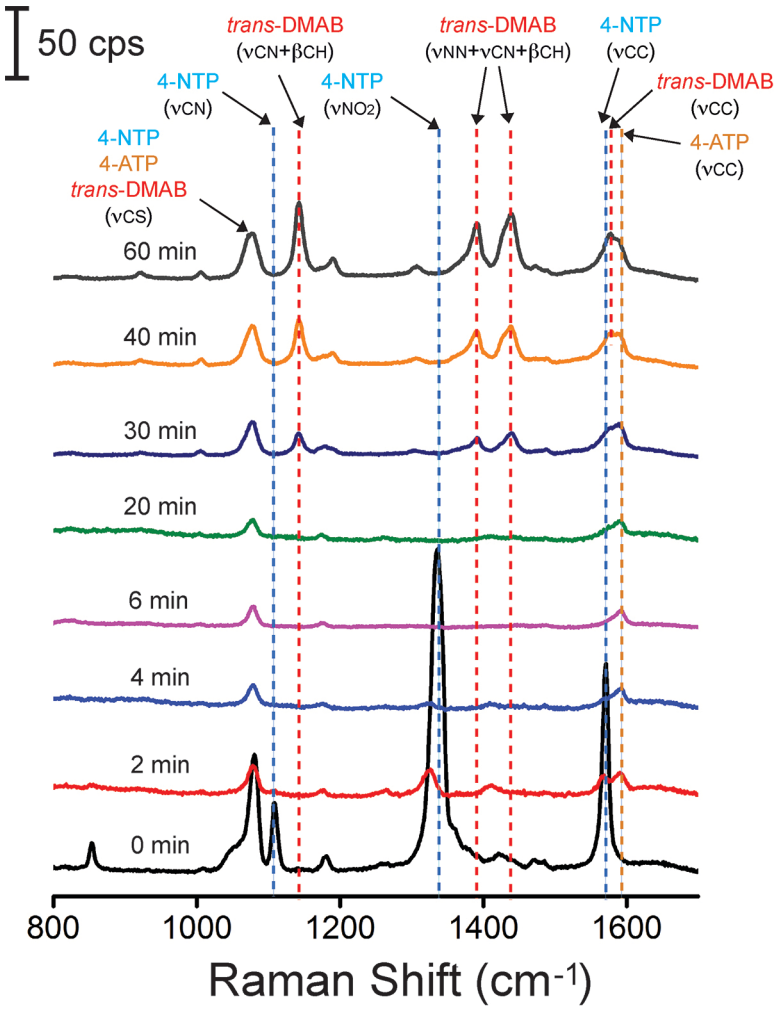

Figure 2.7. The SERS spectra were recorded before and after the introduction of $NaBH_4$ solution into an aqueous suspension of 4-NTP-functionalized Ag@Pd-Ag nanocubes at the excitation wavelength at 532 nm. The catalyst was prepared with the co-titration of 0.3 mL of Na_2PdCl_4 and $AgNO_3$ solution with 4.6 wt.% Pd.

of the formation of *trans*-DMAB rather than *cis*-DMAB, we assume that molecules are orientated with a configuration parallel to the surface. When $NaBH_4$ is introduced to an aqueous solution under ambient conditions, it will decompose to produce H_2, followed by

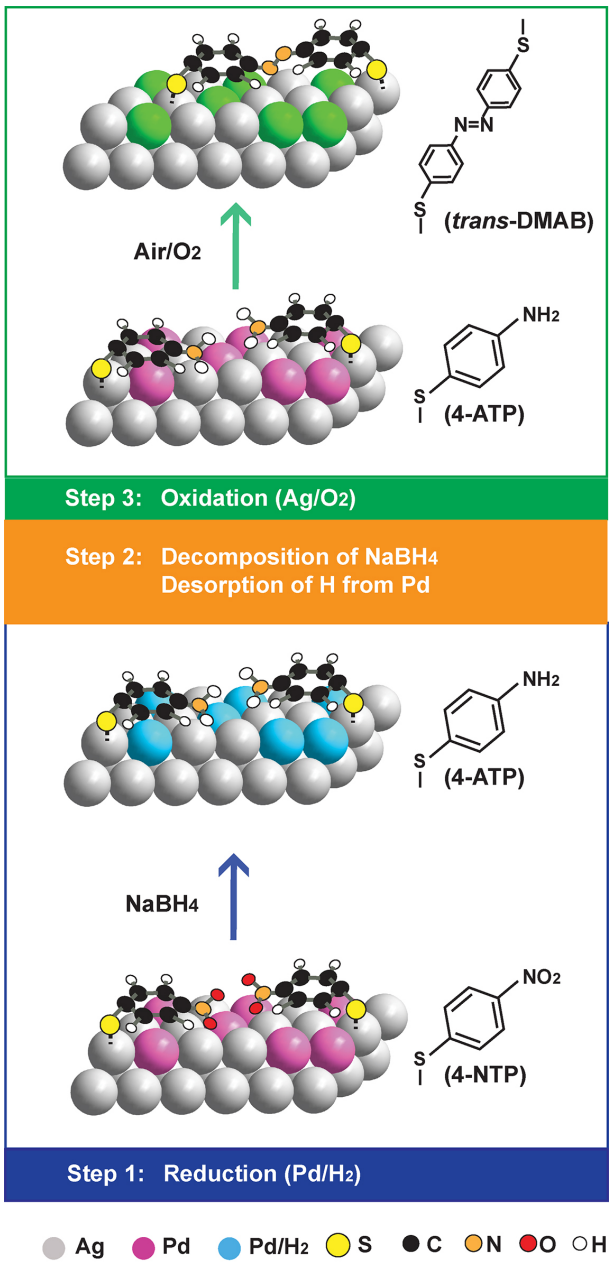

Figure 2.8. The proposed mechanism of stepwise reactions involving the Pd-catalyzed reduction of 4-NTP by $NaBH_4$ and Ag-catalyzed oxidation of 4-ATP by the O_2 from air.

their adsorption and dissociation on the Pd surface to generate H atoms.[34] The atomic hydrogen can quickly reduce 4-NTP to 4-ATP. In the second step, the 4-ATP molecules remain on the surface of the catalyst until the $NaBH_4$ is completely decomposed in the reaction solution. In the final step, the Ag surface activates the O_2 from air,[35] enabling Ag-catalyzed oxidation of 4-ATP to *trans*-DMAB.

2.4 Conclusions

We have discussed two general methods for depositing a second metal on the surfaces of Ag nanocrystals without involving galvanic replacement and thus facile fabrication of bimetallic nanocrystals with a well-defined core-frame or core-shell structure. The success relies on the introduction of a parallel reduction reaction to compete with and thus suppress the galvanic replacement. In one approach, ascorbic acid is used at pH around 11.9 for generating ascorbate monoanion with a strong reduction power and thus defeating the galvanic replacement. Alternatively, the precursor is co-titrated with Ag^+ ions into a suspension of Ag nanocubes in the presence of ascorbic acid at a pH around 3.2. In this case, the presence of sufficient Ag^+ ions can push back the galvanic replacement, facilitating the deposition of an alloy onto the edges, corners, and part of the side faces of Ag nanocubes for the generation of core-frame nanocubes with increasingly thicker ridges. In both cases, the plasmonic properties of the Ag nanocubes are essentially preserved in the core-frame and core-shell nanocubes while the second metal offers new capabilities. As a unique application, we have demonstrated that the Ag@Pd-Ag core-frame nanocubes can serve as a dual catalyst for the Pd-catalyzed reduction of nitroaromatics to aromatic amines and then the Ag-catalyzed oxidation of amines to azo compounds while both reactions can be monitored and analyzed using SERS. The Ag cores can also be selectively

removed by etching to transform the core-frame and core-shell nanocubes into nanoframes and nanoboxes with a highly open structure and novel properties. Ultimately, this work will contribute to the rational design and synthesis of bi- and multi-metallic nanocrystals with diversified compositions regardless of the possible complication from galvanic replacement.

2.5 Notes to Chapter 2

Part of this chapter is adapted from the paper "Enriching Silver Nanocrystals with a Second Noble Metal" published in *Accounts of Chemical Research* and "A Dual Catalyst with SERS Activity for Probing Stepwise Reduction and Oxidation Reactions" published in *ChemNanoMat*.

2.6 References

[1] Rycenga, M.; Cobley, C. M.; Zeng, J.; Li, W.; Moran, C. H.; Zhang, Q.; Qin, D.; Xia, Y., Controlling the Synthesis and Assembly of Silver Nanostructures for Plasmonic Applications. *Chem. Rev.* **2011**, *111*, 3669–3712.

[2] Xia, Y.; Xiong, Y.; Lim, B.; Skrabalak, S. E., Shape-Controlled Synthesis of Metal Nanocrystals: Simple Chemistry Meets Complex Physics? *Angew. Chem. Int. Ed.* **2009**, *48*, 60-103.

[3] Wiley, B.; Sun, Y.; Xia Y., Synthesis of Silver Nanostructures with Controlled Shapes and Properties. *Acc. Chem. Res.* **2007**, *40*, 1067–1076.

[4] Xia, X.; Zeng, J.; McDearmon, B.; Zheng, Y.; Li, Q.; Xia, Y., Silver Nanocrystals with Concave Surfaces and Their Optical and Surface-Enhanced Raman Scattering Properties. *Angew. Chem. Int. Ed.* **2011**, *123*, 12542–12546.

[5] McLellan, J. M.; Siekkinen, A.; Chen, J.; Xia, Y., Comparison of the Surface-Enhanced Raman Scattering on Sharp and Truncated Silver Nanocubes. *Chem. Phys. Lett.* **2006**, *427*, 122–126.

[6] Christopher, P.; Xin, H.; Linic, S., Visible-Light-Enhanced Catalytic Oxidation Reactions on Plasmonic Silver Nanostructures. *Nat. Chem.* **2011**, *3*, 467–472.

[7] Gilroy, K. D.; Ruditskiy, A.; Peng, H. C.; Qin, D.; Xia, Y., Bimetallic Nanocrystals: Syntheses, Properties, and Applications. *Chem. Rev.* **2016**, *116*, 10414–10472.

[8] Link, S.; Wang, Z. L.; El-Sayed, M. A., Alloy Formation of Gold−Silver Nanoparticles and the Dependence of the Plasmon Absorption on Their Composition. *J. Phys. Chem. B,* **1999**, *103*, 3529–3533.

[9] Yang, Y.; Liu, J.; Fu, Z.; Qin, D., Galvanic Replacement-Free Deposition of Au on Ag for Core-Shell Nanocubes with Enhanced Chemical Stability and SERS Activity. *J. Am. Chem. Soc.* **2014**, *136*, 8153–8156.

[10] Li, J.; Liu, J.; Yang, Y.; Qin, D., Bifunctional Ag@Pd-Ag Nanocubes for Highly Sensitive Monitoring of Catalytic Reactions by Surface-Enhanced Raman Spectroscopy. *J. Am. Chem. Soc.* **2015**, *137*, 7039−7042.

[11] Sun, Y.; Xia, Y., Mechanistic Study on the Replacement Reaction between Silver Nanostructures and Chloroauric Acid in Aqueous Medium. *J. Am. Chem. Soc.* **2004**, *126*, 3892–3901.

[12] Chen, J.; Wiley, B.; McLellan, J.; Xiong, Y.; Li, Z.-Y.; Xia, Y., Optical Properties of Pd−Ag and Pt−Ag Nanoboxes Synthesized via Galvanic Replacement Reactions. *Nano Lett.* **2005**, *5*, 2058–2062.

[13] Zhang, W.; Yang J.; Lu, X., Tailoring Galvanic Replacement Reaction for the Preparation of Pt/Ag Bimetallic Hollow Nanostructures with Controlled Number of Voids. *ACS Nano* **2012**, *6*, 7397–7405.

[14] Sun, Y.; Tao, Z.; Chen, J.; Herricks, T.; Xia, Y., Ag Nanowires Coated with Ag/Pd Alloy Sheaths and Their Use as Substrates for Reversible Absorption and Desorption of Hydrogen. *J. Am. Chem. Soc.* **2004**, *126*, 5940–5941.

[15] Sutter, E.; Jungjohann, K.; Bliznakov, S.; Courty, A.; Maisonhaute, E.; Tenney, S.; Sutter, P., *In situ* Liquid-Cell Electron Microscopy of Silver-Palladium Galvanic Replacement Reactions on Silver Nanoparticles. *Nat. Commun*. **2014**, *5*, 4946.

[16] Sanedrin, R. G.; Georganopoulou, D. G.; Park, S.; Mirkin, C. A., Seed-Mediated

Growth of Bimetallic Prisms. *Adv. Mater.* **2005**, 17, 1027–1031.

[17] McEachran, M.; Keogh, D.; Pietrobon, B.; Cathcart, N.; Gourevich, I.; Coombs, N.; Kitaev, V., Ultrathin Gold Nanoframes through Surfactant-Free Templating of Faceted Pentagonal Silver Nanoparticles. *J. Am. Chem. Soc.* **2011**, *126*, 8066–8069.

[18] Shahjamali, M. M.; Bosman, M.; Cao, S.; Huang, X.; Saadat, S.; Martinsson, E.; Aili, D.; Tay, Y. Y.; Liedberg, B.; Loo, S. C. J.; Zhang, H.; Boey, F.; Xue, C., Gold Coating of Silver Nanoprisms. *Adv. Funct. Mater.* **2012**, *22*, 849–854.

[19] Gao, C.; Lu, Z.; Liu, Y.; Zhang, Q.; Chi, M.; Cheng, Q.; Yin, Y., Highly Stable Silver Nanoplates for Surface Plasmon Resonance Biosensing. *Angew. Chem. Int. Ed.* **2012**, *51*, 5629–5633.

[20] Murshid, N.; Gourevich, I.; Coombs, N.; Kitaev, V., Gold Plating of Silver Nanoparticles for Superior Stability and Preserved Plasmonic and Sensing Properties. *Chem. Commun.* **2013**, 49, 11355–11357.

[21] Liu, H.; Liu, T.; Zhang, L.; Han, L.; Gao, C.; Yin, Y., Etching-Free Epitaxial Growth of Gold on Silver Nanostructures for High Chemical Stability and Plasmonic Activity. *Adv. Funct. Mater.* **2015**, *25*, 5435–5443.

[22] Sun, X.; Yang, Y.; Zhang, Z.; Qin, D., On the Mechanistic Roles of Hydroxide in Controlling the Deposition of Gold on Colloidal Silver Nanocrystals. *Chem. Mater.* **2017**, *27*, 4014–4021.

[23] Gilroy, K. D.; Hughes, R. A.; Neretina, S., Kinetically Controlled Nucleation of Silver on Surfacant-Free Gold Seeds. *J. Am. Chem. Soc.* **2014**, *136*, 15337–15345.

[24] Zhang, Q.; Li, W.; Wen, L.-P.; Chen, J.; Xia, Y., Facile Synthesis of Ag Nanocubes of 30 to 70 nm in Edge Length with CF_3COOAg as a Precursor. *Chem. Eur. J.* **2010**, *16*, 10234-10239.

[25] Sun, X.; Qin, D., Co-Titration of $AgNO_3$ and $HAuCl_4$: A New Route to the Synthesis of Ag@Ag–Au Core–frame Nanocubes with Enhanced Plasmonic and Catalytic Properties. *J. Mater. Chem. C* **2015**, *3*, 11833–11841.

[26] Li, J.; Sun, X.; Qin, D., Ag-Enriched Ag-Pd Bimetallic Nanoframes and Their Catalytic Properties. *ChemNanoMat* **2016**, *2*, 494−499.

[27] Schlücker, S., Surface-Enhanced Raman Spectroscopy: Concepts and Chemical Applications. *Angew. Chem. Int. Ed.* **2014**, *53*, 4756–4795.

[28] Li, J.; Wu, Y.; Sun, X.; Liu, J.; Winget, S. A.; Qin, D., A Dual Catalyst with SERS Activity for Probing Stepwise Reduction and Oxidation Reactions. *ChemNanoMat* **2016** *2*, 786−790.

[29] Zhao, L. B.; Chen, J. L.; Zhang, M.; Wu, D. Y.; Tian, Z. Q., Theoretical Study on Electroreduction of *p*−Nitrothiophenol on Silver and Gold Electrode Surfaces. *J. Phys. Chem. C* **2015**, *119*, 4949−4958.

[30] Huang, Y. F.; Wu, D. Y.; Zhu, H. P.; Zhao, L. B.; Liu, G. K.; Ren, B.; Tian, Z. Q., Surface-Enhanced Raman Spectroscopic Study of *p*−Aminothiophenol. *Phys. Chem. Chem. Phys.* **2012**, *14*, 8485−8497.

[31] Stuart, C. M.; Frontiera, R. R.; Mathies, R. A., Excited−State Structure and Dynamics of *cis*- and *trans*-Azobenzene from Resonance Raman Intensity Analysis. *J. Phys. Chem. A* **2007**, *111*, 12072−12080.

[32] Joseph, V.; Engelbrekt, C.; Zhang, J.; Gernert, U.; Ulstrup, J.; Kneipp, J., Characterizing the Kinetics of Nanoparticle-Catalyzed Reactions by Surface-Enhanced Raman Scattering. *Angew. Chem. Int. Ed.* **2012,** *51*, 7592-7596.

[33] McLellan, J. M.; Xiong, Y.; Hu, M.; Xia, Y., Surface-Enhanced Raman Scattering of 4-Mercaptopyridine on Thin Films of Nanoscale Pd Cubes, Boxes, and Cages. *Chem. Phys. Lett.* **2006**, *417*, 230-234.

[34] Nakatsuji, H.; Hada, M.; Yonezawa, T., Theoretical Study on the Chemisorption of a Hydrogen Molecule on Palladium. *J. Am. Chem. Soc.* **1987***, 109*, 1902−1912.

[35] Yu, W.; Mullen, G. M.; Mullin, C. B., Hydrogen Adsorption and Absorption with Pd–Au Bimetallic Surfaces. *J. Phys. Chem. C* **2013**, *117*, 19535–19543.

CHAPTER 3. BIFUNCTIONAL AG@SiO_2/AU NANOPARTICLES FOR PROBING SEQUENTIAL CATALYTIC REACTIONS BY SURFACE-ENHANCED RAMAN SPECTROSCOPY

3.1 Introduction

Noble-metal nanocrystals have found applications in areas ranging from catalysis to photonics, electronics, sensing, imaging, and biomedical research.[1-5] As discussed in Chapter 1, bimetallic nanocrystals, in particular, have received ever growing interest in recent years because of their enhanced properties relative to their monometallic counterparts.[6-10] By controlling the ratio and spatial distributions of the elements, one can engineer and enrich the properties of bimetallic nanocrystals to greatly expand their scope of applications. One of intriguing bimetallic systems is based upon Ag and Au. Silver nanocrystals embrace localized surface plasmon resonance (LSPR) in the visible region for surface-enhanced Raman scattering (SERS),[11,12] and they can also serve as a superb catalyst for oxidation reactions, including the epoxidation of ethylene by O_2.[13] On the other hand, Au is well known for its intrinsic inertness. However, it has been demonstrated that the catalytic activity of Au can be drastically enhanced by substantially downsizing the nanoparticles.[14-17] To this end, Haruta *et al.* discovered that the catalytic activity of TiO_2-supported Au nanoparticles toward CO oxidation increased significantly as their sizes were reduced down to 5 nm and below.[15] In principle, by simply coating the surface of Ag nanocrystals with discrete Au islands of less than 5 nm in size, one could design a useful

bimetallic system with a unique integration of SERS and catalytic properties originating from the Ag and Au components, respectively.

Although it appears straightforward to prepare the aforementioned Ag-Au bimetallic system, the synthesis inherits a number of challenges. As discussed in Chapter 2, the galvanic replacement between Ag and $AuCl_4^-$ precludes the use of a protocol that involves the reduction of $AuCl_4^-$ in the presence of Ag nanocrystals.[18] Even when the galvanic replacement is suppressed through the introduction of a strong reducing agent, the deposition of Au atoms tends to take a layer-by-layer rather than island growth mode.[19] It is possible to deposit pre-synthesized Au nanoparticles onto the surface of Ag nanocrystals through careful manipulation of surface charges, but it will be difficult to prevent the Au nanoparticles from touching and merging into larger structures. In addition, the tiny Au particles with an enormous surface-to-volume ratio have a strong tendency to coagulate during operation, ultimately losing their catalytic activity. One approach to improve the stability against coagulation is to encapsulate the Au nanoparticles with a thin, porous oxide layer, such as SiO_2, SnO_2, CeO_2, or TiO_2. To this end, it has been demonstrated that the oxide layer could serve as a physical barrier to isolate and confine the metal nanoparticles for a variety of systems.[19-25] However, the presence of an oxide layer tends to block the active sites on metal nanoparticles, leading to reduction in catalytic activity when compared with the naked metal nanoparticles.

In this chapter, we report a rational approach to synthesize $Ag@SiO_2$/Au nanoparticles that consist of Au nanoparticles on the surface of Ag nanocubes that are isolated from each other, but not fully covered, by SiO_2. We start with a Stöber process to deposit a thin layer of SiO_2 on the surface of Ag nanocubes to generate $Ag@SiO_2$ core-

shell nanocubes.[26] We then titrate aqueous $HAuCl_4$ into an aqueous suspension containing $Ag@SiO_2$ nanocubes, ascorbic acid (H_2Asc, a reducing agent), poly(vinyl pyrrolidone) (PVP, a colloidal stabilizer), and sodium hydroxide (NaOH) at pH=11.9. The OH^- ions can chemically etch the SiO_2 shell to generate pathways for the reagents to directly access the surface of the Ag nanocube.[27] In the presence of H_2Asc, $AuCl_4^-$ could be reduced to generate $AuCl_2^-$.[28] The galvanic replacement reaction between Au^{3+}/Au^+ and Ag then quickly initiates the nucleation and deposition of Au atoms on the surface of Ag nanocube. Afterwards, the pores within the SiO_2 shell are gradually filled by the Au atoms derived from the reduction of Au^{3+}/Au^+ by H_2Asc, leading to the formation of discrete, well-defined Au islands immersed in a sea made of SiO_2. We confirm the catalytic activity of the Au islands using the reduction of 4-nitrophenol (4-NP) to 4-aminophenol (4-AP) by $NaBH_4$. We also demonstrate that the bimetallic nanoparticles embrace SERS activity, which is 10-fold stronger than that of the $Ag@SiO_2$ nanocubes. Remarkably, the integrated catalytic and SERS properties of these nanoparticles can be used for *in situ* SERS probing of the Au-catalyzed reduction of 4-nitrothiophenol (4-NTP) by $NaBH_4$ and the Ag-catalyzed oxidation of 4-aminothiophenol (4-ATP) by O_2 from air.

3.2 Experimental Section

Chemicals and Materials. Poly(vinyl pyrrolidone) with an average molecular weight of 29,000 (PVP-29K) or 55,000 (PVP-55K), aqueous hydrochloric acid (HCl, 37%), silver trifluoroacetate (CF_3COOAg, ≥99.99% trace metal basis), sodium hydrosulfide hydrate ($NaHS \cdot xH_2O$), gold(III) chloride trihydrate ($HAuCl_4 \cdot 3H_2O$, ≥99.9% trace metal basis), L-ascorbic acid (H_2Asc, 98%), ethanol (CH_3CH_2OH, 200 proof),

tetraethyl orthosilicate (TEOS, 99.0%), aqueous ammonia solution (28.0–30.0%), sodium borohydride ($NaBH_4$, 99.99%), and 4-nitrophenol (4-NP, $C_6H_5NO_3$) were all purchased from Sigma Aldrich. Ethyl glycol ($HOCH_2CH_2OH$, EG) was obtained from J. T. Baker. Acetone (C_3H_6O, HPLC grade, 99.5+%), sodium hydroxide (NaOH, 98%), 1,4-benzenedithiol (1,4-BDT, $C_6H_6S_2$, 97%), and 4-aminothiophenol (4-ATP, C_6H_7NS, 97%) were obtained from Alfa Aesar. 4-Nitrothiophenol (4-NTP, $C_6H_5NO_2S$) was purchased from Oakwood Chemical. All chemicals were used as received. All aqueous solutions were prepared using deionized (DI) water with a resistivity of 18.2 MΩ·cm at room temperature.

Synthesis of Ag Nanocubes. The Ag nanocubes of 38.6±1.8 nm in edge length were prepared by following a protocol that involves the reduction of CF_3COOAg with EG in the presence of NaHS and HCl.[29] Finally, the Ag nanocubes were dispersed in DI water at a concentration of 6.9×10^{12} particles/mL.

Synthesis of Ag@SiO_2 Nanocubes. In a typical synthesis, 33.8 μL of the suspension of Ag nanocubes was dispersed into 200 μL of DI water, followed by the addition of 6 mL ethanol and 400 μL of PVP-55K aqueous solution (2 mg/mL). The solution was subject to magnetic stirring at 950 rpm for 30 min at room temperature. Next, 6 mL of ethanol and 1 mL of DI were introduced sequentially, followed by the quick addition of 280 μL of aqueous ammonia (30%) and 400 μL of TEOS (4% in ethanol). After reaction for 4 h, we collected the particles by centrifugation at 9000 rpm for 15 min, washed with ethanol three times and re-dispersed in DI water for future use.

Synthesis of Ag@SiO_2/Au Nanoparticles. In a typical synthesis, 2 mL of aqueous PVP-29K (1 mM), 0.5 mL of aqueous H_2Asc (100 mM) and 0.5 mL of aqueous NaOH

(200 mM) solution were introduced sequentially into a 23-mL glass vial under magnetic stirring, followed by the addition of 60 μL of the suspension of $Ag@SiO_2$ nanocubes. Next, different volume (0.2 mL, 0.4 mL, or 0.8 mL) of aqueous $HAuCl_4$ (0.1 mM) was titrated into the reaction solution at 0.02 mL/min using a syringe pump. The reaction solution was magnetically stirred for another 10 min upon completion of titration. The particles were collected by centrifugation at 6000 rpm for 15 min, washed with DI water three times and re-dispersed in DI water for future use.

XPS Analysis of $Ag@SiO_2$/Au Nanoparticles. Approximately 20 μL of the as-prepared sample suspension was drop casted on the surface of a 1×1 cm^2 silicon wafer and allowed to dry overnight under ambient conditions in air. The sample was then loaded into of a Thermo K-Alpha X ray photoelectron spectrometer and the Au4*f* (79–99 eV) and Ag3*d* (360–380 eV) regions of the sample were measured with a 0.1 eV resolution.

Catalytic Characterization of $Ag@SiO_2$/Au Nanoparticles. In a typical measurement, 2 mL of aqueous 4-NP (0.2 mM), 5 mL of DI water, 1 mL of aqueous $NaBH_4$ (20 mg/mL, freshly prepared, ice cold) were introduced into a 23-mL glass vial under magnetic stirring. Upon addition of the $Ag@SiO_2$/Au nanoparticles ($\sim10^{11}$ particles), we monitored the reaction by withdrawing 1 mL of reaction solution every several minutes to collect UV-vis spectra.

Duration Test of $Ag@SiO_2$/Au Nanoparticles. First, 2 mL of aqueous 4-NP (0.2 mL), 5 mL of DI water, and 1 mL of aqueous $NaBH_4$ (20 mg/mL, freshly prepared, ice cold) were introduced into a 23-mL glass vial under magnetic stirring. Next, the $Ag@SiO_2$/Au nanoparticles were introduced into the reaction solution and UV-vis spectra

were recorded every several minutes. After the reaction had slowed down, the nanoparticles were collected using centrifugation at 15000 rpm for 15 min and re-dispersed in 1 mL of DI water. UV-vis was used to confirm the number of the nanoparticles. Repeat the catalytic reaction using the recycled nanoparticles for two times.

SERS of 1,4-BDT. The Ag nanocubes, Ag@SiO_2 nanocubes, and Ag@SiO_2/Au nanoparticles were incubated with 1,4-BDT (4×10^{-4} M in ethanol) for 1 hour. After washing with DI water three times, the functionalized nanoparticles were re-dispersed in 1 mL of DI water, respectively, maintaining a similar concentration of 10^{12} particles per mL. An aliquot of 20 μL was withdrawn from the solution and placed into a polydimethylsiloxane (PDMS) cell for all measurements. The Raman spectra were recorded using Renishaw inVia Raman spectrometer coupled with a Leica microscope with a 100× objective lens. The laser excitation wavelength was 532 nm, together with a laser power output of 50 mW and a collection time of 30 s.

***In situ* SERS Monitoring of the Reaction Involving 4-NTP or 4-ATP.** The Ag@SiO_2/Au nanoparticles were dispersed in 2.5 mL of 4-NTP (10^{-6} M in ethanol) for 1 h. After the incubation, the particles were collected by centrifugation at 5000 rpm for 15 min and washed with DI water two times. The particles were re-dispersed in 1 mL of DI water. After mixing 200 μL of 4-NTP-functionalized-Ag@SiO_2/Au nanoparticles and 200 μL of aqueous $NaBH_4$ (0.1 mg/mL), we withdrew an aliquot of 20 μL from reaction solution every several minutes and placed in PDMS cell to monitor the reaction progress by SERS. The SERS spectra were recorded using a Renishaw inVia Raman spectrometer coupled with a Leica microscope with the use of a 5× objective lens. The laser excitation

wavelength was 532 nm, with a laser power of 50 mW and a collection time of 7 s. The protocol of monitoring reaction of 4-ATP was the same except for the use of a different chemical with a different concentration (10^{-5} mM in ethanol).

Instrumentation and Characterization. We used an Eppendorf 5430 centrifuge for the collection and washing of all samples. The UV-vis spectra were recorded on a Cary 50 spectrometer (Agilent Technologies, Santa Clara, CA). Quantitative measurements of Au and Ag contents were performed using an inductively coupled plasma mass spectrometer (ICP-MS, NexION 300Q, PerkinElmer, Waltham, MA). The XPS spectra were collected using a Thermo K-Alpha X ray photoelectron spectrometer (Thermo Fisher Scientific, Waltham, MA). A Hitachi HT7700 microscope (Hitachi, Tokyo, Japan) operated at 120 kV was used to take transmission electron microscopy (TEM) images. The high-resolution HAADF-STEM imaging and STEM-EELS mapping were conducted on a Hitachi HD2700C STEM operated at 200 kV and equipped with a probe aberration corrector. The SERS spectra were recorded using a Renishaw inVia Raman spectrometer (Wotton-under-Edge, UK) coupled with a Leica microscope (Wetzlar, Germany). The excitation wavelength was 532 nm and the scattered light was dispersed using a holographic notch filter with a grating of 2400 lines/mm.

3.3 Results and Discussion

3.3.1 Deposition of Au on Ag@SiO_2 Nanocubes for Ag@SiO_2/Au Nanoparticles

We followed the published protocols to synthesize the Ag nanocubes (Figure 3.1A) with an average edge length of 38.6±1.8 nm and the Ag@SiO_2 nanocubes (Figure 3.1B) with an oxide shell of 6.0±0.2 nm in thickness, respectively.[29,30] We then dispersed the

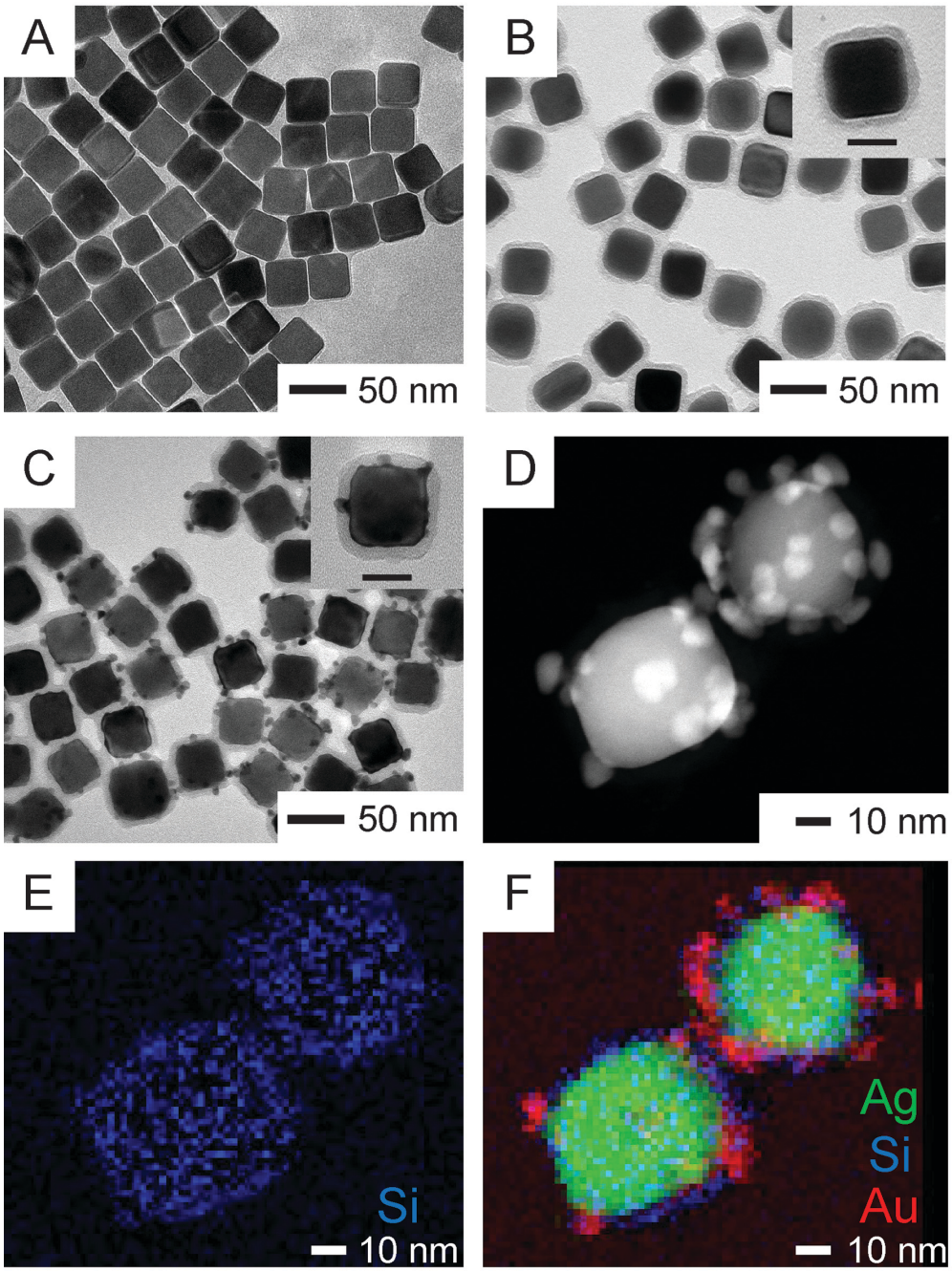

Figure 3.1. TEM images of (A) Ag nanocubes, (B) Ag@SiO_2 nanocubes, and (C) Ag@SiO_2/Au nanoparticles prepared with the titration of 0.4 mL of 0.1 mM aqueous $HAuCl_4$. (D) HAADF-STEM image and (E, F) EELS mapping images of the Ag@SiO_2/Au nanoparticles in (C).

$Ag@SiO_2$ nanocubes in an aqueous solution containing H_2Asc, PVP, and NaOH at pH = 11.9, followed by the titration of aqueous $HAuCl_4$ using a syringe pump at a relatively slow rate under ambient conditions. Figure 3.1C shows a TEM image of the sample obtained after the titration of 0.4 mL aqueous $HAuCl_4$, indicating the formation of Au islands, with sizes ranging from 6 to 12 nm in diameter, over the surface of each $Ag@SiO_2$ nanocube. It should be pointed out that the thickness of the SiO_2 shell remained essentially the same during the transformation of $Ag@SiO_2$ nanocubes into $Ag@SiO_2$/Au nanoparticles (see the insets of Figure 3.1, B and C). Figure 3.1D shows a high-angle annular dark field scanning TEM (HAADF-STEM) image of two $Ag@SiO_2$/Au nanoparticles, from which we could simply distinguish Au from Ag by contrast. As shown in Figure 3.1, E and F, electron energy-loss spectroscopy (EELS) mapping of these two nanoparticles clearly confirmed the generation of discrete Au islands directly on the surface of each Ag nanocube, with SiO_2 serving as a spacer among the islands.

We also used high-resolution HAADF-STEM to resolve the interface at which the growth of Au was instigated. As shown in Figure 3.2, A and B, the Au atoms directly nucleated and grew from the surface of the Ag nanocube encapsulated in the SiO_2 shell. Figure 3.2, C–E, shows the STEM-EELS mapping of Au, Ag, and Si, respectively. We confirmed that the initial deposition of Au atoms was indeed initiated from the surface of the Ag nanocube, followed by the continuous growth into a Au island (Figure 3.2C). There was a detectable layer of Ag on top of the outermost surface of the Au island (Figure 3.2D). The silica layer was retained on the surface of the Ag nanocube, with very little coverage on the Au island (Figure 3.2E). However, it is difficult, if not impossible, to clearly resolve any silica layer on the outermost surface of the Au island. Taken together, we believe that

the Au nanoparticles and SiO_2 shell were situated on the surface of each Ag nanocube with an "islands in a sea" configuration (Figure 3.2F).

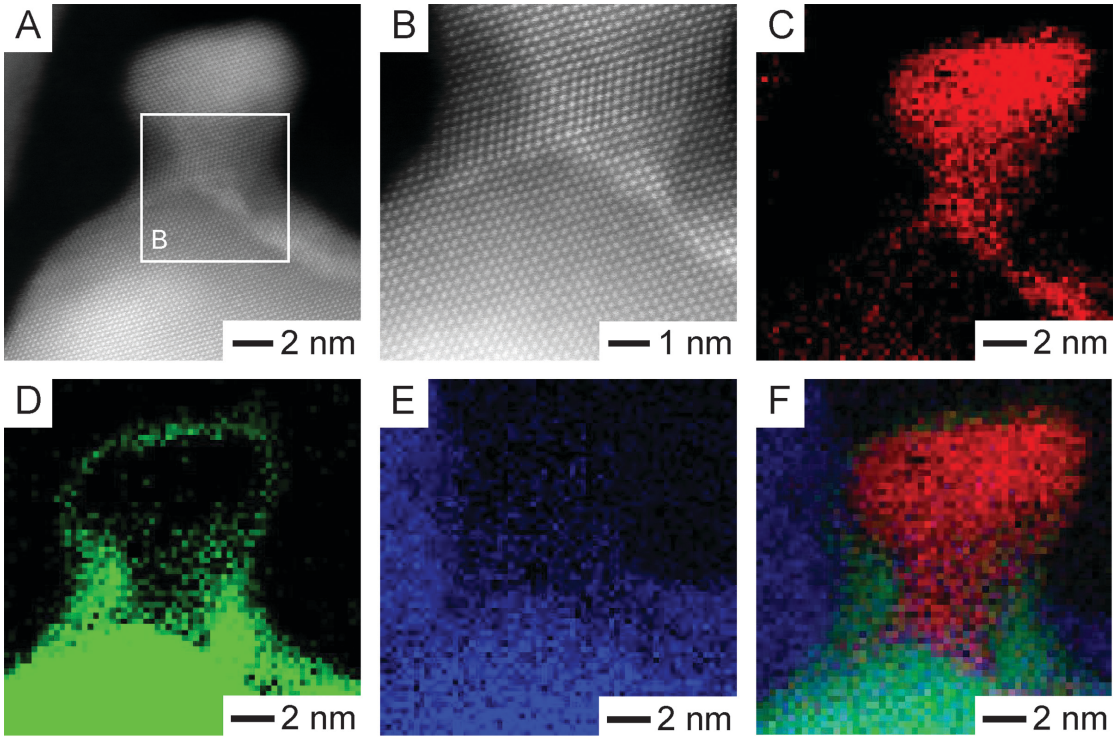

Figure 3.2. (A, B) HAADF-STEM images, at two different magnifications, of a Au island on the surface of a Ag@SiO_2/Au nanoparticle that was prepared with the titration of 0.4 mL of 0.1 mM aqueous $HAuCl_4$. (C–F) STEM–EELS elemental mapping of Au (red), Ag (green), and Si (blue), respectively, of the Au island.

3.3.2 Proposed Mechanism of the Transformation of Ag@SiO_2 Nanocubes to Ag@SiO_2/Au Nanoparticles

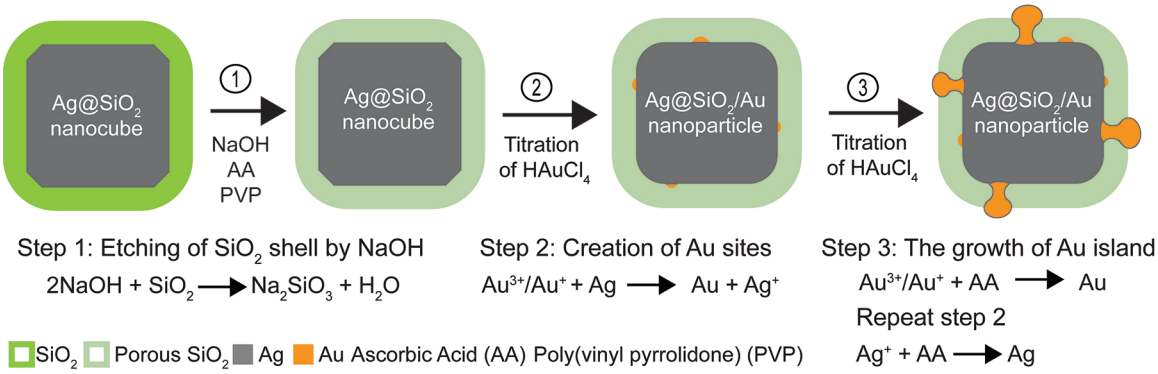

Figure 3.3. Schematic illustration of all the major steps and reactions involved in the fabrication of Ag@SiO_2/Au nanoparticles.

Figure 3.3 illustrates a mechanism proposed to account for the formation of Ag@SiO_2/Au nanoparticles. In the first step, small pores are generated *in situ* in the SiO_2 shell due to chemical etching by NaOH.[27] We argue that such pores ultimately determine the sites for the nucleation and epitaxial growth of Au islands on the surface of each Ag nanocube. In the second step, upon the titration of aqueous $HAuCl_4$ in the presence of H_2Asc, it is possible that Au^{3+} would be reduce to generate Au^+.[28] These Au^{3+}/ Au^+ ions would diffuse through the pores to react with the Ag surface *via* galvanic replacement for the initial deposition of Au atoms on the surface of each Ag nanocube at the expenses of Ag atoms from the nanocube, leading to the formation of a Ag core slightly deviated from the cubic shape (see Figure 3.1C). We suspect that these dissolved Ag^+ ions could then react with OH^- for the generation of Ag_2O patches on the surface of Ag nanocubes, preventing the underlying Ag from further reaction with Au^{3+}/Au.[31] In the third step, as the titration of $HAuCl_4$ is continued, the Au atoms derived from the reduction of Au^{3+}/ Au^+ by

both H_2Asc and Ag will result in the formation of Au islands that pass through and eventually protrude from the SiO_2 shell, leading to the generation of $Ag@SiO_2/Au$ nanoparticles with an "islands in the sea" structure. Likely, some Ag^+ ions in the reaction solution were, in turn, reduced by H_2Asc to generate Ag atoms, followed by their deposition onto the surface of Au islands (see Figure 3.2D). These results also support our argument that the H_2Asc was in proximity to the surface of Ag nanocubes, facilitating the reduction of Au^{3+}/Au^+ ions for the continuous growth of Au islands as more $HAuCl_4$ was titrated into the reaction solution. It is worth mentioning that, during the growth of Au islands, galvanic replacement reaction would create new sites for the epitaxial growth of more Au islands on the surface of each Ag nanocube. As a result, we obtained $Ag@SiO_2/Au$ nanoparticles with variations in both number and size for the Au islands among different particles (see Figure 3.1C).

To further validate our hypothesis, we collected another two data points with the titration volume of $HAuCl_4$ at 0.2 and 0.8 mL, respectively, while keeping all other experimental parameters unaltered. Figure 3.4 shows TEM and SEM images of the as-obtained samples. With an increase in titration volume, the products showed an increase in both the coverage of Au islands on each Ag nanocube and the size of individual Au islands. Our inductively coupled plasma mass spectroscopy (ICP-MS) analyses indicate that 88% of the added $HAuCl_4$ was reduced to Au atoms, followed by their deposition onto the Ag nanocubes. As expected, the longer reaction time for the case of 0.8 mL of $HAuCl_4$ would create more nucleation sites for the growth of Au islands, in addition to their increase in size. We also used XPS to analyze the Au deposited on the Ag nanocubes (Figure 3.5). We found that the amount of Au increased with the titration volume. Additionally, the

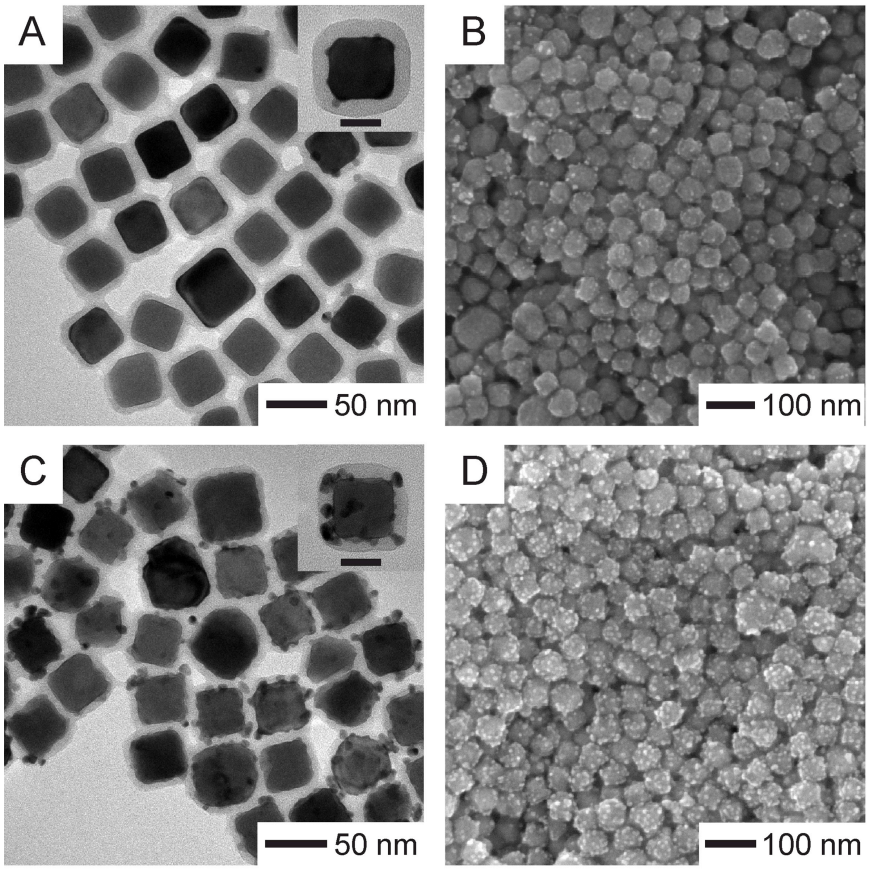

Figure 3.4. (A, C) TEM and (B, D) SEM images of the Ag@SiO_2/Au nanoparticles prepared with the titration of 0.2 mL and 0.8 mL of 0.1 mM $HAuCl_4$, respectively, in the presence of H_2Asc, PVP, and NaOH at pH=11.9.

gaps between the $3d_{5/2}$ and $3d_{3/2}$ peaks of Ag (Δ=6.0 eV) and those between the $4f_{7/2}$ and $4f_{5/2}$ peaks of Au (Δ=3.7 eV) are exactly the same as the values for zero-valent Au and Ag (Table 3.1),[32] suggesting the presence of Au and Ag atoms in a zero-valent state for both samples. During the titration process, we found that the pH was slightly dropped from 11.9 to 11.7, 11.3, 10.2 at titration of volumes of 0.2, 0.4, 0.8 mL, respectively. As a result, we believe that the reducing power of H_2Asc would drop slightly during the titration process.

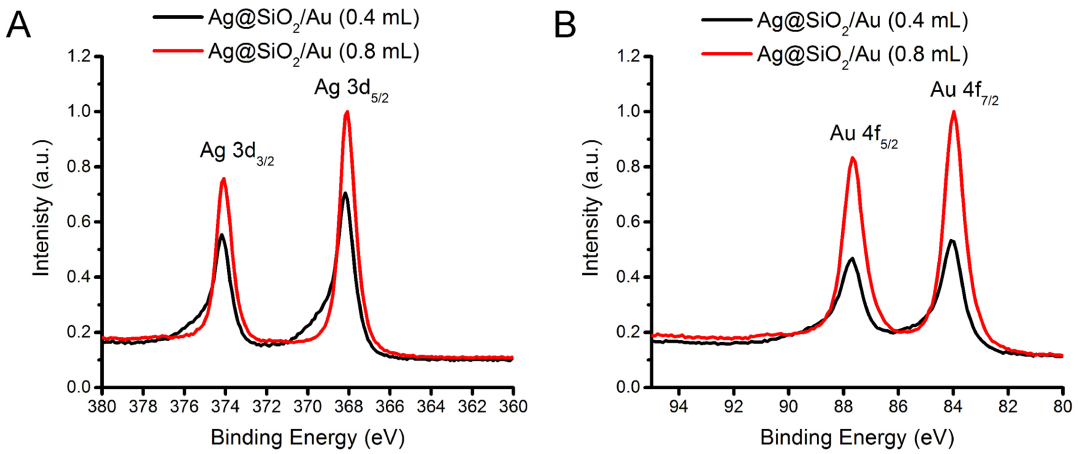

Figure 3.5. XPS of the $Ag@SiO_2/Au$ nanoparticles prepared with the titration of 0.4 mL and 0.8 mL of 0.1 mM $HAuCl_4$, respectively, in the presence of H_2Asc, PVP, and NaOH at pH=11.9.

Table 3.1. The XPS peak positions measured for Au^0 and Ag^0, with reference to bulk standards.

	Au*4f*$_{5/2}$	**Au4*f*$_{7/2}$**	**Δ**	**Ag3*d*$_{3/2}$**	**Ag3*d*$_{5/2}$**	**Δ**
0.4 mL	87.7	84.0	3.7	374.2	368.2	6.0
0.8 mL	87.7	84.0	3.7	374.1	368.1	6.0
Au bulk[32]	87.7	84.0	3.7	n/a	n/a	n/a
Ag bulk[32]	n/a	n/a	n/a	374.3	368.3	6.0

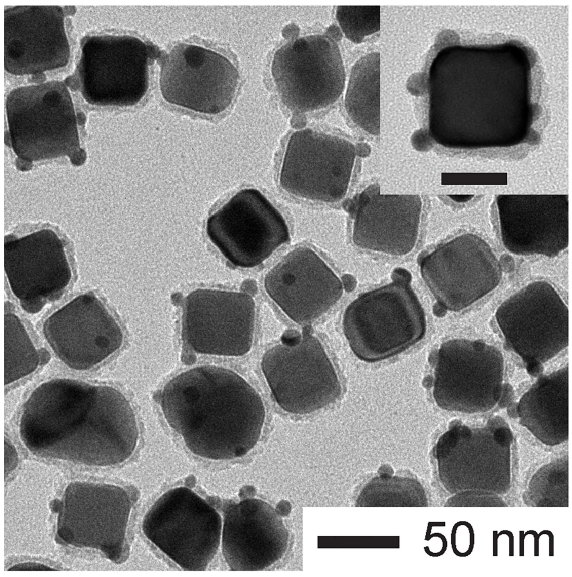

Figure 3.6. TEM image of the Ag@SiO_2/Au nanoparticles prepared with the titration of 0.8 mL of 0.1 mM $HAuCl_4$ in the presence of H_2Asc, PVP, and NaOH at pH=10.3.

To further understand the role of pH in controlling the generation of Ag@SiO_2/Au nanoparticles, we performed another experiment by titrating aqueous $HAuCl_4$ into an aqueous suspension of Ag@SiO_2 in the presence of H_2Asc and PVP at pH = 10.3, with the involvement of 300 μL NaOH (200 mM). Figure 3.6 shows TEM image of the product obtained by at a titration volume of 0.8 mL of $HAuCl_4$, which is similar to those shown in Figure 3.4C. We also conducted a control experiment by titrating aqueous $HAuCl_4$ into an aqueous suspension of Ag@SiO_2 in the presence of H_2Asc and PVP only at pH = 3.1, without the involvement of any NaOH. As shown in Figure 3.7, we observed a mixture of Ag@SiO_2 nanocubes and Au nanoparticles for 0.4 mL and 0.8 mL of $HAuCl_4$, respectively. In this case, the Au nanoparticles were formed through homogenous nucleation and growth

upon the reduction by H_2Asc. Collectively, these results offer addition evidence to support the proposed mechanism.

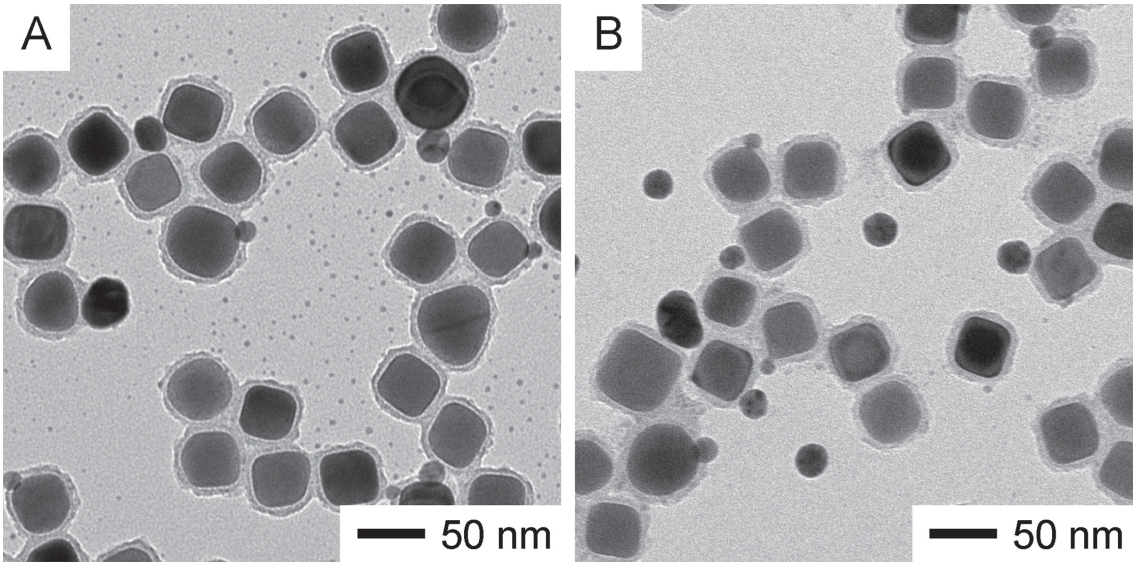

Figure 3.7. TEM image of the $Ag@SiO_2$ nanocubes after reacting with different volumes of 0.1 mM $HAuCl_4$ at (A) 0.4 mL and (B) 0.8 mL, respectively, in the presence of H_2Asc and PVP only.

3.3.3 Catalytic Activity of Ag@SiO₂/Au Nanoparticles toward Reduction of 4-Nitrophenol

We confirmed the catalytic activity of the Au islands towards the reduction of 4-NP to 4-AP by $NaBH_4$.[33] We prepared two samples by fixing the number of $Ag@SiO_2$ nanocubes at $\sim 10^{11}$ to obtain $Ag@SiO_2$/Au nanoparticles at titration volumes of 0.4 mL and 0.8 mL, respectively. The as-obtained samples were directly added as catalysts. Upon

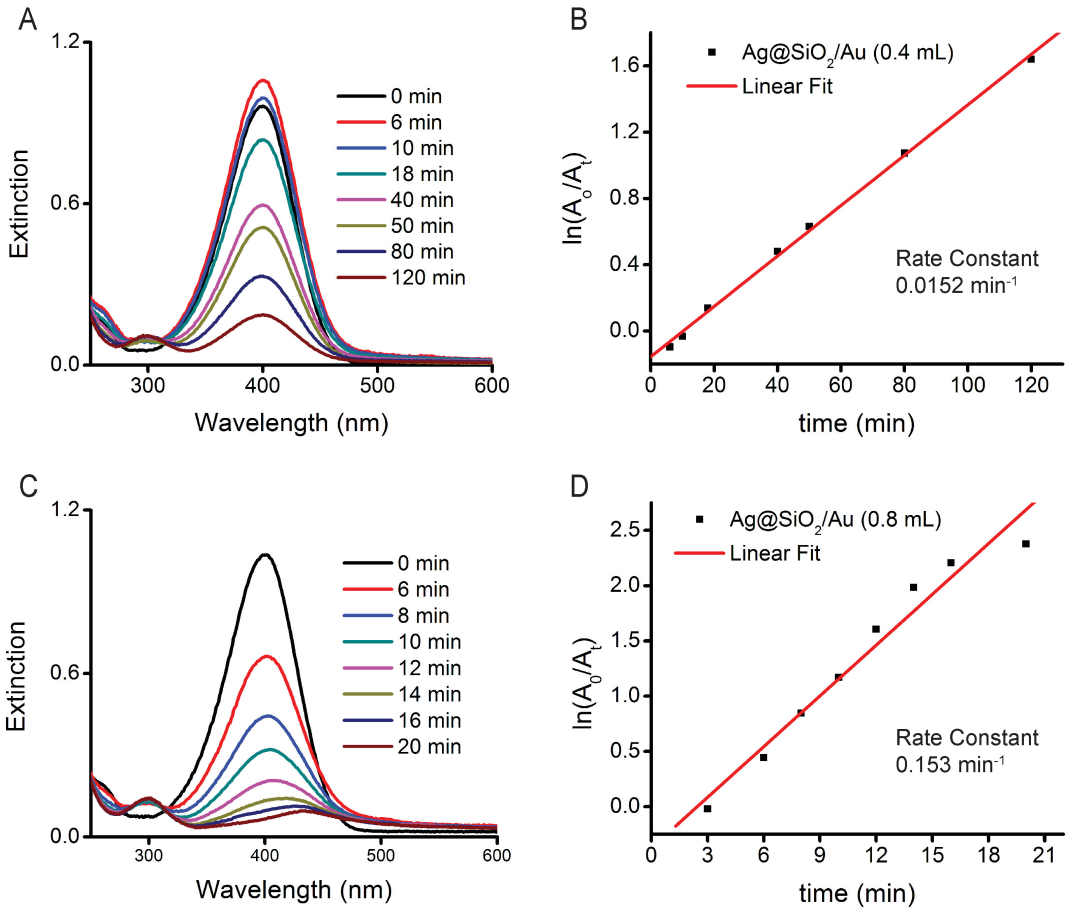

Figure 3.8. (A, C) UV-vis spectra recorded at different time intervals for the reduction of 4-NP by $NaBH_4$ at room temperature, in the presence of $Ag@SiO_2/Au$ nanoparticles as a catalyst. The catalysts were prepared with the titration of (A) 0.4 mL and (C) 0.8 mL, respectively, of 0.1 mM $HAuCl_4$ solution. (B, D) Plots of $\ln[A_0/A_t]$ *versus* time for the peaks located at 400 nm in (A) and (C), respectively.

the introduction of $NaBH_4$, we collected UV-vis spectra of 4-NP at different time intervals (Figure 3.8, A and C). By monitoring the absorption peak at 400 nm, we plotted $\ln(A_t/A_o)$ as a function of reaction time (Figure 3.8, B and D). In both cases, the reduction reaction exhibited first-order kinetics. As a result, we obtained the rate constant through curve fitting. For the $Ag@SiO_2/Au$ nanoparticles prepared at 0.4 mL and 0.8 mL of $HAuCl_4$, the

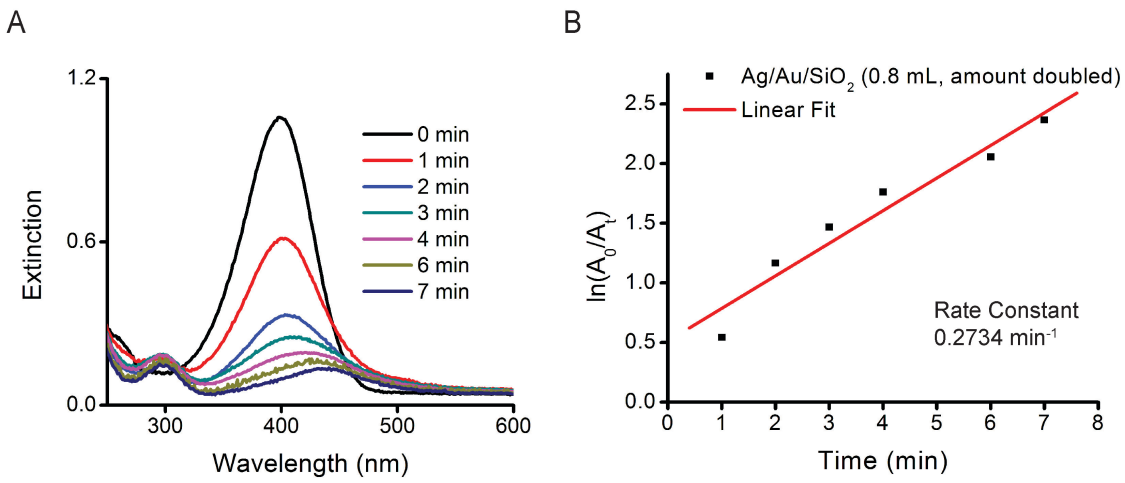

Figure 3.9. (A) UV-vis spectra recorded at different time intervals for the reduction of 4-NP by $NaBH_4$ at room temperature, in the presence of $Ag@SiO_2/Au$ nanoparticles as a catalyst. The catalyst was prepared by using doubled amount of $Ag@SiO_2$ nanocubes with the titration volumes at 0.8 mL for 0.1 mM $HAuCl_4$. (B) plot of $\ln[A_0/A_t]$ *versus* time for the peak located at 400 nm in (A).

rate constants were 0.015 min^{-1} and 0.15 min^{-1}, respectively. These results indicate that the reduction would be accelerated by 10 times when we doubled the titration volume of $HAuCl_4$. As demonstrated in Figure 3.9, the rate constant was further increased to 0.27 min^{-1} when we doubled the number of catalytic particles prepared with 0.8 mL of $HAuCl_4$. These data support our argument that a greater titration volume of the $AuCl_4^-$ precursor would increase both the number and size of Au islands on the surface of each Ag nanocube, ultimately accelerating the reduction kinetics of 4-NP.

For the $Ag@SiO_2/Au$ nanoparticles prepared with 0.8 mL of $HAuCl_4$, we also evaluated their catalytic stability for the reduction of 4-NP by $NaBH_4$. Specifically, after one round of reaction, we collected the catalytic particles and applied them to another round

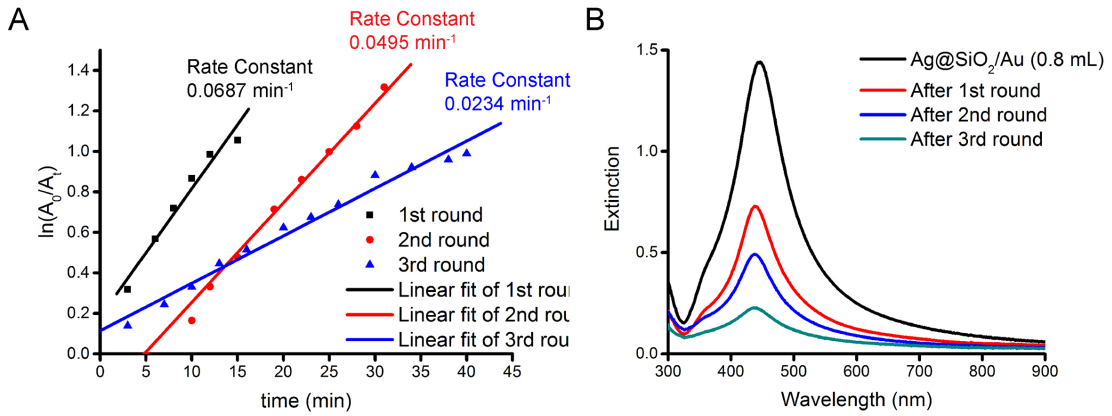

Figure 3.10. (A) Plots of $\ln[A_0/A_t]$ *versus* time for the peak located at 400 nm in UV-vis spectra recorded at different time intervals for the reduction of 4-NP by $NaBH_4$ at room temperature, in the presence of $Ag@SiO_2/Au$ nanoparticles as a catalyst. The initial catalyst was prepared by titrating 0.8 mL of 0.1 mM $HAuCl_4$. After each round, the catalytic particles were collected by centrifugation and re-used for another round of reaction. (B) UV-vis spectra recorded from aqueous suspensions of $Ag@SiO_2/Au$ nanoparticles collected after each round of reaction.

of reaction. As shown in Figure 3.10A, the rate constant dropped from 0.069 to 0.049, and 0.023 min^{-1} after one, two, and three rounds of reaction, respectively. We also collected UV-vis spectra from the $Ag@SiO_2/Au$ nanoparticles after each round of reaction by collecting the solids by centrifugation and re-dispersing them in the same amount of water. As shown in Figure 3.10B, the LSPR peak intensity dropped while the peak position remained unchanged. The drop in LSPR peak intensity can be attributed to the loss of nanoparticles during the centrifugation process. The structure and morphology of the nanoparticles should remain unchanged because the LSPR peak position changed very little. These data are consistent with what is shown in Figure 3.9. When the number of catalytic particles was doubled, the rate constant was almost doubled, increasing from 0.15 to 0.27 min^{-1}. In fact, when we normalized the rate constant against the number of catalytic

particle (based on the LSPR peak intensities in Figure 3.10B), the rate constants became 0.11, and 0.073, and 0.034 for the second and third rounds of reaction.

3.3.4 LSPR and SERS Activities of Ag@SiO_2/Au Nanoparticles

We also characterized the LSPR properties of the Ag@SiO_2/Au nanoparticles. Figure 3.11 shows the UV-vis spectra recorded from aqueous suspensions of the Ag nanocubes, Ag@SiO_2 nanocubes, and the as-obtained Ag@SiO_2/Au nanoparticles prepared at titration volumes of 0.4 mL and 0.8 mL, respectively, for $HAuCl_4$. For the Ag nanocubes, the UV-vis spectrum showed a strong peak at 440 nm (peak #1), one shoulder at 386 nm (peak #2), and a weak peak at 348 nm (peak #3), respectively. Calculations based on the discrete dipole approximation (DDA) method indicates that the physical origins of peaks #1 and #2 can be attributed to dipole resonances,[34] while peak #3 is particularly sensitive to the sharpness of edges and corners of a Ag nanocube. The major dipole resonance (peak #1) was slightly blue shifted from 440 to 438 nm while peak #2 slightly dropped in intensity after SiO_2 coating due to the change in dielectric constant caused by the oxide layer and slight truncation at the corner and edge sites (Figure 3.1B). After the titration of 0.4 mL $HAuCl_4$, peak #1 was further shifted to 433 nm, together with a decrease in intensity for peak #3. Such changes in the LSPR spectrum can be attributed to the increase in truncation at the corner and edge sites (Figure 3.1D). When the volume of $HAuCl_4$ was increased to 0.8 mL, peak #1 was slightly red-shifted from 433 to 438 nm, together with broadening in width. Both changes can be attributed to the increase in both number and volume for the Au islands on each Ag nanocube. Also, peak #3 became undetectable due to continuous truncation to the corners and edges of the Ag core. Collectively, the LSPR spectra also support our results of morphology characterization (see Figure 3.1).

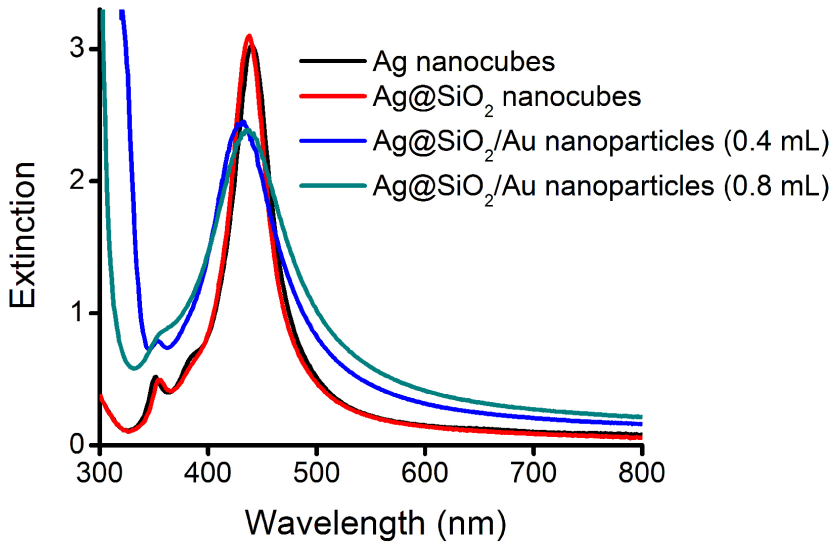

Figure 3.11. UV-vis spectra recorded from aqueous suspensions of Ag nanocubes, $Ag@SiO_2$ nanocubes, and $Ag@SiO_2$/Au nanoparticles prepared with the titration of 0.4 mL and 0.8 mL of 0.1 mM $HAuCl_4$ solution, respectively.

We benchmarked the SERS activity of the $Ag@SiO_2$/Au nanoparticles against those of both Ag and $Ag@SiO_2$ nanocubes. In a typical measurement, we functionalized the nanoparticles with 1,4-benzenedithiol (1,4-BDT) and then collected SERS spectra from the suspensions at an excitation wavelength of 532 nm. As shown in Figure 3.12, the SERS activity of the Ag nanocubes dropped significantly after their surface had been coated with a SiO_2 shell of 6 nm thick. For instance, the intensity of the benzene ring mode at 1564 cm^{-1} decreased by 93.1%, primarily due to the blocking of Ag surface by SiO_2 shell toward the binding of 1,4-BDT probe molecules. Interestingly, some 1,4-BDT molecules could still be trapped in the SiO_2 shell and/or physically adsorbed on the surface, contributing to the observation of weak SERS signals, because these molecules could still feel the enhanced

electromagnetic field on the Ag core.[35] Upon the growth of Au islands in the SiO_2 shells, the intensity of the peak at 1564 cm^{-1} was brought back to a level comparable to that of the Ag nanocubes, corresponding to a 10-fold enhancement relative to that of the $Ag@SiO_2$ nanocubes. In this case, the 1,4-BDT probe molecules were anticipated to bind to the surface of the Au islands. Since the Au islands were directly anchored on the surface of the Ag nanocube, hot spots could be formed at their tips to yield strong SERS.[36,37]

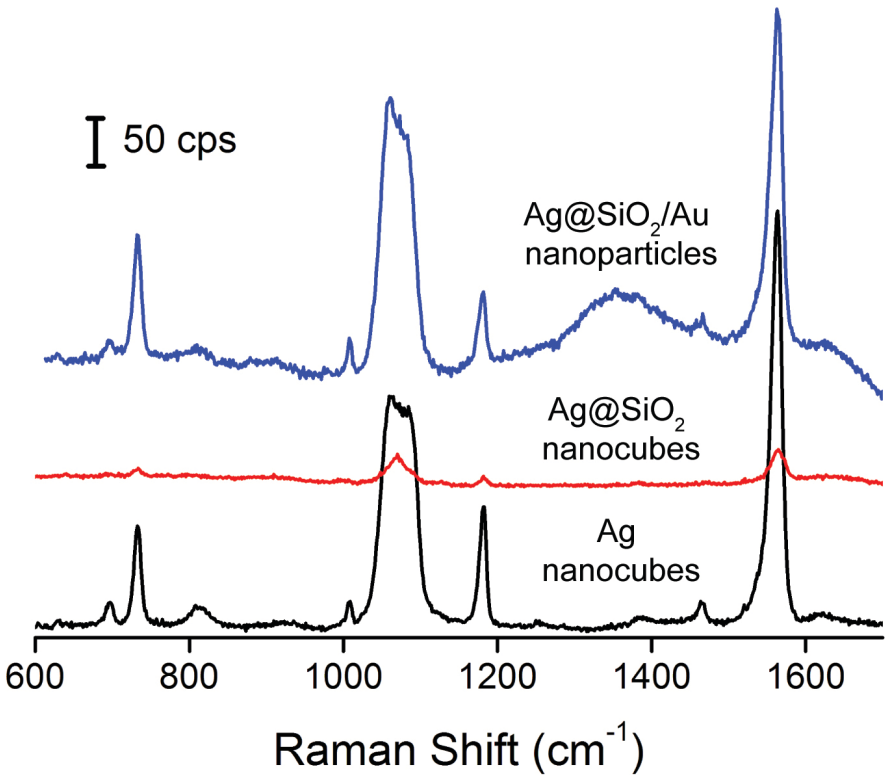

Figure 3.12. SERS spectra collected from 1,4-BDT immobilized on Ag nanocubes, $Ag@SiO_2$ nanocubes, and $Ag@SiO_2$/Au nanoparticles with an excitation wavelength at 532 nm. The $Ag@SiO_2$/Au nanoparticles were prepared with 0.4 mL of 0.1 mM $HAuCl_4$ solution.

3.3.5 Integration of Catalytic and SERS Activities for Probing Sequential Reduction and Oxidation Reactions

By leveraging the catalytic activity of the Au islands and the SERS activity of the Ag core, we further demonstrated the use of the $Ag@SiO_2/Au$ nanoparticles for *in situ* SERS monitoring of the reduction of 4-NTP by $NaBH_4$. In a typical experiment, we prepared $Ag@SiO_2/Au$ nanoparticles with 0.4 mL of $HAuCl_4$ and then functionalized their surfaces with 4-NTP (see 3.2 Experimental Section for details). After initiating the reaction with $NaBH_4$, we collected SERS spectra from the reaction solution at different time intervals at an excitation of 532 nm (Figure 3.13). At t = 0 min, the SERS spectrum shows three characteristic bands of 4-NTP at 1109 cm^{-1} (C-N stretching, ν_{CN}), 1338 cm^{-1} (O-N-O stretching, ν_{NO2}), and 1572 cm^{-1} (C-C stretching, ν_{CC}). The peak located at 1082 cm^{-1} can be assigned to the C-S stretching, ν_{CS}. At t = 9 min, we observed the shift of ν_{NO2} peak from 1338 cm^{-1} to 1328 cm^{-1}, together with a significant drop in peak intensity. For instance, the intensity of ν_{NO2} at 1338 cm^{-1} or ν_{CC} at 1572 cm^{-1} decreased by 94% or 93%, respectively. We suspected that some of the 4-NTP adsorbed on Au islands could be released by $NaBH_4$ due to a stronger binding of BH_4^- to Au surface.[38] At t = 22 min, the three characteristic bands of 4-NTP could no longer be resolved from the spectrum. On the other hand, we observed a small peak at 1594 cm^{-1}, which can be assigned to the ν_{CC} of 4-ATP. Based on our previous findings, the intensity of ν_{CC} for 4-ATP could become one-order of magnitude weaker than that of the band for 4-NTP after the reduction of 4-NTP to 4-ATP by $NaBH_4$.[39-41] From the presence of ν_{CS} band at 1082 cm^{-1}, we argued that some of the 4-ATP molecules were adsorbed on the Au surface. From 22 to 66 min, the SERS spectra remained essentially unaltered. At t = 89 min, four peaks emerged at 1142 cm^{-1},

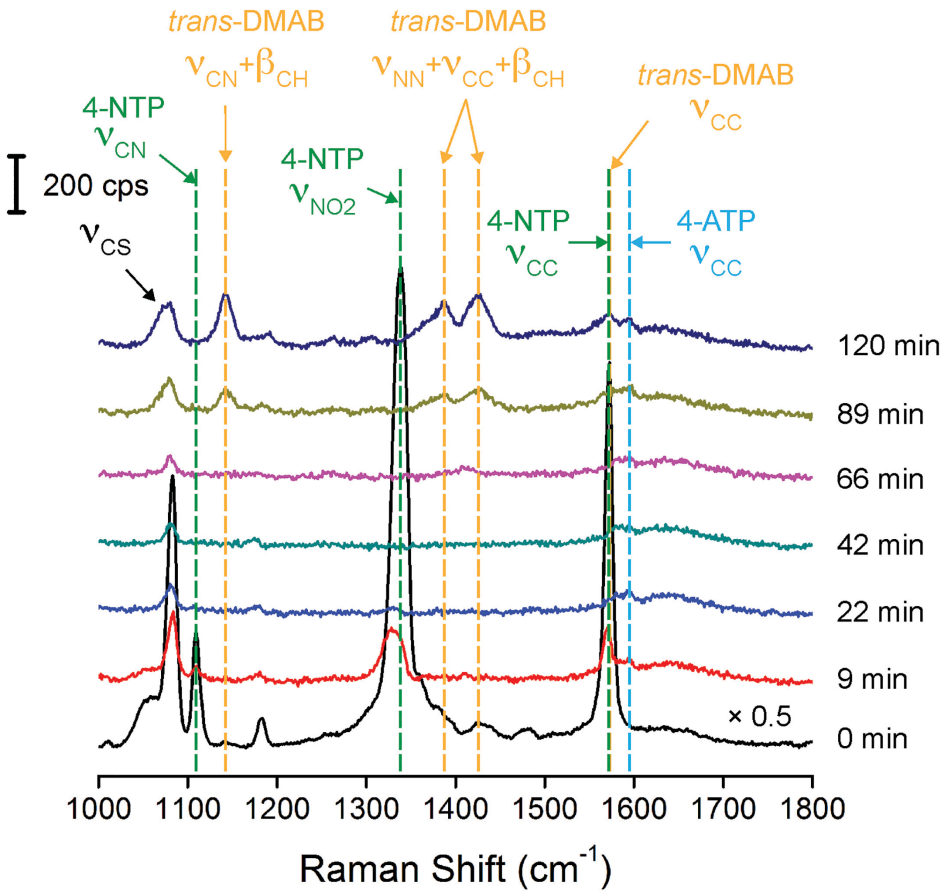

Figure 3.13. SERS spectra collected before and after the introduction of $NaBH_4$ solution into an aqueous suspension of 4-NTP-functionalized $Ag@SiO_2/Au$ nanoparticles at an excitation wavelength of 532 nm. The nanoparticles were prepared with the titration of 0.4 mL of 0.1 mM $HAuCl_4$ solution.

1387 cm^{-1}, 1429 cm^{-1}, and 1574 cm^{-1}, which could be assigned to the $\nu_{CN}+\beta_{CH}$, $\nu_{NN}+\nu_{CN}$, $\nu_{NN}+\beta_{CH}$, and ν_{CC} of *trans*-4,4'-dimercaptoazobenzene (*trans*-DMAB), respectively. This result suggests the oxidation of 4-ATP to *trans*-DMAB by O_2 from air. At t = 120 min, the spectrum remained essentially the same except for a slight increase in intensity for the peaks. Taken together, we believe that the Au islands could serve as a catalyst to facilitate the reduction of 4-NTP by $NaBH_4$.[39] Once $NaBH_4$ was completely consumed in the

reaction solution, the Ag atoms in the outmost surface could activate O_2 in the aqueous solution for the oxidation of 4-ATP to *trans*-DMAB.[41]

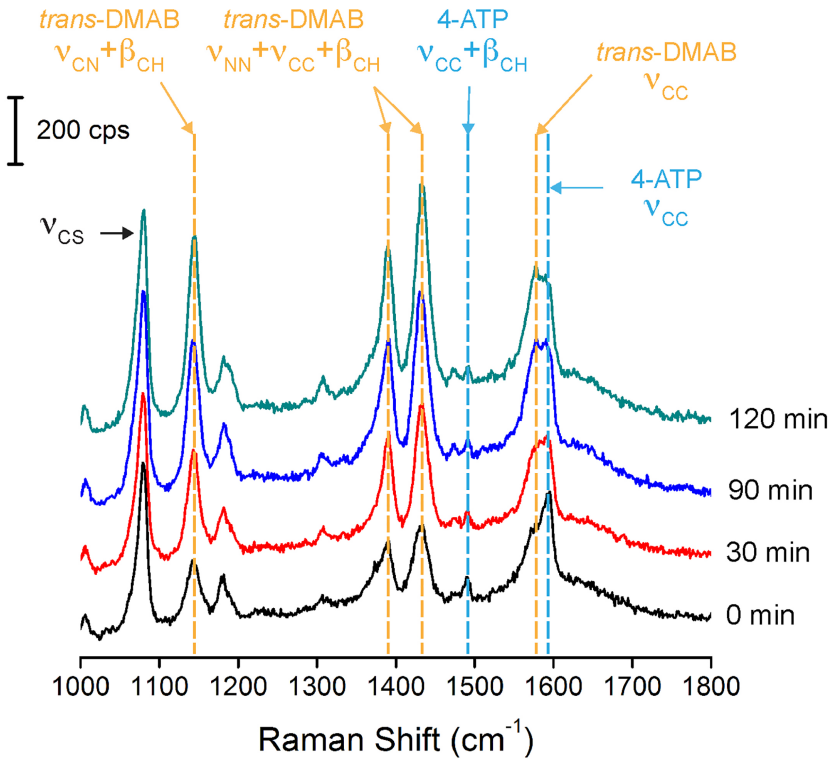

Figure 3.14. Time-dependent SERS spectra recorded before and after functionalizing the $Ag@SiO_2/Au$ nanoparticles with 4-ATP at an excitation wavelength of 532 nm. The nanoparticles were prepared with the titration of 0.4 mL of 0.1 mM $HAuCl_4$.

To gain a better mechanistic insight into the oxidation of 4-ATP to *trans*-DMAB on the surface of the $Ag@SiO_2/Au$ nanoparticles, we directly functionalized the surface of the nanoparticles (obtained at a titration volume of 0.4 mL) with 4-ATP and then recorded the SERS spectra. As shown in Figure 3.14 we also observed the four peaks of *trans*-

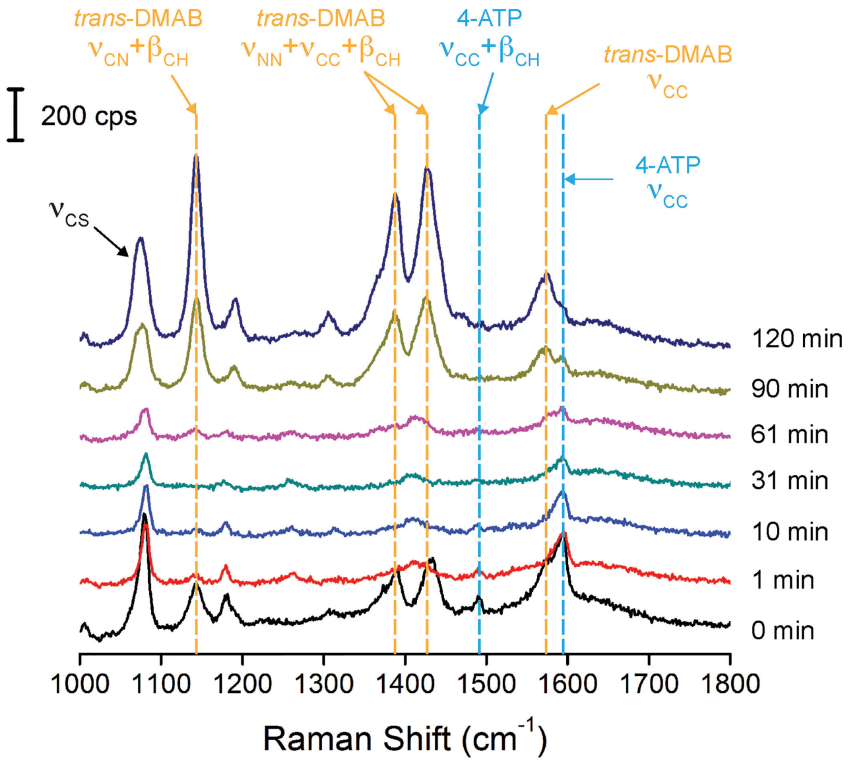

Figure 3.15. SERS spectra recorded before and after the introduction of $NaBH_4$ solution into an aqueous suspension of $Ag@SiO_2/Au$ nanoparticles functionalized with 4-ATP as a SERS probe molecule. The nanoparticles were prepared with the titration of 0.4 mL of 0.1 mM $HAuCl_4$ solution.

DMAB at 1142 cm^{-1}, 1390 cm^{-1}, 1430 cm^{-1}, and 1576 cm^{-1}, together with two peaks of 4-ATP peaks at 1595 and 1489 cm^{-1}, suggesting that some of the immobilized 4-ATP could be oxidized by the O_2 from air to generate *trans*-DMAB. This observation is consistent with previous findings.[42,43] When the solution was left in the air for up to 120 min, the intensities of peaks from *trans*-DMAB were found to continuously increase with no change in the peak positions. Interestingly, we can reduce the *trans*-DMAB back to 4-ATP by adding $NaBH_4$. As shown in Figure 3.15, upon the introduction of $NaBH_4$, the four characteristic peaks of *trans*-DMAM (marked in yellow) disappeared after 1 min. The

remaining two peaks can be assigned to 4-ATP (marked in green). From 1 to 60 min, the SERS spectra showed very minor changes except that the two peaks of 4-ATP dropped in intensity, likely due to the desorption of 4-ATP caused by $NaBH_4$ as we discussed previously.[38] At t = 90 min, the peaks of *trans*-DMAB returned. At this point, all the $NaBH_4$ had been consumed and 4-ATP was oxidized back to *trans*-DMAB by the O_2 from air. At t = 120 min, the peak positions remained the same but the intensities of all bands dropped, which is consistent with our previous observation (see Figure 3.13).

3.4 Conclusions

In summary, we have demonstrated a rational approach to synthesize $Ag@SiO_2/Au$ nanoparticles through the titration of $HAuCl_4$ into an aqueous suspension of $Ag@SiO_2$ core-shell nanocubes in the presence of H_2Asc, PVP, and NaOH at pH = 11.9. Both HAADF-STEM and EELS studies confirm the growth of Au islands (with sizes in the range of 6 to 12 nm) directly from the surface of each Ag nanocube, passing through the SiO_2 shell to generate an "islands in the sea" structure. In this synthesis, NaOH plays a critical role in creating some initial pores in the SiO_2 shell on each Ag nanocube. The salt precursor reacts with Ag through galvanic replacement to initiate the nucleation of Au, followed by continuous reduction by H_2Asc and Ag for epitaxial growth into discrete Au islands that eventually pass through and protrude from the SiO_2 shell. The SiO_2 surrounding the Au islands help confine them to a small size while preventing them from coalesce into larger structures. The Au islands embrace strong catalytic activity toward the reduction of 4-NP by $NaBH_4$. Because the Au islands are directly attached to the surface of the Ag nanocube, the $Ag@SiO_2/Au$ nanoparticles also exhibit strong SERS activity comparable to that of the pristine Ag nanocubes. By integrating the catalytic and SERS

activities originating from the Au islands and Ag cores, respectively, we demonstrated the fabrication of a bifunctional probe for *in situ* monitoring the Au-catalyzed reduction of 4-NTP by $NaBH_4$ and subsequently the Ag-catalyzed oxidation of 4-ATP by the O_2 from air. The strategy demonstrated in this work can be potentially extended to other noble metals other than Au to fabricate hybrid nanocrystals for other catalytic reactions.

3.5 Notes to Chapter 3

Part of this chapter is adapted from the paper "Bifunctional $Ag@SiO_2$/Au Nanoparticles for Probing Sequential Catalytic Reactions by Surface-Enhanced Raman Spectroscopy" published in *ChemNanoMat*.

3.6 References

[1] El-Sayed, M. A., Some Interesting Properties of Metals Confined in Time and Nanometer Space of Different Shapes. *Acc. Chem. Res.* **2001**, *34*, 257-264.

[2] Jones, M. R.; Osberg, K. D.; Macfarlane, R. J.; Langille, M. R.; Mirkin, C. A., Templated Techniques for the Synthesis and Assembly of Plasmonic Nanostructures. *Chem. Rev.* **2011**, *111*, 3736-3827.

[3] Haes, A. J.; Haynes, C. L.; McFarland, A. D.; Schatz, G. C.; Van Duyne, R. P.; Zou, S., Plasmonic Materials for Surface-Enhanced Sensing and Spectroscopy. *MRS Bull.* **2005**, *30*, 368-375.

[4] Lal, S.; Clare, S. E.; Halas, N. J., Nanoshell-Enabled Photothermal Cancer Therapy: Impending Clinical Impact. *Acc. Chem. Res.* **2008**, *41*, 1842-1851.

[5] Xia, Y.; Li, W.; Cobley, C. M.; Chen, J.; Xia, X.; Zhang, Q.; Yang, M.; Cho, E. C.; Brown, P. K., Gold Nanocages: from Synthesis to Theranostic Applications. *Acc. Chem. Res.* **2011**, *44*, 914-924.

[6] Gilroy, K. D.; Ruditskiy, A.; Peng, H.-C.; Qin, D.; Xia, Y., Bimetallic Nanocrystals: Syntheses, Properties, and Applications. *Chem. Rev.* **2016**, *116*, 10414-10472.

[7] Zhang, H.; Jin, M.; Xia, Y., Enhancing the Catalytic and Electrocatalytic Properties of Pt-Based Catalysts by Forming Bimetallic Nanocrystals with Pd. *Chem. Soc. Rev.* **2012**, *41*, 8035-8049.

[8] Wang, D.; Li, Y., Bimetallic Nanocrystals: Liquid-Phase Synthesis and Catalytic Applications. *Adv. Mater.* **2011**, *23*, 1044-1060.

[9] DeSantis, C. J.; Weiner, R. G.; Radmilovic, A.; Bower, M. M.; Skrabalak, S. E., Seeding Bimetallic Nanostructures as a New Class of Plasmonic Colloids. *J. Phys. Chem. Let.* **2013**, *4*, 3072-3082.

[10] Peng, Z.; Yang, H., Designer Platinum Nanoparticles: Control of Shape, Composition in Alloy, Nanostructure and Electrocatalytic Property. *Nano Today* **2009**, *4*, 143-164.

[11] Zhang, Q.; Li, W.; Moran, C.; Zeng, J.; Chen, J.; Wen, L.-P.; Xia, Y., Seed-Mediated Synthesis of Ag Nanocubes with Controllable Edge Lengths in the Range of 30-200 nm and Comparison of Their Optical Properties. *J. Am. Chem. Soc.* **2010**, *132*, 11372-11378.

[12] Michaels, A. M.; Nirmal, M.; Brus, L., Surface Enhanced Raman Spectroscopy of Individual Rhodamine 6G Molecules on Large Ag Nanocrystals. *J. Am. Chem. Soc.* **1999**, *121*, 9932-9939.

[13] Christopher, P.; Linic, S., Engineering Selectivity in Heterogeneous Catalysis: Ag Nanowires as Selective Ethylene Epoxidation Catalysts. *J. Am. Chem. Soc.* **2008**, *130*, 11264-11265.

[14] Hammer, B.; Norskov, J., Why Gold is the Noblest of All the Metals. *Nature* **1995**, *376*, 238-240.

[15] Haruta, M., Size- and Support-Dependency in the Catalysis of Gold. *Catal. Today* **1997**, *36*, 153-166.

[16] Overbury, S.; Schwartz, V.; Mullins, D. R.; Yan, W.; Dai, S., Evaluation of the Au Size Effect: CO Oxidation Catalyzed by Au/TiO_2. *J. Catal.* **2006**, *241*, 56-65.

[17] Janssens, T. V.; Carlsson, A.; Puig-Molina, A.; Clausen, B. S., Relation between Nanoscale Au Particle Structure and Activity for CO Oxidation on Supported Gold Catalysts. *J. Catal.* **2006**, *240*, 108-113.

[18] Xia, X.; Wang, Y.; Ruditskiy, A.; Xia, Y., 25th Anniversary Article: Galvanic Replacement: A Simple and Versatile Route to Hollow Nanostructures with Tunable and Well-Controlled Properties. *Adv. Mater.* **2013**, *25*, 6313-6333.

[19] Yang, Y.; Liu, J.; Fu, Z.-W.; Qin, D., Galvanic Replacement-Free Deposition of Au on Ag for Core-Shell Nanocubes with Enhanced Chemical Stability and SERS Activity. *J. Am. Chem. Soc.* **2014**, *136*, 8153-8156.

[20] Lee, J.; Park, J. C.; Song, H., A Nanoreactor Framework of a Au@SiO_2 Yolk/Shell Structure for Catalytic Reduction of *p*-Nitrophenol. *Adv. Mater.* **2008**, *20*, 1523-1528.

[21] Yu, K.; Wu, Z.; Zhao, Q.; Li, B.; Xie, Y., High-Temperature-Stable Au@SnO_2 Core/Shell Supported Catalyst for CO Oxidation. *J. Phys. Chem. C*. **2008**, *112*, 2244-2247.

[22] Arnal, P. M.; Comotti, M.; Schüth, F., High-Temperature-Stable Catalysts by Hollow Sphere Encapsulation. *Angew. Chem., Int. Ed.* **2006**, *118*, 8404-8407.

[23] Dai, Y.; Lim, B.; Yang, Y.; Cobley, C. M.; Li, W.; Cho, E. C.; Grayson, B.; Fanson, P. T.; Campbell, C. T.; Sun, Y.; Xia, Y., A Sinter-Resistant Catalytic System Based on Platinum Nanoparticles Supported on TiO_2 Nanofibers and Covered by Porous Silica. *Angew. Chem., Int. Ed.* **2010**, *122*, 8341-8344.

[24] Ge, J.; Zhang, Q.; Zhang, T.; Yin, Y., Core-Satellite Nanocomposite Catalysts Protected by a Porous Silica Shell: Controllable Reactivity, High Stability, and Magnetic Recyclability. *Angew. Chem., Int. Ed.* **2008**, *120*, 9056-9060.

[25] Lu, P.; Campbell, C. T.; Xia, Y., A Sinter-Resistant Catalytic System Fabricated by Maneuvering the Selectivity of SiO_2 Deposition onto the TiO_2 Surface versus the Pt Nanoparticle Surface. *Nano Lett.* **2013**, *13*, 4957-4962.

[26] Stöber, W.; Fink, A.; Bohn, E., Controlled Growth of Monodisperse Silica Spheres in the Micron Size Range. *J. Colloid Interface Sci.* **1968**, *26*, 62-69.

[27] Zhang, Q.; Zhang, T.; Ge, J.; Yin, Y., Permeable Silica Shell through Surface-Protected Etching. *Nano Lett.* **2008**, *8*, 2867-2871.

[28] Au, L.; Lu, X.; Xia, Y., A Comparative Study of Galvanic Replacement Reactions Involving Ag Nanocubes and $AuCl_2^-$ or $AuCl_4^-$. *Adv. Mater.* **2008**, *20*, 2517-2522.

[29] Zhang, Q.; Li, W.; Wen, L. P.; Chen, J.; Xia, Y., Facile Synthesis of Ag Nanocubes of 30 to 70 nm in Edge Length with CF_3COOAg as a Precursor. *Chem. - Eur. J.* **2010**, *16*, 10234-10239.

[30] Liz-Marzán, L. M.; Giersig, M.; Mulvaney, P., Synthesis of Nanosized Gold-Silica Core-Shell Particles. *Langmuir* **1996**, *12*, 4329-4335.

[31] Sun, X.; Kim, J.; Gilroy, K. D.; Liu, J.; König, T. A.; Qin, D., Gold-Based Cubic Nanoboxes with Well-Defined Openings at the Corners and Ultrathin Walls Less Than Two Nanometers Thick. *ACS Nano*, **2016**, *10*, 8019-8025.

[32] Moulder, J. F.; Stickle, W. F.; Sobol, P. E.; Bomben, K. D., *Handbook of X-ray Photoelectron Spectroscopy*. Perkin-Elmer Corporation: **1992**.

[33] Haldar, K. K.; Kundu, S.; Patra, A., Core-Size-Dependent Catalytic Properties of Bimetallic Au/Ag Core-Shell Nanoparticles. *ACS Appl. Mater. Interfaces* **2014**, *6*, 21946-21953.

[34] Zhou, F.; Li, Z.-Y.; Liu, Y.; Xia, Y., Quantitative Analysis of Dipole and Quadrupole Excitation in the Surface Plasmon Resonance of Metal Nanoparticles. *J. Phys. Chem. C*, **2008**, *112*, 20233-20240.

[35] Schatz, G. C., Theoretical Studies of Surface Enhanced Raman Scattering. *Acc. Chem. Res.* **1984**, *17*, 370-376.

[36] Camden, J. P.; Dieringer, J. A.; Wang, Y.; Masiello, D. J.; Marks, L. D.; Schatz, G. C.; Van Duyne, R. P., Probing the Structure of Single-Molecule Surface-Enhanced Raman Scattering Hot Spots. *J. Am. Chem. Soc.* **2008**, *130*, 12616-12617.

[37] Etchegoin, P. G.; Le Ru, E., A Perspective on Single Molecule SERS: Current Status and Future Challenges. *Phys. Chem. Chem. Phys.* **2008**, *10*, 6079-6089.

[38] Ansar, S. M.; Ameer, F. S.; Hu, W.; Zou, S.; Pittman Jr, C. U.; Zhang, D., Removal of Molecular Adsorbates on Gold Nanoparticles Using Sodium Borohydride in Water. *Nano Lett.* **2013**, *13*, 1226-1229.

[39] Zhang, J.; Winget, S. A.; Wu, Y.; Su, D.; Sun, X.; Xie, Z.-X.; Qin, D., Ag@Au Concave Cuboctahedra: A Unique Probe for Monitoring Au-Catalyzed Reduction and Oxidation Reactions by Surface-Enhanced Raman Spectroscopy. *ACS Nano* **2016**, *10*, 2607-2616.

[40] Li, J.; Liu, J.; Yang, Y.; Qin, D., Bifunctional Ag@Pd-Ag Nanocubes for Highly Sensitive Monitoring of Catalytic Reactions by Surface-Enhanced Raman Spectroscopy. *J. Am. Chem. Soc.* **2015**, *137*, 7039-7042.

[41] Li, J.; Wu, Y.; Sun, X.; Liu, J.; Winget, S. A.; Qin, D., A Dual Catalyst with SERS Activity for Probing Stepwise Reduction and Oxidation Reactions. *ChemNanoMat* **2016**, *2*, 786-790.

[42] Huang, Y.-F.; Zhu, H.-P.; Liu, G.-K.; Wu, D.-Y.; Ren, B.; Tian, Z.-Q., When the Signal Is not from the Original Molecule to Be Detected: Chemical Transformation of *para*-Aminothiophenol on Ag during the SERS Measurement. *J. Am. Chem. Soc.* **2010**, *132*, 9244-9246.

[43] Huang, Y.-F.; Wu, D.-Y.; Zhu, H.-P.; Zhao, L.-B.; Liu, G.-K.; Ren, B.; Tian, Z.-Q., Surface-Enhanced Raman Spectroscopic Study of *p*-Aminothiophenol. *Phys. Chem. Chem. Phys.* **2012**, *14*, 8485-8497.

CHAPTER 4. IN SITU ATOMIC-LEVEL TRACKING OF HETEROGENEOUS NUCLEATION IN NANOCRYSTAL GROWTH WITH AN ISOCYANIDE MOLECULE

4.1 Introduction

Building upon the prior success, here we turn the synthesis of core-frame nanocubes into a model system for investigating the fundamentals involved in the heterogeneous nucleation and overgrowth of metal nanocrystals. Although site-selective deposition has been successfully demonstrated for a set of bimetallic systems, including Pd-Rh, Pd-Pt, Pd-Ru, Ag-Au, and Ag-Pd (with the former being the seed and the latter the metal deposited),[1-7] it has been extremely challenging to resolve the second metal deposited on the surface of a nanocrystal, in particular, when the deposited amount is below one monolayer. Two different approaches are commonly used in the literature. The first is based upon elemental mapping using energy-dispersive X-ray spectroscopy (EDX) or electron energy loss spectroscopy (EELS) and the second involves selective etching of the original seed, followed by electron microscopy (EM) characterization of the remaining structure.[6-12] Both EDX and EELS are well known for their superb spatial resolutions but it is nontrivial to obtain reliable data when the deposited metal is below one monolayer.[13] These techniques also require the use of advanced EM facilities and cannot be used to directly analyze a sample without drying and additional processing. The second approach, on the other hand, only works if the amount of the deposited metal is sufficient for the generation of a robust, free-standing hollow structure. During sample preparation, the adatoms can move around by diffusion, causing alternations to the original structure.

We propose to address the challenge by taking a paradigm shift through the development of metal-sensitive SERS probes for better understanding the heterogeneous nucleation and early-stage deposition of metal atoms (M) on the edges of Ag nanocubes. Our central hypothesis is that the vibrational frequency of a metal-sensitive SERS probe can serve as a distinctive reporter for the metal being deposited on the surface of a Ag nanocrystal, with a detection limit well below one monolayer. More significantly, such an analysis can be conducted while the particles are still suspended in the original reaction solution for *in situ* characterization of the heterogeneous nucleation and early-stage deposition. I will validate this hypothesis by focusing on a well-defined model system based upon Ag nanocubes with slight truncation at the corners and edges. According to the simulation results obtained using the discrete dipole approximation (DDA) method, intensified electric fields will be created on the edges of a Ag nanocube upon excitation of LSPR, generating hot spots for ultrasensitive detection by SERS (Figure 4.1A).[13] Remarkably, these hot spots coincide with the sites preferred for the heterogeneous nucleation and deposition of the second metal during seeded overgrowth because of their high surface free energies. As a result, it is feasible to elucidate the fundamental details by introducing a metal-sensitive SERS probe capable of differentiating the deposited M atoms from the original Ag atoms.

Conventionally, thiol-based molecules have been most commonly used as SERS probes, with notable examples including 1,4-benzenedithiol and 4-nitrothiophenol. Although the vibrational modes associated with their benzene rings are strong enough to allow for ultrasensitive detection of these molecules upon adsorption onto the surface of Ag or Au nanocrystals,[14-17] these vibrational modes show essentially no dependence on the

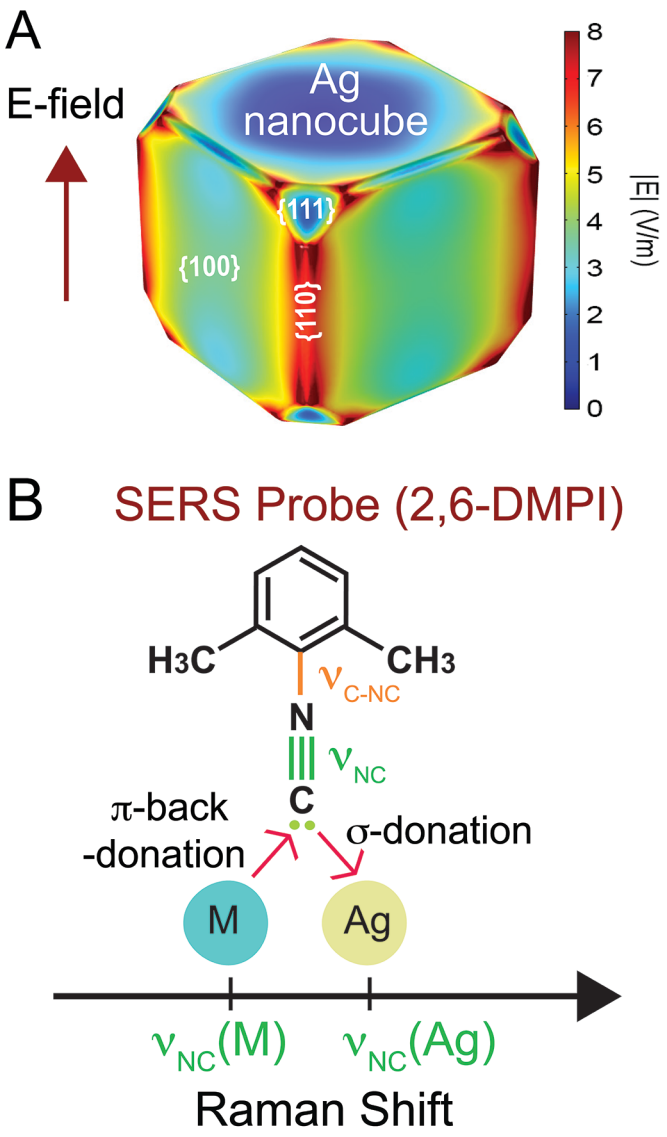

Figure 4.1. (A) Plot of electric field on the surface of a Ag nanocube with edge length of 39 nm at the laser excitation of 532 nm. (B) Schematic illustration showing the difference in the electron donation and corresponding stretching frequency change when the isocyanide group binds to Ag and M atoms.

metal surface, making them invalid for the identification of different metals. Recent studies suggest that, isocyanide compounds could serve as metal-sensitive SERS probes because the binding of the isocyanide group (–NC) to a transition metal is similar to that of carbon

monoxide (CO) due to their isoelectronic structure.[18, 19] To this end, a number of research groups reported distinctive stretching frequencies (ν_{NC}) for the NC bond when the –NC group binds to different types of metals in the context of nanoparticles, powders, and crystal substrates. For example, Shin *et al.* reported that the ν_{NC} band was positioned at 2175 and 2107 cm^{-1}, respectively, when 2,6-dimethylphenyl isocyanide (2,6-DMPI) was introduced as a SERS probe to coordinate with the Ag and Pd (on Ag-Pd alloy nanoparticles) atoms.[20] Sanchez-Cortes *et al.* studied the adsorption of 1,4-phenylene diisocyanide (1,4-PDI) on Ag and Au nanoparticles and they argued that the two different SERS peaks located at 2182 and 2125 cm^{-1} could be assigned to bounded and unbounded –NC groups on Ag, respectively.[21] Zou *et al.* reported the SERS study of 1,4-PDI adsorbed on Au, Pt, Rh, and Pd electrodes.[22] They revealed that the frequency of ν_{NC} was strongly dependent on the metal to which the isocyanide group bound. Ikeda *et al.* investigated the adsorption of 4-chlorophenyl isocyanide (4-CPI) on a single-crystal Pt surface using gap-mode SERS.[23] They also observed the formation of Pd islands on the surface of a Au(111) substrate by employing 4-CPI as a SERS probe.[24] Taken together, it has been well-established that the lone-pair electrons associated with the carbon atom in the –NC group could bind to the surface of Ag or Au via σ donation and to that of Pt or Pd via π-back donation, leading to blue and red shifts, respectively, for ν_{NC}.

As the first demonstration, we discovered that the isocyanide-based SERS probe could serve as a distinctive reporter for investigation of the heterogeneous nucleation and early stage deposition of the transition metal such as Pt on the plasmonically active Ag or Au nanocrystals by monitoring the change to the frequency of ν_{NC} with *in situ* SERS (Figure 4.1B). As the first proof-of-concept demonstration, we reported the use of 2,6-

DMPI as a SERS probe for watching the overgrowth of Pt on Ag nanocubes in the original growth solution.[13] By monitoring the stretching frequencies and the peak intensities of ν_{NC} in real time, we demonstrated that *in situ* SERS had the sensitivity to detect as few as 27 Pt atoms being deposited onto each edge of a 39-nm Ag nanocube. Despite the remarkable detection sensitivity, we only observed one peak for ν_{NC} when 2,6-DMPI bound to Pt atoms in the atop configuration, making it impossible to further characterize the atomic arrangement of Pt atoms during the heterogeneous nucleation and early-stage deposition events.

According to the literature, the binding of CO to Pd atoms could take the atop, bridge, and hollow configurations.[25-27] As such, we propose that 2,6-DMPI can bind to Pd atoms in these three different configurations, making it feasible to characterize the arrangement of Pd atoms being deposited onto different types of facets of Ag nanocubes by monitoring the vibrational frequency of ν_{NC} (Figure 4.2). Specifically, the 2,6-DMPI probe should bind to Ag and Pd *via* σ donation and π-back donation, respectively, resulting in a blue shift for $\nu_{NC(Ag)\text{-}atop}$ and a red shift for $\nu_{NC(Pd)\text{-}atop}$ accordingly.[20] Similar to the case of CO, we believe that –NC can also bind to one, two, and three adjacent Pd atoms for the generation of atop, bridge, and hollow configurations, respectively.[27] Because the bond between the N and C atoms will be gradually weakened as –NC shares electrons with one, two, and three Pd atoms, the vibrational frequencies of $\nu_{NC(Pd)\text{-}atop}$, $\nu_{NC(Pd)\text{-}bridge}$, and $\nu_{NC(Pd)\text{-}hollow}$ should be further shifted to the red.

In this chapter, we report *in situ* atomic-level tracking of the heterogeneous nucleation of Pd on Ag nanocubes by using the 2,6-DMPI as a sensitive molecular probe.

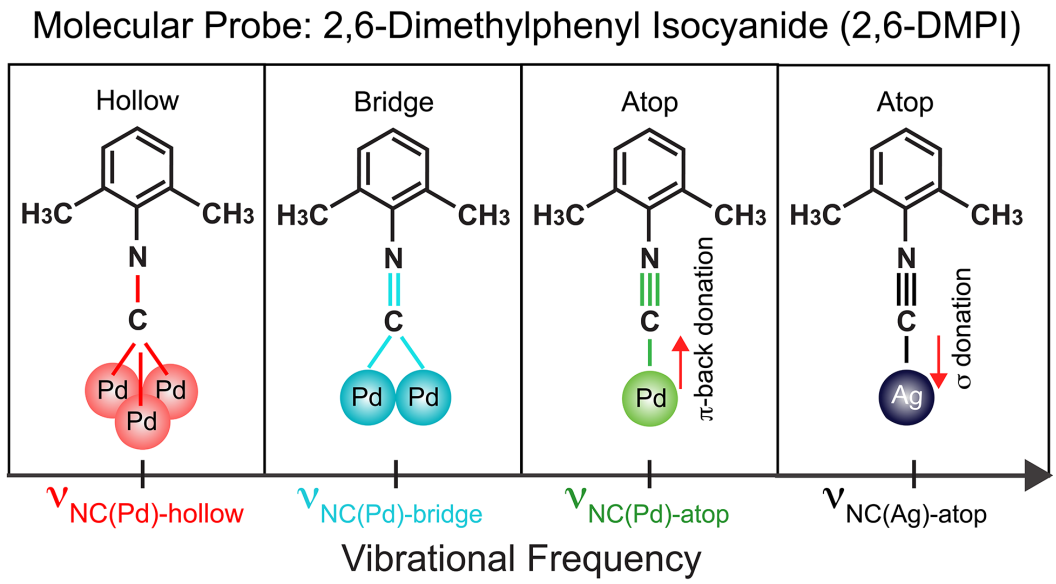

Figure 4.2. Schematic illustration showing the difference in stretching frequency for the NC bond, ν_{NC}, when 2,6-DMPI binds to Ag in the atop configuration and to the Pd atoms in the atop, bridge, and hollow configurations, respectively.

We demonstrate that the ν_{NC} band of 2,6-DMPI can serve as a distinctive reporter for the Pd adatoms being deposited on the surface of Ag nanocubes with atomic-level sensitivity. In the case of *ex situ* measurement, we follow a standard protocol to synthesize Ag-Pd nanocubes by adding Na_2PdCl_4 into the aqueous suspension of Ag nanocubes in the presence of ascorbic acid (H_2Asc, a reducing agent) and poly(vinyl pyrrolidone) (PVP, a colloidal stabilizer) under ambient condition. After collecting the solid products, we functionalize the nanoparticles with 2,6-DMPI molecules for *ex situ* SERS characterization. We are able to detect the $\nu_{NC(Pd)\text{-}atop}$, $\nu_{NC(Pd)\text{-}bridge}$, and $\nu_{NC(Pd)\text{-}hollow}$ bands in the SERS spectra, confirming that 2,6-DMPI can indeed serve as a probe to distinguish the Pd adatoms in terms of arrangement. Because the *ex situ* method often requires centrifugation and washing, during which the Pd adatoms can migrate from the original

sites of deposition prior to SERS measurements, we also develop an *in situ* approach. In this case, we directly introduce 2,6-DMPI into the standard reaction solution and then sample aliquots at different time points for SERS measurement. We confirm that the presence of 2,6-DMPI in the reaction solution does not alter the reduction of the precursor, neither the deposition pathway of Pd on Ag nanocubes. We further demonstrate the capability of this *in situ* method for atomic-level tracking of Pd atoms being deposited on the Ag nanocubes by following the ν_{NC} bands for both Ag and Pd atoms as a function of reaction time. The different binding configurations of –NC to Pd atoms also offer an opportunity to investigate the roles played by reaction temperature and the type of Pd(II) precursor in affecting the reduction, deposition, and surface diffusion involved in heterogeneous nucleation.

4.2 Experimental Section

Chemicals and Materials. Poly(vinyl pyrrolidone) (PVP) with an average molecular weight of 29000 (PVP-29K) or 55000 (PVP-55K), L-ascorbic acid (H_2Asc, ≥98%), 2,6-dimethylphenyl isocyanide, (2,6-DMPI, ≥98%), ethanol (CH_3CH_2OH, 200 proof), sodium tetrachloropalladate(II) (Na_2PdCl_4, ≥99.99% trace metal basis), silver trifluoroacetate (CF_3COOAg, ≥99.99% trace metal basis), sodium hydrosulfide hydrate ($NaHS{\cdot}xH_2O$), aqueous hydrochloric acid (HCl, 37%), hydrogen peroxide (H_2O_2, 30 wt.% in H_2O), iron(III) nitrate nonahydrate ($Fe(NO_3)_3{\cdot}9H_2O$, ≥98%) and nitric acid (HNO_3, 70%) were all purchased from Sigma-Aldrich. Ethylene glycol ($HOCH_2CH_2OH$, EG) was ordered from J.T. Baker. Acetone (C_3H_6O, HPLC grade, 99.5+%) and sodium tetrabromopalladate(II) (Na_2PdBr_4, 99.95% trace metal basis, Pd 22.0% min) were

obtained from Alfa Aesar. All the chemicals were used as received. The deionized (DI) water had a resistivity of 18.2 MΩ·cm at room temperature.

Synthesis of Silver Nanocubes. We followed a published protocol to synthesize the Ag nanocubes.[28] The products were washed with acetone and DI water three times and then dispersed in DI water for further use. The suspension of Ag nanocubes had a final concentration of 6.56×10^{12} particles/mL.

Synthesis of Ag-Pd Nanocubes. In a typical synthesis, 2 mL of 1 mM PVP-29K aqueous solution was placed in a 23-mL vial, followed by the introduction of 0.5 mL of 100 mM aqueous H_2Asc, 0.5 mL of DI water, and 25 μL of the aqueous suspension of Ag nanocubes (1.64×10^{11} particles) at room temperature under magnetic stirring. Different volumes of aqueous Na_2PdCl_4 (0.2 mM) were then injected into the vial using a pipette. After 20 min, the solid products were collected by centrifugation at 6000 rpm for 10 min and re-dispersed in DI water for further use.

Raman Measurements. The Raman spectra were recorded using a Renishaw inVia Raman Spectrometer integrated with a Leica microscope. The excitation wavelength was 532 nm and the scattered light was dispersed using a holographic notch filter with a grating of 2400 lines/mm. For all the time-dependent SERS spectra, they were collected using either *static* or *extended* mode. In the *static* mode, we recorded a Raman spectrum in the range of 1445.83–2495.29 cm^{-1} by setting the center position at 2000 cm^{-1} almost instantaneously, within a period as short as 1 s. We typically used a collection time of 10 s to improve the signal-to-noise ratio by averaging multiple spectra. In the *extended* mode,

it took about 90 s for the spectrometer to scan across the spectral region from 500 cm^{-1} to 2500 cm^{-1} when a collection time of 10 s was used.

***Ex Situ* SERS Measurements.** The as-prepared particles were dispersed in 1 mL of ethanol containing 0.01 mM 2,6-DMPI and incubated at room temperature for 60 min. Next, the 2,6-DMPI-functionalized nanocubes were collected by centrifugation and washed with DI water twice and re-dispersed in 200 μL of DI water, with a final concentration of 1.3×10^{10} particles/mL. We fabricated the sample cell by punching a hole, which could hold 25 μL of liquid, on the surface of a polydimethylsiloxane (PDMS) block and then having it mounted on a piece of glass slide. Upon the introduction of liquid sample, the cell was carefully covered with a glass coverslip of 0.17 mm in thickness to avoid solvent evaporation. The top surface of the coverslip could also work as a reference point, from which the focal plane was defined at 200 μm into the sample. We collected the SERS spectra in the *extended* mode, with a 5x objective lens, a laser power of 50 mW, and a collection time of 10 s.

***In Situ* SERS Measurements in the Reaction Solution.** In a typical study, 2 mL of 1 mM PVP-29K aqueous solution was introduced into a 23-mL vial, followed by the addition of 0.5 mL of 100 mM aqueous H_2Asc and 0.5 mL of 0.01 mM 2,6-DMPI in ethanol at room temperature (21 °C) under magnetic stirring (650 rpm). For the temperature dependent experiments, the reaction container was immersed in an ice bath (0 °C) or oil bath (40 °C) for 30 min. Initially, an aliquot of 25 μL was withdrawn from the mixture and a solution-phase Raman spectrum was recorded before 25 μL of an aqueous suspension of Ag nanocubes (1.64×10^{11} particles in total) was added. After 10 min, an aliquot of 25 μL

was withdrawn from the reaction solution and a SERS spectrum was recorded. Finally, 50 μL of 0.2 mM aqueous Na_2PdCl_4 (or 50 μL of 0.2 mM aqueous Na_2PdBr_4) was introduced using a pipette. At different time points of reaction, an aliquot of 25 μL was quickly withdrawn from the reaction solution and its SERS spectrum was recorded in the *extended* mode, with a 5x objective lens, a laser power of 50 mW, and a collection time of 10 s. After 60 min, the remaining particles were collected by centrifugation and washed with DI water three times prior to TEM characterization.

We also recorded *in situ* SERS spectra of the reaction mixture in the *static* mode. In this case, an aliquot of 25 μL was withdrawn from the same reaction system at a specific time point and subjected to SERS measurement with a 5x objective lens, a laser power of 50 mW, and a collection time of 1 or 10 s.

Instrumentation and Characterization. We used a centrifuge (Eppendorf 5430) for the collection and washing of all solid products. A Cary 50 spectrometer (Agilent Technologies, Santa Clara, CA) was used to record the UV-vis spectra. The quantitative measurement of Ag and Pd contents was conducted using an inductively coupled plasma mass spectrometer (ICP-MS, NexION 300Q, PerkinElmer, Waltham, MA). Transmission electron microscopy (TEM) images were taken using a Hitachi HT7700 microscope (Hitachi, Japan) operated at 120 kV. The Raman and SERS spectra were recorded using a Renishaw inVia Raman Spectrometer (Wotton-under-Edge, UK) integrated with a Leica microscope (Wetzlar, Germany).

4.3 Results and Discussion

4.3.1 Analysis of the SERS Detection Mechanism

Figure 4.3 shows how SERS can be used for *in situ*, atomic-level tracking of the heterogeneous nucleation of Pd on a Ag nanocube with the aid of 2,6-DMPI. As reported in literature[29-32] and illustrated in Figure 4.3A, the Pd atoms should be preferentially deposited on the edges, terminated in {110} facets, of a Ag nanocube, followed by the diffusion of Pd adatoms to corners and side faces that correspond to {111} and {100} facets, respectively. Our calculations based on the finite element method (FEM) indicate that the SERS hot spots of a 39-nm Ag nanocube are predominantly located on the edges (see Figure 4.1A).[13] Our results suggest that the electromagnetic field can also be enhanced at sites in close proximity to the edges, including those regions on the corners and side faces. When 2,6-DMPI binds to the surface atoms on a Ag-Pd nanocube, Figure 4.3B illustrates two scenarios. In the first scenario (top panel), which corresponds to the early

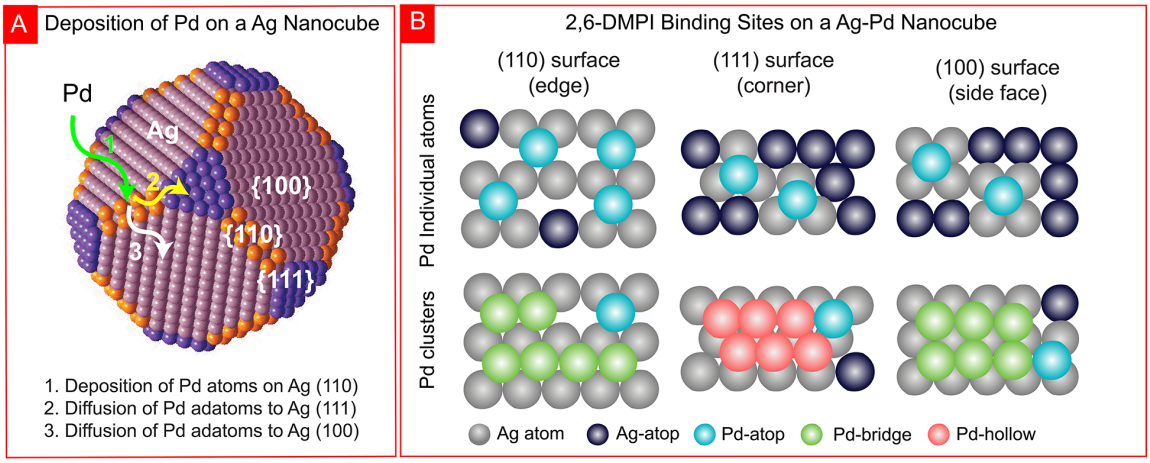

Figure 4.3. (A) Schematic diagram of a proposed pathway for the deposition of Pd atoms on a Ag nanocube. (B) Schematic illustrations showing the different binding sites and configurations for Pd atoms on the surface of a Ag nanocube.

stage of a synthesis, Pd is deposited as individual adatoms on the outermost surface of a Ag nanocube. As a result, 2,6-DMPI binds to both the Pd adatoms and the remaining Ag atoms in the atop configuration only. In the second scenario (bottom panel), as the deposition of Pd progresses toward a monolayer to generate Pd clusters on the Ag surface, 2,6-DMPI can bind to the Pd adatoms in the atop, bridge, and hollow configurations, respectively. According to the atomic arrangement, the Pd adatoms on the {111} facets (the corners) can give rise to atop and hollow configurations while the {110} facets (edges) and {100} facts (side faces) only allow for atop and bridge configurations. Taken together, we hypothesize that 2,6-DMPI can serve as a unique probe to characterize the arrangements of Pd adatoms being deposited onto different types of facets on Ag nanocubes by monitoring the peak intensities of the $\nu_{NC(Pd)\text{-atop}}$, $\nu_{NC(Pd)\text{-bridge}}$, $\nu_{NC(Pd)\text{-hollow}}$ bands.

4.3.2 Synthesis of Ag-Pd Nanocubes

After the preparation of Ag nanocubes with an average edge length of 40.3±1.6 nm (Figure 4.4A),[28] we dispersed them in an aqueous solution containing H_2Asc and PVP, followed by the injection of aqueous Na_2PdCl_4 under ambient condition. Figure 4.4B and C, shows TEM images of the as-obtained Ag-Pd nanocubes prepared with the introduction of 50 μL and 600 μL of Na_2PdCl_4 solution, respectively. In both cases, we noticed that the cubic shape of the nanocubes was well retained. To resolve the sites of deposition for Pd on the surface of Ag nanocubes, we used an aqueous mixture of $Fe(NO_3)_3$ and HNO_3 to remove the Ag core while retaining the Pd. We were unable to collect any solid by centrifugation for the sample prepared with 50 μL of aqueous Na_2PdCl_4. When the amount of Na_2PdCl_4 solution was increased to 600 μL, however, we obtained nanoframes, as

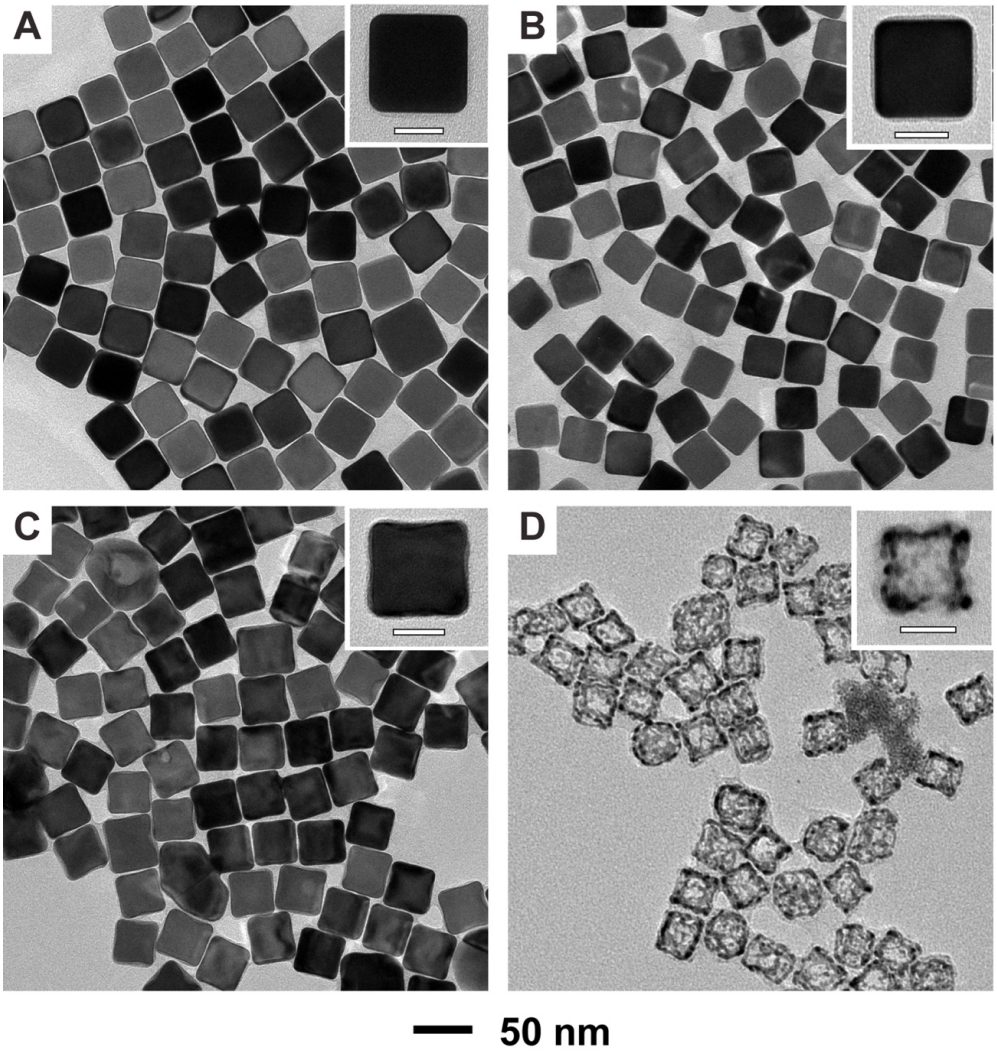

Figure 4.4. TEM images of (A) Ag nanocubes, (B, C) Ag-Pd nanocubes prepared by reacting 40-nm Ag nanocubes with 50 μL and 600 μL of aqueous Na_2PdCl_4, respectively, in the presence of H_2Asc and PVP, and (D) the resultant Ag-Pd nanoframes after the removal of Ag cores from the Ag-Pd nanocubes in (C) using an etchant based on $Fe(NO_3)_3/HNO_3$. The scale bar in the inset is 20 nm.

shown by the TEM image in Figure 4.4D. This result suggests that the Pd atoms derived from the reduction of Na_2PdCl_4 by H_2Asc were preferentially deposited on the edges of the

Ag nanocubes, together with the diffusion of some Pd adatoms to the corners and side faces. This result is consistent with the deposition mechanism proposed in Figure 4.3A.

To further confirm the deposition of Pd atoms on the Ag nanocubes, we used ICP-MS to measure Ag and Pd contents in both solid and supernatant before and after the Ag nanocubes had reacted with 50 μL of aqueous Na_2PdCl_4 in the presence of H_2Asc and PVP (Table 4.1). The ICP-MS data indicated that 46.6% of the added Na_2PdCl_4 was converted

Table 4.1. The contents of Pd and Ag in the solid product and supernatant using ICP-MS analysis. The sample was prepared by the injection volume of 50 μL Na_2PdCl_4 to the suspension of Ag nanocubes in the presence of H_2Asc and PVP.

Samples	Measured conc. of Ag (μg/L)	Measured conc. of Pd (μg/L)	Conversion rate of Pd (%)[a]
Ag nanocubes	4.6×10^6		
Na_2PdCl_4 solution (0.2 mM)		1.5×10^4	
Ag-Pd nanocubes			
Added Na_2PdCl_4		245.9	
Solid sample		114.5	46.6%
Supernatant		137.0	

[a]The conversion rate of Pd (%) was calculated from the mass ratio of Pd in the solid sample to the Pd in added Na_2PdCl_4.

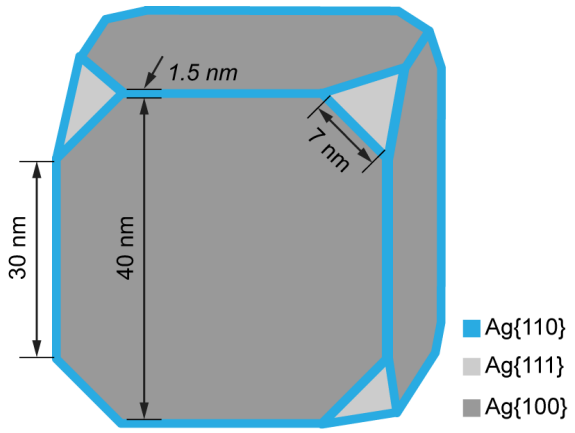

Figure 4.5. The graphic illustration of a Ag nanocube with all the dimensions labeled.

to Pd atoms, followed by their deposition onto the Ag nanocubes. If we assumed that these Pd atoms were deposited uniformly on all the edges of the Ag nanocubes with the dimensions defined in Figure 4.5, we estimated that 1006 Pd atoms would be deposited on each edge. The same back-of-the-envelope calculation suggested that 1189 Pd atoms would be needed for generating one monolayer of Pd adatoms on each edge of a nanocube (see details in 4.6 Appendix). On the basis of these results, we decided to focus on the two systems involving 10 and 50 μL of Na_2PdCl_4 solution when designing experiments to monitor the heterogeneous nucleation and deposition of Pd on the Ag nanocubes by SERS. It is worth mentioning that the added Na_2PdCl_4 could be reduced by both H_2Asc *via* chemical reduction and Ag *via* galvanic replacement. Because the morphology of the Ag-Pd nanocubes obtained using 50 μL of Na_2PdCl_4 solution was similar to that of the original Ag nanocubes (see Figure 4.4B), we argue that the reduction of Na_2PdCl_4 should be dominated by H_2Asc rather than by Ag. Otherwise, we expect to observe changes to the morphology.

4.3.3 Resolving the Arrangement of Pd Adatoms on Ag Nanocubes by Ex Situ SERS

In a typical process, we incubated the as-prepared Ag-Pd nanocubes in an ethanol solution of 0.01 mM 2,6-DMPI for 60 min, followed by the collection of solids through centrifugation. After the particles had been washed with DI water twice, they were re-dispersed in DI water for SERS measurements. Figure 4.6 shows the SERS spectra of 2,6-DMPI adsorbed on the Ag-Pd nanocubes prepared with 10 and 50 μL of Na_2PdCl_4 solution.

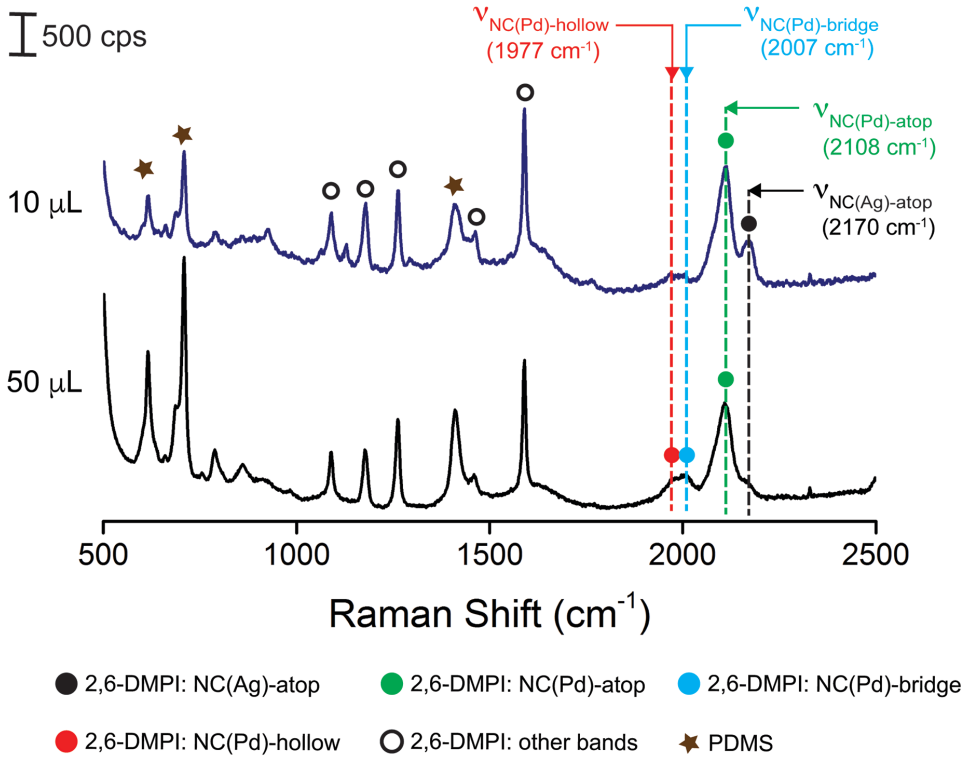

Figure 4.6. *Ex situ* SERS spectra recorded from aqueous suspensions of 2,6-DMPI-functionalized samples prepared by reacting 40-nm Ag nanocubes with 10 μL and 50 μL, respectively, of Na_2PdCl_4 in the presence of H_2Asc and PVP at room temperature.

For the case of 10 μL, the SERS spectrum showed two major peaks at 2170 and 2108 cm-[1], with their assignment to the NC stretching of the probe molecules binding to Ag ($\nu_{NC(Ag)\text{-}atop}$) and Pd ($\nu_{NC(Pd)\text{-}atop}$), respectively.[20] When compared with the ν_{NC} band at 2123 cm^{-1} for the ordinary Raman spectrum of 2,6-DMPI in the neat state (Figure 4.7), we noticed that the $\nu_{NC(Ag)\text{-}atop}$ and $\nu_{NC(Pd)\text{-}atop}$ bands were blue- and red-shifted, respectively. The ratio between the peak intensities of the $\nu_{NC(Pd)\text{-}atop}$ and $\nu_{NC(Ag)\text{-}atop}$ bands was 2.79:1. The other well-resolved peaks were associated with different vibrational modes of the benzene ring in 2,6-DMPI (see Table 4.2 for peak assignments).[20] We also observed some peaks belonging to PDMS (marked by solid stars, see Figure 4.8 for an ordinary Raman spectrum

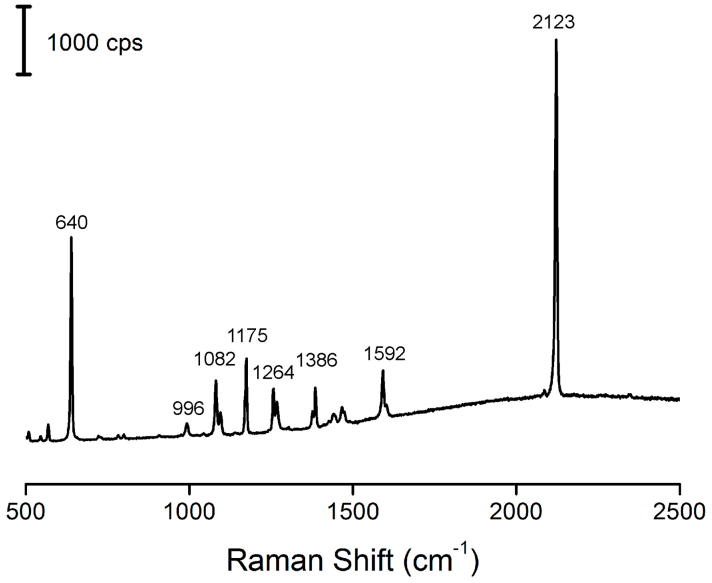

Figure 4.7. The ordinary Raman spectrum of 2,6-DMPI in its neat state on a Si substrate.

Table 4.2. The SERS and ordinary Raman shifts of 2,6-DMPI and their assignments.

SERS (cm^{-1})	Ordinary (cm^{-1})	Assignment[a]
	640	$\nu_{C\text{-}NC}$
	996	12 (A_1)
1088	1082	13 (A_1)
1176	1175	9b (B_2)
1264	1264	3 (B_2) γ_{CH2}
	1386	19b (B_2)
1590	1592	8a (A_1)
2162 (Ag-atop)		
2104 (Pd-atop)	2123	ν_{NC}
2007 (Pd-bridge)		
1973 (Pd-hollow)		

[a] Ref. 34.

of PDMS and Table 4.3 for their peak assignments).[33] Taken together, we hypothesized that the Pd was deposited on the edges of the Ag nanocubes as individual atoms. Likely, some of the Pd adatoms could undergo surface diffusion to the corners and side faces, but remaining as individual atoms. This observation suggests that 2,6-DMPI bound to the surface of the Ag-Pd nanocubes in the pattern illustrated in the top panel of Figure 4.3B. For the case of 50 μL, the $\nu_{NC(Pd)\text{-}atop}$ peak became more dominant while the $\nu_{NC(Ag)\text{-}atop}$ band evolved into a shoulder peak. Meanwhile, we observed two weak peaks at 2007 and

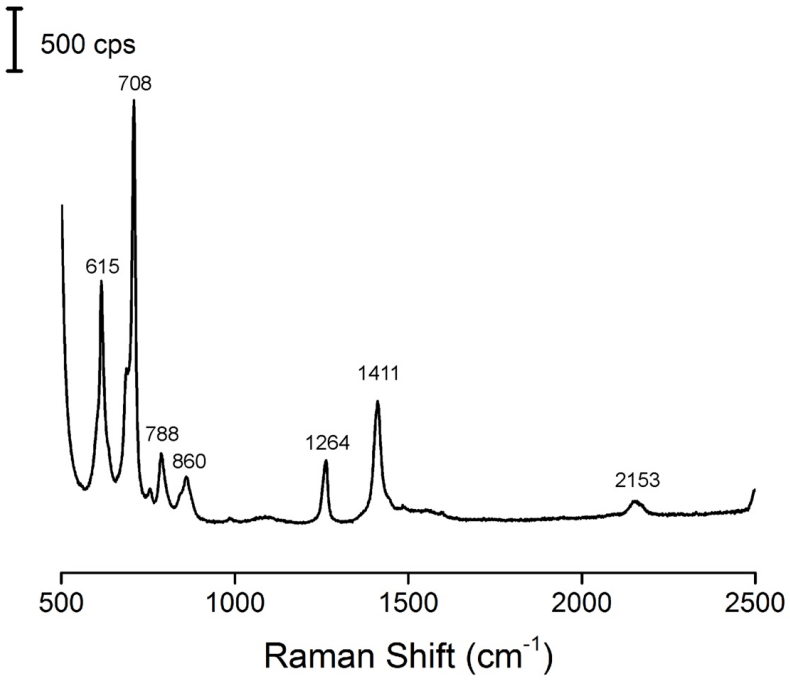

Figure 4.8. The ordinary Raman spectrum of PDMS.

Table 4.3. The ordinary Raman shifts of PDMS and their assignments.

Ordinary (cm^{-1})	Assignment[a]
615	Si-CH_3 symmetric rocking
708	Si-C symmetric stretching
788	CH_3 asymmetric rocking Si-C asymmetric stretching
860	CH_3 symmetric rocking
1264	CH_3 symmetric bending
1411	CH_3 asymmetric bending

[a] Ref. 48.

1977 cm^{-1}, which could be assigned to $\nu_{NC(Pd)\text{-}bridge}$ and $\nu_{NC(Pd)\text{-}hollow}$, respectively.[20] This result indicated that, as more Pd was deposited on the Ag nanocubes, the Pd adatoms would start to form clusters on the edges, and subsequently the corners and side faces because of surface diffusion, leading to the binding pattern depicted in bottom panel of Figure 4.3B.

4.3.4 Probing the Heterogeneous Nucleation of Pd Atoms on Ag nanocubes by In Situ SERS

One of the challenges in using the *ex situ* SERS method to monitor the deposition of Pd on Ag nanocubes is that the samples often need to go through several centrifugation steps prior to SERS measurements. In this case, it is possible that the Pd adatoms can migrate from the original sites of deposition during the sample preparation process, making it difficult to capture the original arrangements of Pd adatoms during deposition. One approach to eliminate this ambiguity is to directly introduce 2,6-DMPI into the reaction solution to monitor the Pd atoms being deposited on Ag nanocubes through *in situ* SERS. In a typical experiment, we prepared a standard aqueous solution containing PVP, H_2Asc, and 2,6-DMPI (in ethanol), followed by the addition of Ag nanocubes and then 50 μL of aqueous Na_2PdCl_4 under magnetic stirring at room temperature (21 °C). Aliquots were sampled from the reaction solution for immediate characterization by SERS.

Figure 4.9 shows a series of Raman/SERS spectra obtained by withdrawing samples from the reaction solution at different time points and then subjecting to Raman measurements (see details in 4.2 Experimental Section). The Raman spectrum recorded from the aqueous solution containing PVP, H_2Asc, and 2,6-DMPI only showed a set of peaks that could be assigned to the vibrational bands of PDMS (marked by solid stars)[33]

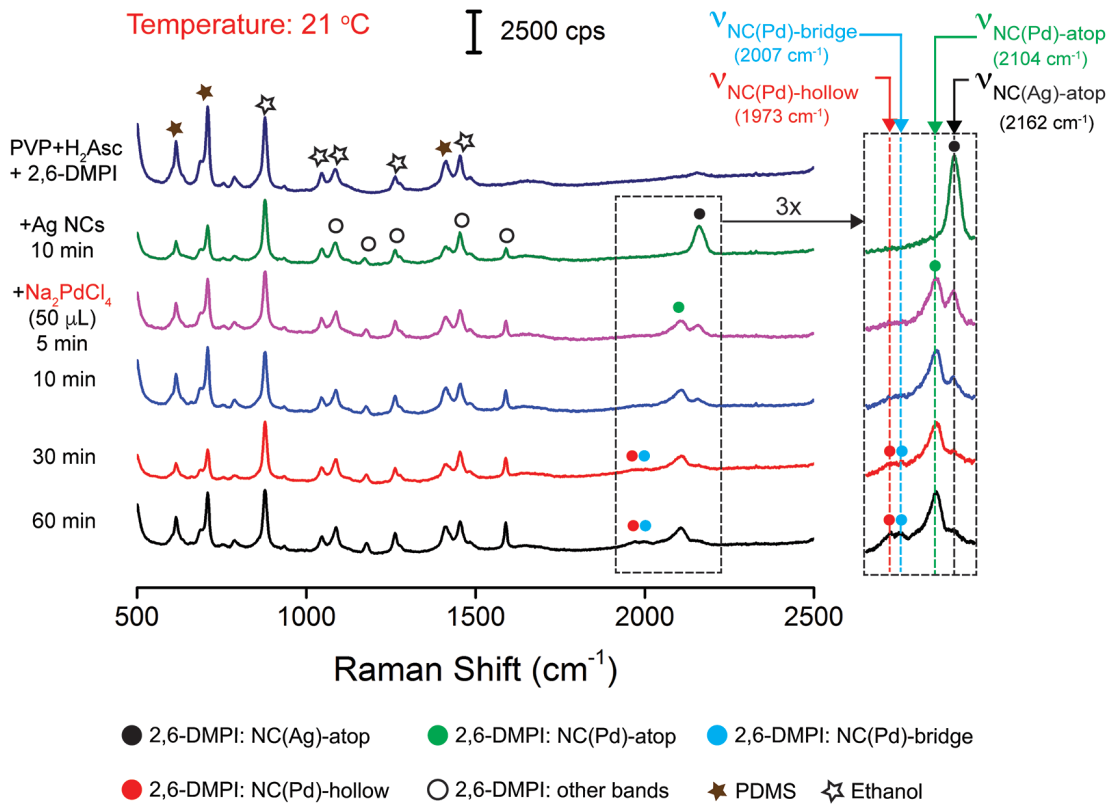

Figure 4.9. Raman spectrum recorded from an aqueous solution containing 2,6-DMPI (pre-dissolved in ethanol), H_2Asc, and PVP and *in situ* SERS spectra of 2,6-DMPI collected from an aqueous suspension of 40-nm Ag nanocubes, 2,6-DMPI, H_2Asc, and PVP before and after the addition of 50 μL of Na_2PdCl_4 precursor at room temperature (21 °C).

and ethanol (marked by open stars, see Figure 4.10 for an ordinary Raman spectrum of ethanol and Table 4.4 for the peak assignments).[34] In fact, we could use the ethanol peak at 879 cm^{-1} as an internal standard to calibrate the SERS spectra because the position and peak intensity of this band remained essentially the same in the entire course of an experiment. After 10 min post the addition of Ag nanocubes, the peak of $\nu_{NC(Ag)\text{-}atop}$ at 2162 cm^{-1} (marked by black dot) appeared on the spectrum, indicating the adsorption of

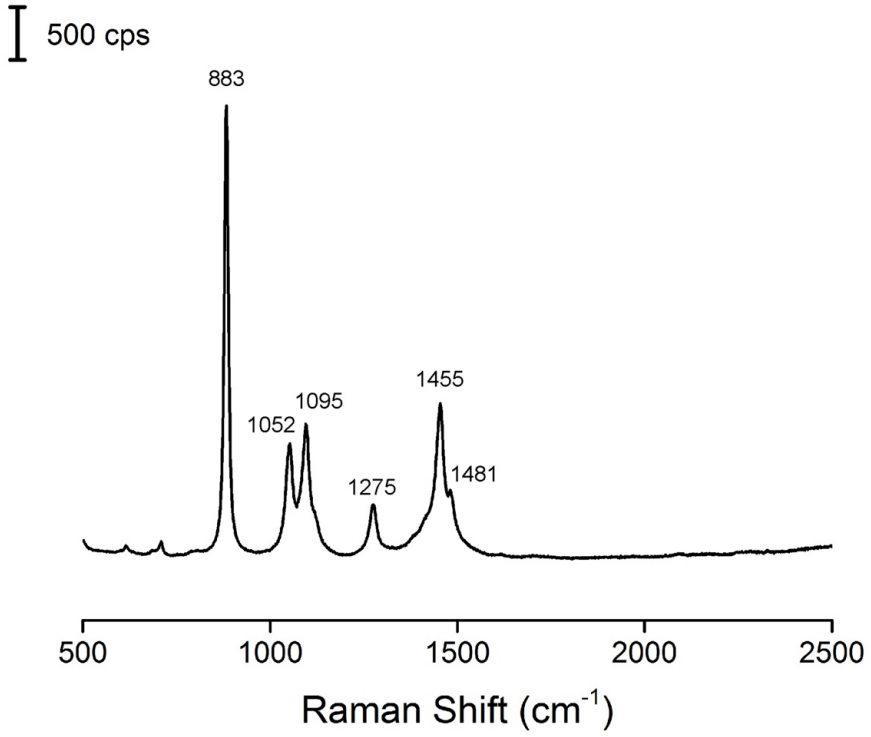

Figure 4.10. The ordinary Raman spectrum of ethanol.

Table 4.4. The ordinary Raman shifts of ethanol and their assignments.

Solution Raman (cm^{-1})	Ordinary (cm^{-1})	Assignment[a]
879	883	ν_{C-C}
1045	1052	ν_{C-O}
1088	1095	CH_3 rock
1276	1275	CH_2 wag
1455	1455	CH_3 bend
1483	1481	CH_3 bend

[a] Ref. 49.

2,6-DMPI onto the surface of Ag nanocubes. When aqueous Na_2PdCl_4 was introduced, we argued that the reduction of Na_2PdCl_4 by H_2Asc at room temperature should undergo a solution-phase reduction for the generation of Pd atoms,[35] followed by their initial deposition onto the edges of Ag nanocubes while surface diffusion could move some of the Pd adatoms onto the corners and side faces. At t = 5 min post the introduction of Na_2PdCl_4, we observed the $\nu_{NC(Pd)\text{-}atop}$ band at 2104 cm^{-1} (marked by green dot) while the $\nu_{NC(Ag)\text{-}atop}$ band was still positioned at 2162 cm^{-1} although its peak intensity had dropped. The ratio between the peak intensities of the $\nu_{NC(Pd)\text{-}atop}$ and $\nu_{NC(Ag)\text{-}atop}$ bands was 1.40:1. This result suggests that a small number of Pd atoms derived from the solution-phase reduction nucleated from the edges of the Ag nanocubes in the form of individual Pd adatoms, leading to the formation of a surface consisting of both Ag and Pd atoms, to which the 2,6-DMPI molecules would bind in the atop configuration.

As the reaction progressed to t = 10 min, the positions of all peaks in the spectra remained the same except that there was an increase in the intensity ratio between the $\nu_{NC(Ag)\text{-}atop}$ and $\nu_{NC(Pd)\text{-}atop}$ bands to 2.32:1. At t = 30 min, the $\nu_{NC(Ag)\text{-}atop}$ band became a shoulder peak while the $\nu_{NC(Pd)\text{-}atop}$ band gained dominance. In addition, we observed two new weak peaks (still relatively weak) at 2007 and 1973 cm^{-1}, which could be assigned to $\nu_{NC(Pd)\text{-}bridge}$ and $\nu_{NC(Pd)\text{-}hollow}$, respectively. By t = 60 min, the $\nu_{NC(Pd)\text{-}bridge}$ and $\nu_{NC(Pd)\text{-}hollow}$ bands became well-identified as the $\nu_{NC(Pd)\text{-}atop}$ peak remained essentially unchanged. The appearance of $\nu_{NC(Pd)\text{-}bridge}$ and $\nu_{NC(Pd)\text{-}hollow}$ bands indicated that, as more and more Pd was deposited on the edges of the Ag nanocube, the Pd adatoms started to evolve into monolayer and then multilayers on the edges of a nanocube, followed by surface diffusion to the corners and side faces. As shown in Figure 4.3B, the hollow configuration is only

allowed for Pd atoms deposited on the {111} facets at the corner sites as constrained by the atomic arrangement. As for the bridge configuration, it is allowed for Pd adatoms deposited on both the {110} and {100} facets, corresponding to the edges and side faces. The observation of $\nu_{NC(Pd)\text{-}atop}$ peak suggested that some of the Pd atoms could still be deposited on the surface as individual atoms.

Table 4.5. The contents of Pd and Ag in the solid product and supernatant using ICP-MS analysis. The sample was prepared by the injection volume of 50 μL Na_2PdCl_4 to the suspension of Ag nanocubes in the presence of H_2Asc, PVP, and 2,6-DMPI.

Samples	Measured conc. of Ag (μg/L)	Measured conc. of Pd (μg/L)	Conversion rate of Pd (%)[a]
Ag nanocubes	4.6×10^6		
Na_2PdCl_4 solution (0.2 mM)		1.5×10^4	
Ag-Pd nanocubes			
Added Na_2PdCl_4		245.9	
Solid sample		104.0	42.3%
Supernatant		107.0	

[a]The conversion rate of Pd (%) was calculated from the mass ratio of Pd in the solid sample to the Pd in added Na_2PdCl_4.

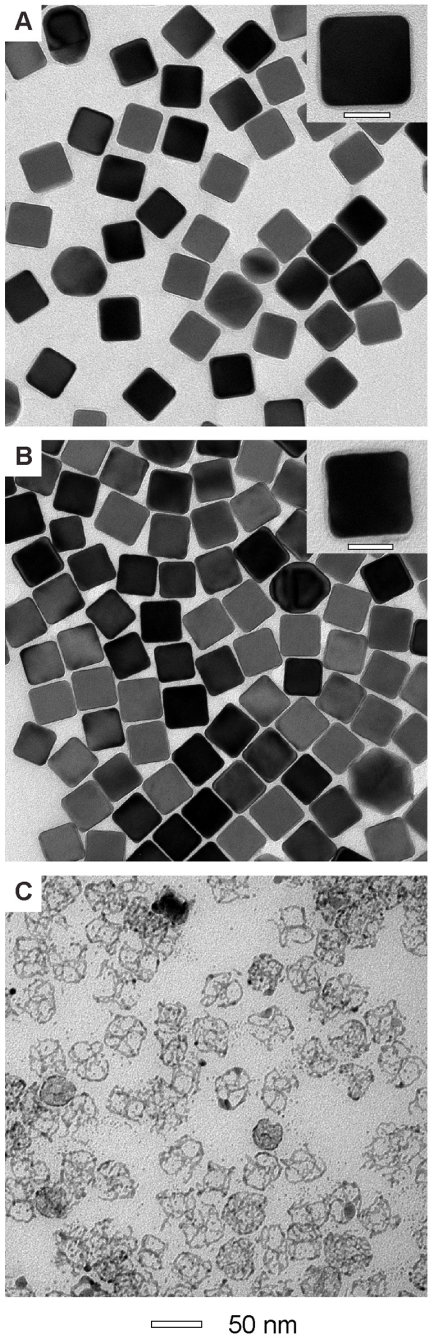

Figure 4.11. (A, B) TEM images of Ag-Pd nanocubes prepared by reacting 40 nm Ag nanocubes with 50 μL and 600 μL of aqueous Na_2PdCl_4, respectively, in the presence of 2,6-DMPI, H_2Asc and PVP, and (C) the resultant Ag-Pd nanoframes after the removal of Ag from Ag-Pd nanocubes in (B) by an etchant based on $Fe(NO_3)_3/HNO_3$. The inset scale bar is 20 nm.

We further used ICP-MS to analyze the sample obtained at the reaction time of 60 min. Our results indicate that 42.3% of the added Na_2PdCl_4 was converted to Pd atoms, followed by their deposition onto the Ag nanocubes (Table 4.5). In comparison with the conversion rate of 46.6% for Na_2PdCl_4 when 2,6-DMPI was not involved in the reaction solution (see Table 4.1), we argued that the SERS probe did not interfere with the reduction of Na_2PdCl_4. We further used TEM to characterize the sample. Figure 4.11A indicates that the morphology of the nanoparticles was essentially the same as those shown in Figure 4.4A where no 2,6-DMPI was added into the reaction solution. When the injection volume was increased to 600 μL in the presence of 2,6-DMPI, Figure 4.11B, C shows the transformation of nanocubes into nanoframes after the removal of Ag with an aqueous mixture of $Fe(NO_3)_3$ and HNO_3, in agreement with the results shown in Figure 4.4C, D. Taken together, we believed that the presence of 2,6-DMPI molecules in the reaction solution did not alter the reduction pathway of Na_2PdCl_4, nor the deposition of the resultant Pd atoms, which still preferred heterogeneous nucleation from the edges of the Ag nanocubes.

We also conducted another control experiment by following the same *in situ* protocol except that no H_2Asc was added. As shown in Figure 4.12, after 10 min post the addition of Ag nanocubes, we observed the peak of $\nu_{NC(Ag)\text{-}atop}$ at 2179 cm^{-1} in the SERS spectrum, indicating the adsorption of 2,6-DMPI onto the surface of the Ag nanocubes. However, when aqueous Na_2PdCl_4 was introduced, we did not resolve any peaks associated with the $\nu_{NC(Pd)\text{-}atop}$, $\nu_{NC(Pd)\text{-}bridge}$, and $\nu_{NC(Pd)\text{-}hollow}$ bands up to t = 60 min. The $\nu_{NC(Ag)\text{-}atop}$ band also became too weak to be identified. These results are completely different from those SERS spectra shown in Figure 4.9 when H_2Asc was involved in the synthesis. In the absence of

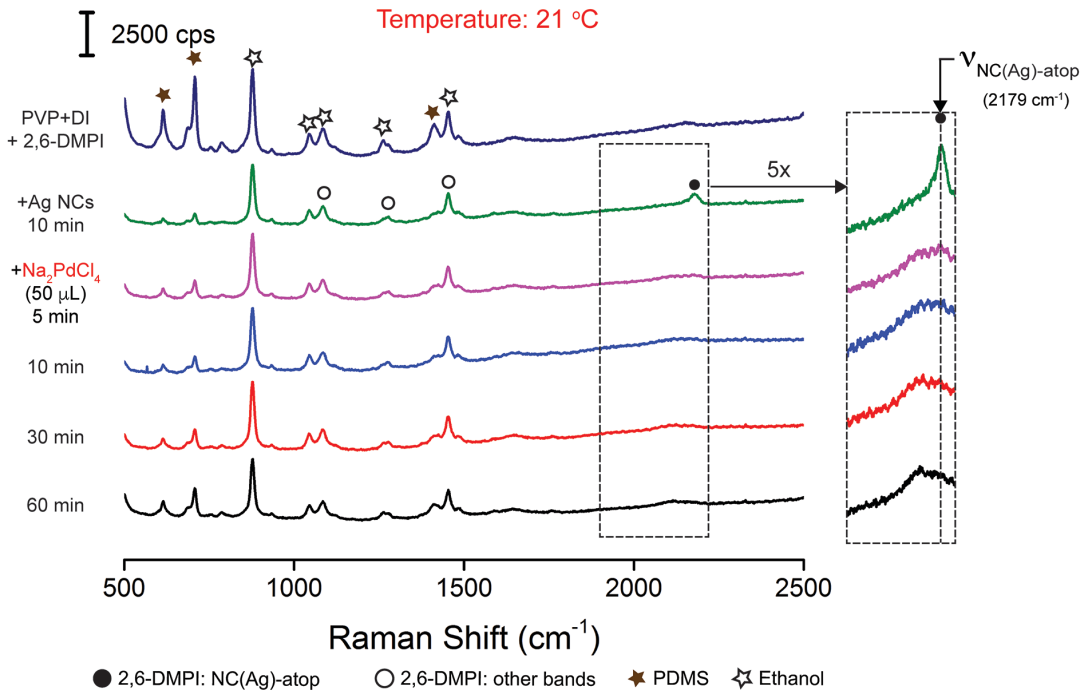

Figure 4.12. Raman spectrum recorded from an aqueous solution containing 2,6-DMPI (in ethanol), and PVP and *in situ* SERS spectra of 2,6-DMPI collected from an aqueous suspensions of 40 nm Ag nanocubes, 2,6-DMPI, and PVP before and after the addition of 50 μL of Na_2PdCl_4 precursor at room temperature (21 °C).

H_2Asc, we argue that the galvanic replacement reaction would dominate. Some of the resultant Pd atoms will be deposited on the side faces of the Ag nanocubes, reducing the number of Pd atoms deposited on the edges where hot spots are located and thus making it difficult to detect the Pd atoms by SERS. Additionally, any dissolution of Ag from the sharp edges or corners of the nanocubes would deteriorate the SERS activity. Taken together, we believe that this *in situ* method also has the capability to distinguish the deposition of Pd on Ag nanocubes *via* galvanic replacement *versus* chemical reduction.

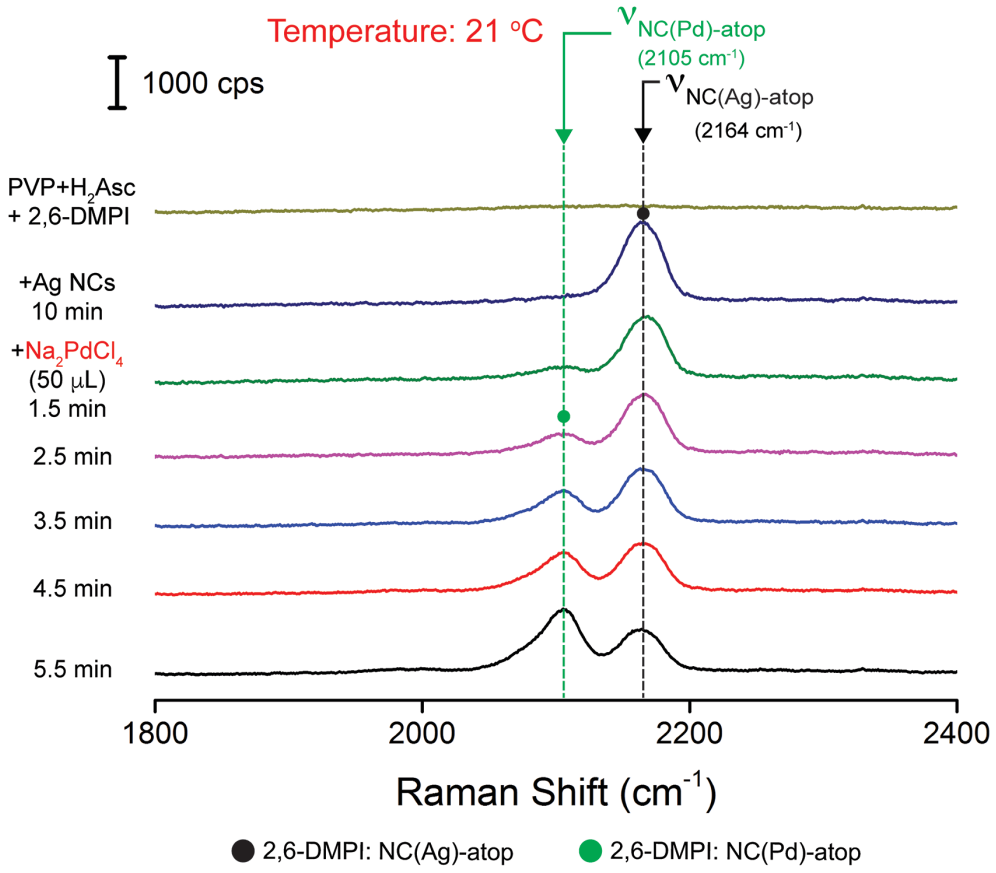

Figure 4.13. Raman spectrum recorded from an aqueous solution containing 2,6-DMPI (in ethanol), H_2Asc, and PVP and *in situ* SERS spectra of 2,6-DMPI collected from an aqueous suspensions of 40 nm Ag nanocubes, 2,6-DMPI, H_2Asc, and PVP before and after the addition of 50 μL of Na_2PdCl_4 precursor at room temperature (21 °C). The measurement was taken every one minute using the *static* mode (centered at 2000 cm^{-1}) with the collection time of 10 s. The spectra show a portion of the signals from 1800 cm^{-1} to 2400 cm^{-1}.

It should be pointed out that we performed *in situ* SERS measurements by withdrawing aliquots of 25 μL from the reaction solution under stirring at different reaction time points, followed by addition of the sample into a PDMS cell, optimization of optics and the spectrometer, and collection of a Raman spectrum in the *extended* mode (see details

in 4.2 Experimental Section). Typically, it took 1-2 min to get the sample ready for spectral collection, together with another 2 min to complete the collection. The entire process took about 4 min from the withdrawal of sample to the completion of spectral recording. The time point marked in Figure 4.9 corresponds to the moment at which the collection of spectrum was initiated, relative to $t = 0$ min when the Na_2PdCl_4 precursor was introduced. To capture the heterogeneous nucleation events within a period of time shorter than 5 min, we revised our standard procedure by collecting the time-dependent SERS spectra in the *static* mode (see details in 4.2 Experimental Section). Figure 4.13 shows a series of Raman/SERS spectra obtained by withdrawing one sample from the reaction solution at $t = 50$ s after the addition of Na_2PdCl_4, and then subjecting it to Raman measurements from $t = 1.5$ min for four consecutive scans up to $t = 5.5$ min. The spectra indicate that the ratio between the peak intensities of the $\nu_{NC(Pd)\text{-}atop}$ and $\nu_{NC(Ag)\text{-}atop}$ bands was increased from 0.15 to 1.49 as the time point was increased $t = 1.5$ to $t = 5.5$ min, confirming that the deposition of Pd atoms occurred rapidly on the edges of the Ag nanocubes in the form of individual Pd adatoms. As a result, a surface was created, to which the 2,6-DMPI molecules could bind to the Ag and Pd atoms in the atop configuration.

4.3.5 Investigating the Role of Temperature in Controlling the Heterogeneous Nucleation of Pd on Ag Nanocubes.

The *in situ* SERS method opens an opportunity to investigate the role of reaction temperature in controlling the heterogeneous nucleation and growth of metal nanocrystals. Specifically, we conducted two sets of experiments by immersing the reaction container in an ice bath (at 0 °C) or oil bath (at 40 °C), respectively. Figure 4.14A shows the

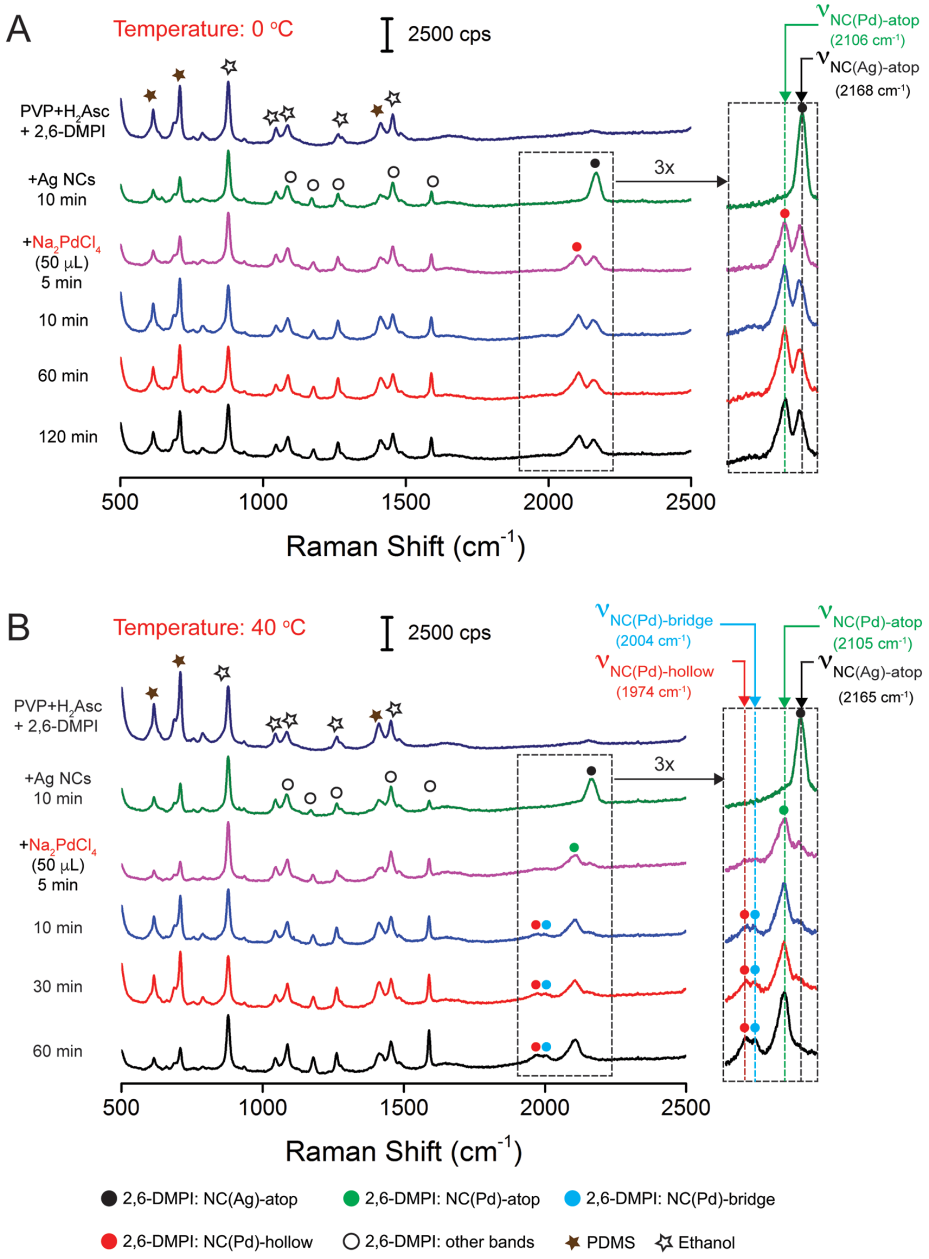

Figure 4.14. Raman spectrum recorded from an aqueous solution containing 2,6-DMPI (pre-dissolved in ethanol), H_2Asc, and PVP and *in situ* SERS spectra of 2,6-DMPI collected from an aqueous suspension of 40 nm Ag nanocubes, 2,6-DMPI, H_2Asc, and PVP before and after the addition of 50 μL of Na_2PdCl_4 precursor at (A) 0 °C (ice bath) and (B) 40 °C (oil bath).

Raman/SERS spectra of the aliquots sampled from the reaction solution held at 0 °C. The Raman spectrum was essentially the same as what was collected when the synthesis was conducted at room temperature (21 °C, see Figure 4.9). After introducing the Ag nanocubes and waiting for 10 min, we observed the $\nu_{NC(Ag)\text{-}atop}$ peak at 2168 cm^{-1}, suggesting that the kinetics for the adsorption of 2,6-DMPI onto the surface of Ag nanocubes was comparable at 0 °C and 21 °C. At t = 5 min post the addition of Na_2PdCl_4, we observed both $\nu_{NC(Pd)\text{-}atop}$ and $\nu_{NC(Ag)\text{-}atop}$ bands appeared at 2106 and 2168 cm^{-1}, respectively, and ratio of their peak intensities was 1.07:1. As the reaction progressed to 10 min, the SERS spectrum only showed a slight increase in peak intensity ratio for the $\nu_{NC(Pd)\text{-}atop}$ and $\nu_{NC(Ag)\text{-}atop}$ bands to 1.34:1. It was difficult to resolve the $\nu_{NC(Pd)\text{-}bridge}$ and $\nu_{NC(Pd)\text{-}hollow}$ bands. The SERS spectra showed very little changes when the reaction time was prolonged from 10 to 120 min. This observation is completely different from the SERS data shown in Figure 4.9 for the synthesis conducted at 21 °C. Specifically, the reduction of Na_2PdCl_4 and thus the deposition of Pd became much slower at a lower temperature, as indicated by the smaller ratio between the peak intensities of $\nu_{NC(Pd)\text{-}atop}$ and $\nu_{NC(Ag)\text{-}atop}$ bands.

In comparison, Figure 4.14B shows the Raman/SERS spectra collected from the reaction solution for the synthesis conducted at 40 °C. Although the Raman spectrum and the SERS spectrum of the Ag nanocubes are similar to those shown in Figure 4.14A, the evolution of the SERS spectra was completely different after the introduction of Na_2PdCl_4. At t = 5 min post the introduction of Na_2PdCl_4, we observed the $\nu_{NC(Pd)\text{-}atop}$ peak at 2105 cm^{-1} but could barely detect the $\nu_{NC(Ag)}$ peak. This result indicated great acceleration for both the reduction of Na_2PdCl_4 and deposition of Pd when the reaction temperature was

raised to 40 °C. At t = 10 min, we could easily resolve $\nu_{NC(Pd)\text{-}bridge}$ and $\nu_{NC(Pd)\text{-}hollow}$ peaks at 2004 and 1974 cm^{-1}, respectively. As the reaction progressed from 10 to 60 min, both $\nu_{NC(Pd)\text{-}bridge}$ and $\nu_{NC(Pd)\text{-}hollow}$ peaks showed major increases in intensity.

Collectively, we believe that the *in situ* SERS spectra at different temperatures provide a clear picture about the reduction, deposition, and surface diffusion processes involved in the nucleation and early-stage deposition of Pd on Ag nanocubes. At 0 °C, both the reduction and deposition kinetics would be retarded while the diffusion process was largely suppressed. In this case, only a small portion of the added Na_2PdCl_4 was reduced for the deposition of Pd as individual adatoms on the Ag surface, resulting in the presence of both Pd and Ag atoms on the outermost surface for binding with 2,6-DMPI in the atop configuration. Because the diffusion of Pd adatoms across the Ag surface was largely suppressed, the SERS spectrum was essentially the same as what was observed at t = 5 min when the reaction time was prolonged. At 40 °C, it is anticipated that the increase in temperature could greatly accelerate the reduction, deposition, and surface diffusion processes. Even at t = 5 min, a significant portion of the Na_2PdCl_4 precursor could be reduced to generate Pd atoms for their deposition on the edges of the Ag nanocubes to create a monolayer of Pd adatoms on Ag, leading to the dominance of $\nu_{NC(Pd)\text{-}atop}$ peak in the absence of $\nu_{NC(Ag)\text{-}atop}$ in the SERS spectrum. As the reaction progressed, more Pd atoms would be deposited on the edges of the Ag nanocubes, and ultimately, more Pd adatoms were able to migrate *via* surface diffusion to the corners and side faces, giving rise of both $\nu_{NC(Pd)\text{-}bridge}$ and $\nu_{NC(Pd)\text{-}hollow}$ peaks. Nevertheless, the $\nu_{NC(Pd)\text{-}atop}$ peak remained in the SERS spectrum because some of the Pd atoms could still exist on the surface as individual atoms.

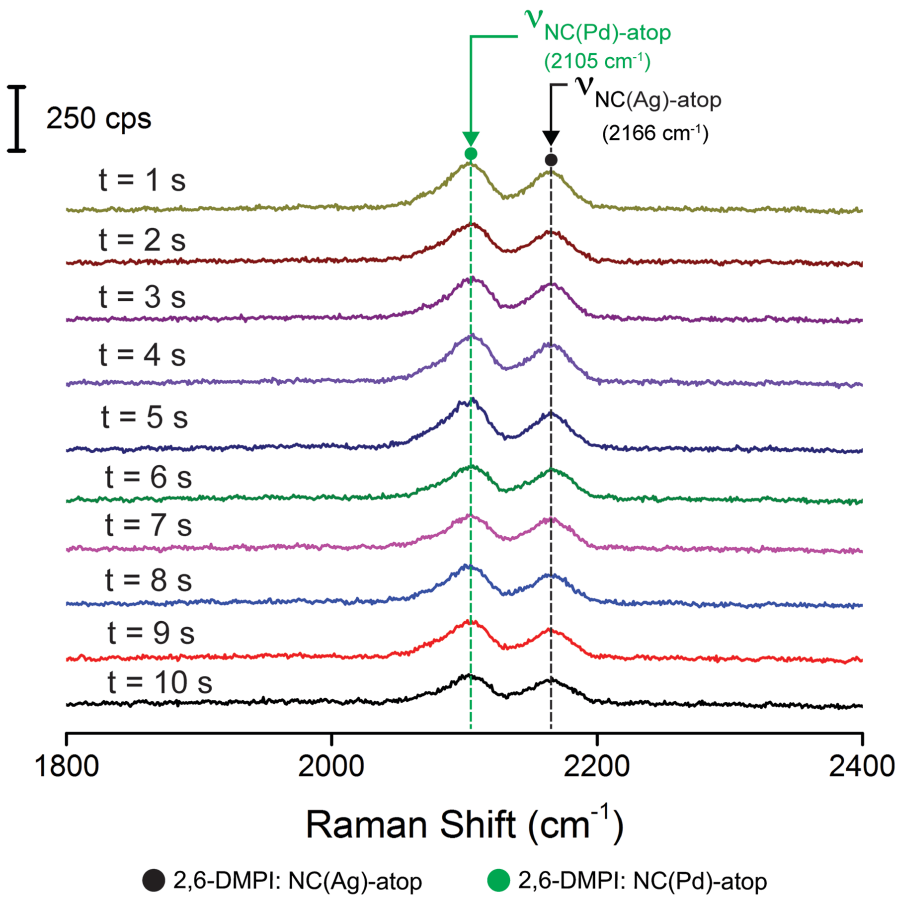

Figure 4.15. *In situ* SERS spectra of 2,6-DMPI collected from an aqueous suspensions of 40 nm Ag nanocubes, 2,6-DMPI, H_2Asc, and PVP after the addition of 50 μL of Na_2PdCl_4 precursor at ice bath (0 °C) starting from t = 5 min. The measurement was recorded every one second using the *static* mode centered at 2000 cm^{-1}. The spectra show only a portion of the signals from 1800 cm^{-1} to 2400 cm^{-1}.

It should be acknowledged that the *in situ* SERS spectra shown in Figure 4.14 were highly reproducible in terms of peak position and intensity as long as the same batch of Ag nanocubes was used. To further evaluate the stability of SERS signal intensity, we performed another set of experiments to collect time-elapsed SERS spectra in the *static* mode (see 4.2 Experimental Section). Because there was very little change to the SERS

spectra at 0 °C after t = 5 min due to the very slow reduction kinetics of the Pd(II) precursor (see Figure 4.14A), we collected another set of *in situ* SERS spectra by keeping the reaction conditions unaltered but changing the Raman collection mode. At t = 5 min post the introduction of Na_2PdCl_4, we started to record SERS spectra using the *static* mode. As shown in Figure 4.15, the SERS signals were rather stable up to a duration of 10 s at a collection time of 1 s. Based on the ten data points of peak intensity for the $\nu_{NC(Pd)\text{-}atop}$ band, we estimated a fluctuation of ~17% in SERS signal over a period of 10 s. Taken together, we believe that this *in situ* SERS technique embraces a great potential to extract reliable data for kinetic analysis.

4.3.6 Examining the Role of Pd(II) Precursor in Affecting the Deposition of Pd on Ag Nanocubes.

To further demonstrate the unique capacity of this *in situ* method in revealing the mechanistic details behind the deposition of Pd on Ag nanocubes, we replaced the Na_2PdCl_4 precursor with Na_2PdBr_4 while keeping all other parameters unaltered. Most recently, Xia and co-workers demonstrated that the reduction of Na_2PdBr_4 by H_2Asc would take a surface pathway at 0 °C.[35] In this case, the precursor ions would initially adsorb onto the surface of a nanocrystal, followed by their reduction to atoms. Figure 4.16A shows a set of Raman/SERS spectra collected from the reaction solution of a synthesis conducted in an ice bath (0 °C) when 50 μL of aqueous Na_2PdBr_4 was introduced. The Raman spectrum and the SERS spectrum of the Ag nanocubes were essentially the same as those shown Figure 4.14A. At t = 5 min post the introduction of Na_2PdBr_4 solution, we observed a strong $\nu_{NC(Pd)\text{-}atop}$ peak and a weak $\nu_{NC(Ag)\text{-}atop}$ peak, together with two weak peaks of

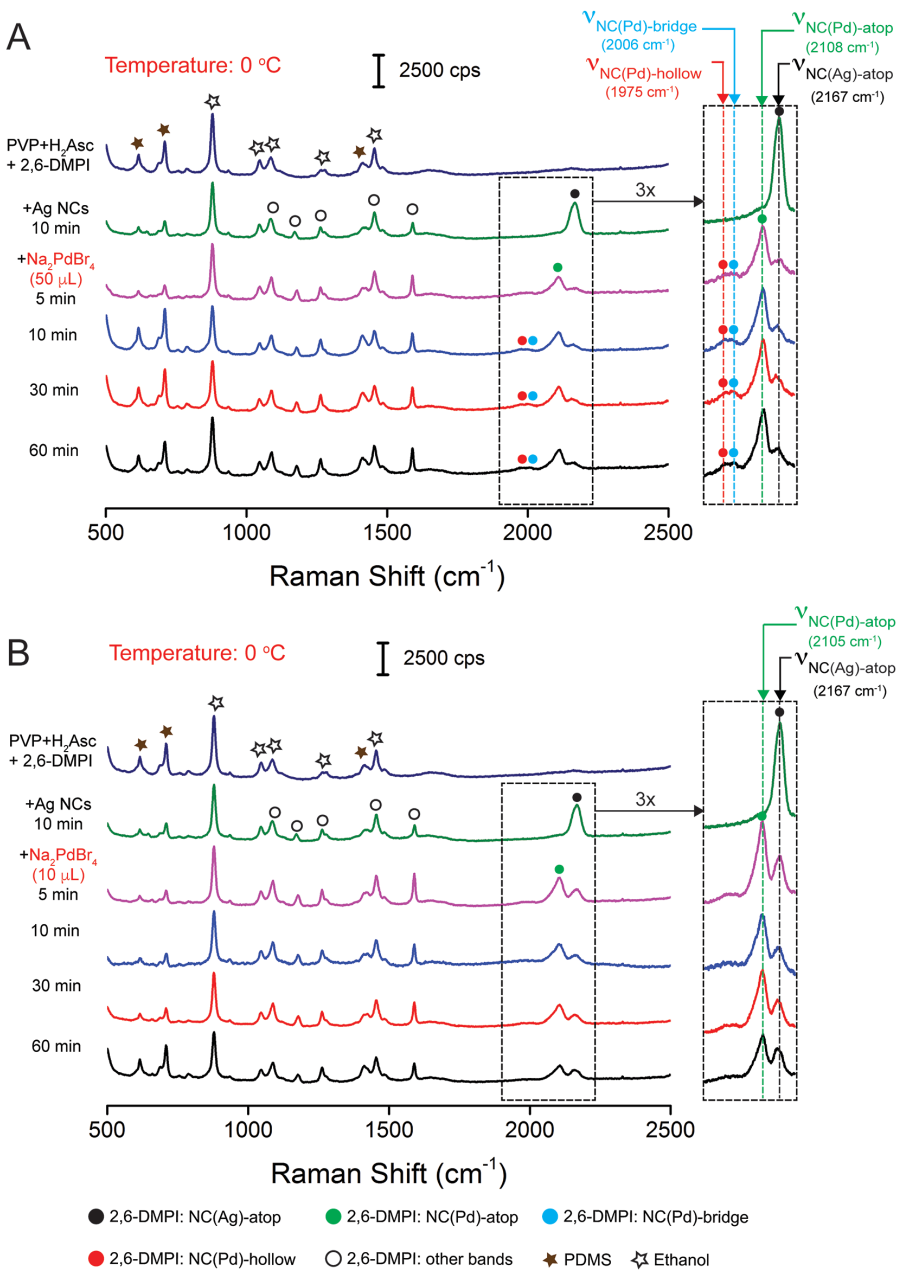

Figure 4.16. Raman spectrum recorded from an aqueous solution containing 2,6-DMPI (pre-dissolved in ethanol), H_2Asc, and PVP, and time-dependent SERS spectra of 2,6-DMPI collected from an aqueous suspension of 40-nm Ag nanocubes, 2,6-DMPI, H_2Asc, and PVP before and after the addition of (A) 50 μL and (B) 10 μL of aqueous Na_2PdBr_4 held at 0 °C with an ice bath.

$\nu_{NC(Pd)\text{-}bridge}$ and $\nu_{NC(Pd)\text{-}hollow}$ in the spectrum. This result is similar to the spectrum at t = 5 min in Figure 4.14B when Na_2PdCl_4 was used as a precursor at 40 °C, but it is completely different from what is shown in Figure 4.14A at t = 5 min and at 0 °C. From 10 to 60 min, the SERS spectra show little change except that both the $\nu_{NC(Pd)\text{-}bridge}$ and $\nu_{NC(Pd)\text{-}hollow}$ bands at 2006 and 1975 cm^{-1} became more dominant.

According to the surface reduction mechanism, we argued that the $PdBr_4^{2-}$ ions would first adsorb onto the {110}, {111}, and {100} facets on the Ag nanocubes *via* collisions, followed by a surface reduction pathway to generate Pd atoms by H_2Asc. Because the adsorption of $PdBr_4^{2-}$ ions could still occur at 0 °C, a large number of Pd atoms were generated at t = 5 min, leading to a high coverage of Pd atoms across the surface of the Ag nanocubes. In this case, the $\nu_{NC(Ag)\text{-}atop}$ peak became very weak while $\nu_{NC(Pd)\text{-}atop}$, $\nu_{NC(Pd)\text{-}bridge}$ and $\nu_{NC(Pd)\text{-}hollow}$ bands all appeared in the SERS spectrum. To further support our argument, we performed another experiment with 10 μL of Na_2PdBr_4 solution while leaving other conditions unchanged. In this case, we hypothesize that fewer $PdBr_4^{2-}$ ions would adsorb onto the surface of the Ag nanocubes, leading to the generation of Pd as individual adatoms, with which 2,6-DMPI would bind in the atop configuration only. As shown in Figure 4.16B, after the injection of aqueous Na_2PdBr_4, we only observed the $\nu_{NC(Pd)\text{-}atop}$ and $\nu_{NC(Ag)\text{-}atop}$ peaks at 2105 and 2167 cm^{-1} with essentially no $\nu_{NC(Pd)\text{-}bridge}$ and $\nu_{NC(Pd)\text{-}hollow}$ in the period from 5–60 min. This observation supports the surface reduction mechanism.

We further evaluated the role of temperature in controlling the deposition of Pd on the Ag nanocubes using Na_2PdBr_4 as the Pd(II) precursor. Figure 4.17 shows a set of

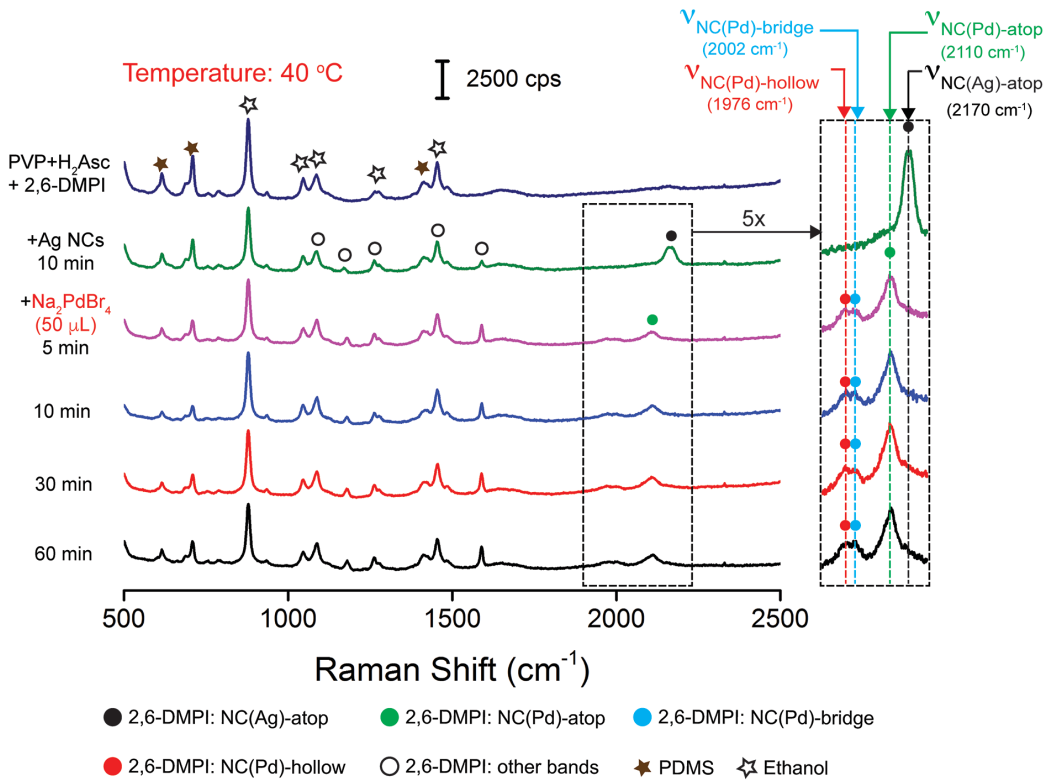

Figure 4.17. Raman spectrum recorded from an aqueous solution containing 2,6-DMPI (pre-dissolved in ethanol), H_2Asc, and PVP, and time-dependent SERS spectra of 2,6-DMPI collected from an aqueous suspension of 40 nm Ag nanocubes, 2,6-DMPI, H_2Asc, and PVP before and after the addition of 50 μL of Na_2PdBr_4 at 40 °C with an oil bath.

Raman/SERS spectra collected from the reaction solution of a synthesis conducted in an oil bath (40 °C) when 50 μL of aqueous Na_2PdBr_4 was introduced. At t = 5 min post the addition of Na_2PdBr_4 solution, we observed all the peaks for $\nu_{NC(Pd)\text{-}atop}$, $\nu_{NC(Pd)\text{-}bridge}$, and $\nu_{NC(Pd)\text{-}hollow}$. This result is similar to the spectrum at t = 5 min in Figure 4.16A when Na_2PdBr_4 was used as a precursor at 0 °C except that we could not identify the $\nu_{NC(Ag)\text{-}atop}$ peak. We expect that the surface diffusion of Pd adatoms would be accelerated at 40 °C, leading to a decrease for the Ag atoms on the surface of the Ag-Pd nanocubes. It is worth

emphasizing that this observation is completely different from what is shown in Figure 4.14B at t = 5 min when 50 μL of Na_2PdCl_4 was involved in the reaction solution at 40 °C. In the latter case, we could only resolve the $\nu_{NC(Pd)\text{-}atop}$ peak, not the $\nu_{NC(Pd)\text{-}bridge}$ and $\nu_{NC(Pd)\text{-}hollow}$ peaks. From 10 to 60 min, the SERS spectra in Figure 4.17 remained essentially unchanged except that both the $\nu_{NC(Pd)\text{-}bridge}$ and $\nu_{NC(Pd)\text{-}hollow}$ bands became more predominant, consistent with those shown in Figure 4.16A at 0 °C. These results are consistent with a surface reduction mechanism at 40 °C.[35] Collectively, our *in situ* SERS results suggest that surface reduction could serve as an effective route to the deposition of Pd on Ag nanocubes.

4.4 Conclusions

In summary, we have demonstrated the use of 2,6-DMPI as a sensitive probe for *in situ* atomic-level tracking of the heterogeneous nucleation of Pd on Ag nanocubes by SERS. Because the isocyanide group binds to Ag and Pd *via* σ donation and π-back donation, respectively, we can simply monitor the deposition of Pd on Ag nanocubes by following the distinctive stretching frequency of 2,6-DMPI, $\nu_{NC,}$ using SERS. More significantly, we discovered that the isocyanide group could bind to one, two, and three adjacent Pd atoms to generate the atop, bridge, and hollow binding configurations, respectively, to display different vibrational frequencies. This unique feature makes it possible to use 2,6-DMPI as a distinctive reporter for characterizing Pd atoms being deposited onto different types of facets on Ag nanocubes with different arrangements. By directly introducing 2,6-DMPI molecules into the reaction solution, we further demonstrated atomic-level dynamic tracking of heterogeneous nucleation of Pd on Ag

nanocubes by monitoring the ν_{NC} bands through time-dependent SERS spectra. This *in situ* tracking method with atomic resolution allows us to investigate the roles played by reaction temperature and the type of Pd(II) precursor in affecting the heterogeneous nucleation and deposition of Pd on Ag nanocrystals. With further development, this technique will also support the rational synthesis of bimetallic nanocrystals involving other noble metals such as Ru, Rh, and Ir.

4.5 Notes to Chapter 4

Part of this chapter is adapted from the paper "In Situ Atomic-Level Tracking of Heterogeneous Nucleation in Nanocrystal Growth with an Isocyanide Molecular Probe" published in *Journal of the American Chemical Society*.

4.6 Appendix

4.6.1 Calculation of the Number of Ag Nanocubes in the Reaction

Based on the ICP-MS results from Table 4.1, we obtained the concentration of Ag in the original Ag nanocube stock solution is 4.565×10^6 μg/L (or 4.565 mg/mL). Our TEM results indicate that the average edge length of Ag nanocubes is 40.3 nm. Given that we used 25 μL of Ag nanocubes for the synthesis of Ag-Pd nanocubes, the number of nanocubes in the reaction solution was calculated as follows.

Calculation of the number of Ag atoms, n_1(Ag), in the reaction solution:

$$n_1(Ag) = [(4.565\,mg/mL \times 0.025\,mL)/(107.86\times 10^3 mg/mol)] \times 6.023\times 10^{23} atoms/mol = 6.3\times 10^{17}\ atoms \quad \textbf{(4.1)}$$

Calculation of the number of Ag atoms in a Ag nanocube, n_2(Ag), with an edge length of 40.3 nm using unit cell approach with the lattice constant of Ag at 0.408 nm:

$$n_2(Ag) = [(40.3\,nm)^3/(0.408\,nm)^3]\times 4 = 3.85\times 10^6\ atoms \quad \textbf{(4.2)}$$

Calculation of number of Ag nanocubes, n_3(nanocube) in the reaction solution:

$$n_3(nanocube) = (6.3\times 10^{17} atoms)/(3.85\times 10^6 atoms) = 1.64\times 10^{11}\ Agnanocubes \quad \textbf{(4.3)}$$

4.6.2 Calculation of Pd Atoms on Each Edge of a Ag Nanocube

Based on the ICP-MS results from Table 4.1, the measured concentration of Pd in the solid sample prepared from 50 μL Na_2PdCl_4 was 114.5 μg/L. Because the total volume of reaction solution was 3.05 mL, we calculate the number of Pd atoms on each edge of a Ag nanocube with an edge length of 40.3 nm as follows:

Calculation of the number of Pd atoms, n_1(Pd), on Ag-Pd nanocubes:

$$n_1(Pd) = [(1.145\times 10^{-4}\ g/L \times 3.05\times 10^{-3} L)/(106.42\ g/mol)] \times 6.023\times 10^{23} atoms/mol = 1.98\times 10^{15}\ atoms \quad \textbf{(4.4)}$$

Calculation of the number of Pd atoms, n_2(Pd), deposited to each edge of one Ag nanocube:

$$n_2(Pd) = (1.98\times10^{15}\ atoms/1.64\times10^{11} cubes)/12 \\ = 1006\ atoms/edge \quad \textbf{(4.5)}$$

4.6.3 Calculation of the Number of Pd Atoms that Are Needed to Form One Monolayer of Pd on Edge of a Ag Nanocube

Based on the dimension of a Ag nanocube as shown in Figure 4.5, we calculated the total surface area of edges (Ag(110) surfaces), s(Ag 110), of Ag nanocubes (1.64×10^{11}) involved in the reaction solution as follows:

$$s(Ag\ 110) = (1.64\times10^{11}\ cubes \times (30\ nm \times 1.5\ nm \times 12)/cube \\ = 8.86\times10^{13} nm^2 \quad \textbf{(4.6)}$$

Next, we assumed that Pd atoms would form one unit cell layer of Pd to form one monolayer on each edge of Ag nanocube. We also argued that the thickness of the layer is equivalent to the lattice constant of Pd at 0.389 nm. As such, we calculated the total volume of Pd atoms, v(Pd), in reaction solution as follows:

$$v(Pd) = (8.86\times10^{13}\ nm^3\times0.389\ nm = 3.45\times10^{13} nm^3 \quad \textbf{(4.7)}$$

Next, we calculated the number of Pd atoms in the reaction solution, n_1(Pd), using the unit cell approach as follows:

$$n_1(Pd) = [3.45\times10^{13}\ nm^3/(0.389\ nm)^3/unit\ cell\ ]\times4 = 2.34\times10^{15}\ atoms \quad \textbf{(4.8)}$$

Finally, we calculated the number of Pd atoms, n_2(Pd), needed to cover each edge of one Ag nanocube as follows:

$$n_2(Pd) = (2.34\times10^{15}\ atoms/1.64\times10^{11} cubes)/12 = 1189\ atoms/edge \quad \textbf{(4.9)}$$

4.7 References

[1] Habas, S. E.; Lee, H.; Radmilovic, V.; Somorjai, G. A.; Yang, P., Shaping Binary Metal Nanocrystals through Epitaxial Seeded Growth. *Nat. Mater.* **2007**, *6*, 692−697.

[2] Rycenga, M.; Cobley, C. M.; Zeng, J.; Li, W.; Moran, C. H.; Zhang, Q.; Qin, D.; Xia, Y., Controlling the Synthesis and Assembly of Silver Nanostructures for Plasmonic Applications. *Chem. Rev.* **2011**, *111*, 3669–3712.

[3] Tsao, Y. C.; Rej, S.; Chiu, C. Y.; Huang, M. H., Aqueous Phase Synthesis of Au-Ag Core-Shell Nanocrystals with Tunable Shapes and Their Optical and Catalytic Properties. *J. Am. Chem. Soc.* **2014**, *136*, 396−404.

[4] Park, J.; Zhang, L.; Choi, S.-I.; Roling, L. T.; Lu, N.; Herron, J. A.; Xie, S.; Wang, J.; Kim, M. J.; Mavrikakis, M.; Xia, Y., Atomic Layer-by-Layer Deposition of Platinum on Palladium Octahedra for Enhanced Catalysts toward the Oxygen Reduction Reaction. *ACS Nano* **2015**, *9*, 2635−2647.

[5] Li, J.; Liu, J.; Yang, Y.; Qin, D., Bifunctional Ag@Pd-Ag Nanocubes for Highly Sensitive Monitoring of Catalytic Reactions by Surface-Enhanced Raman Spectroscopy. *J. Am. Chem. Soc.* **2015**, *137*, 7039−7042.

[6] Xie, S.; Lu, N.; Xie, Z.; Wang, J.; Kim, M. J.; Xia, Y., Synthesis of Pd-Rh Core-Frame Concave Nanocubes and Their Conversion to Rh Cubic Nanoframes by Selective Etching of the Pd Cores. *Angew. Chem. Int. Ed.* **2012**, *51*, 10266−10270.

[7] Fan, Z.; Zhang, H., Template Synthesis of Noble Metal Nanocrystals with Unusual Crystal Structures and Their Catalytic Applications. *Acc. Chem. Res.* **2016**, *49*, 2841−2850.

[8] Egerton, R. F., *Electron Energy-Loss Spectroscopy in the Electron Microscope*. Springer Science & Business Media: 2011.

[9] Xia, X.; Wang, Y.; Ruditskiy, A.; Xia, Y., 25th Anniversary Article: Galvanic Replacement: A Simple and Versatile Route to Hollow Nanostructures with Tunable and Well-Controlled Properties. *Adv. Mater.* **2013**, *25*, 6313-6333.

[10] Park, J.; Zhang, L.; Choi, S.-I.; Roling, L. T.; Lu, N.; Herron, J. A.; Xie, S.; Wang, J.; Kim, M. J.; Mavrikakis, M.; Xia, Y., Atomic Layer-by-Layer Deposition of Platinum on Palladium Octahedra for Enhanced Catalysts toward the Oxygen Reduction Reaction. *ACS Nano* **2015**, *9*, 2635−2647.

[11] Gilroy, K. D.; Ruditskiy, A.; Peng, H.-C.; Qin, D.; Xia, Y., Bimetallic Nanocrystals: Syntheses, Properties, and Applications. *Chem. Rev*. **2016**, *116*, 10414-10472.

[12] Zhao, M.; Wang, X.; Yang, X.; Gilroy, K. D.; Qin, D.; Xia, Y., Hollow Metal Nanocrystals with Ultrathin, Porous Walls and Well-Controlled Surface Structures. *Adv. Mater.* **2018**, 1801956.

[13] Zhang, Y.; Liu, J.; Ahn, J.; Xiao, T.-H.; Li, Z.-Y.; Qin, D., Observing the Overgrowth of a Second Metal on Silver Cubic Seeds in Solution by Surface-Enhanced Raman Scattering. *ACS Nano* **2017,** *11*, 5080-5086.

[14] Joo, S. W.; Han, S. W.; Kim, K., Adsorption of 1,4-Benzenedithiol on Gold and Silver Surfaces: Surface-Enhanced Raman Scattering Study. *J. Colloid Interface Sci.* **2001**, *240*, 391-399.

[15] Suzuki, S.; Kaneko, S.; Fujii, S.; Marqués-González, S.; Nishino, T.; Kiguchi, M., Effect of the Molecule-Metal Interface on the Surface-Enhanced Raman Scattering of 1,4-Benzenedithiol. *J. Phys. Chem. C* **2016**, *120*, 1038-1042.

[16] Zhang, Q.; Blom, D. A.; Wang, H., Nanoporosity-Enhanced Catalysis on Subwavelength Au Nanoparticles: A Plasmon-Enhanced Spectroscopic Study. *Chem. Mater.* **2014**, *26*, 5131-5142.

[17] Zhao, L.; Chen, J.-L.; Zhang, M.; Wu, D.-Y.; Tian, Z.-Q., Theoretical Study on Electroreduction of *p*-Nitrothiophenol on Silver and Gold Electrode Surfaces. *J. Phys. Chem. C* **2015**, *119*, 4949-4958.

[18] Gajdoš, M.; Eichler, A.; Hafner, J., CO Adsorption on Close-Packed Transition and Noble Metal Surfaces: Trends from *ab initio* Calculations. *J. Phys. Condens. Matter* **2004**, *16*, 1141-1164.

[19] Robertson, M. J.; Angelici, R. J., Adsorption of Aryl and Alkyl Isocyanides on Powdered Gold. *Langmuir* **1994**, *10*, 1488-1492.

[20] Kim, K.; Kim, K. L.; Choi, J.-Y.; Lee, H. B.; Shin, K. S., Surface Enrichment of Ag Atoms in Au/Ag Alloy Nanoparticles Revealed by Surface-Enhanced Raman Scattering of 2,6-Dimethylphenyl Isocyanide. *J. Phys. Chem. C* **2010**, *114*, 3448-3453.

[21] López-Tobar, E.; Hara, K.; Izquierdo-Lorenzo, I.; Sanchez-Cortes, S., Plasmonic Effects of Phenylenediisocyanides Linked at Interparticle Junctions of Metal Nanoparticles. *J. Phys. Chem. C* **2014**, *119*, 599-609.

[22] Gruenbaum, S. M.; Henney, M. H.; Kumar, S.; Zou, S., Surface-Enhanced Raman Spectroscopic Study of 1,4-Phenylene Diisocyanide Adsorbed on Gold and Platinum-Group Transition Metal Electrodes. *J. Phys. Chem. B* **2006**, *110*, 4782-4792.

[23] Hu, J.; Tanabe, M.; Sato, J.; Uosaki, K.; Ikeda, K., Effects of Atomic Geometry and Electronic Structure of Platinum Surfaces on Molecular Adsorbates Studied by Gap-Mode SERS. *J. Am. Chem. Soc.* **2014**, *136*, 10299-10307.

[24] Hu, J.; Hoshi, N.; Uosaki, K.; Ikeda, K., Vibrational Spectroscopic Observation of Atomic-Scale Local Surface Sites Using Site-Selective Signal Enhancement. *Nano Lett.* **2015**, *15*, 7982-7986.

[25] Bradshaw, A. M.; Hoffmann, F. M., The Chemisorption of Carbon Monoxide on Palladium Single Crystal Surfaces: IR Spectroscopic Evidence for Localised Site Adsorption. *Surf. Sci.* **1978**, *72*, 513-535.

[26] Unterhalt, H.; Rupprechter, G.; Freund, H.-J., Vibrational Sum Frequency Spectroscopy on Pd(111) and Supported Pd Nanoparticles: CO Adsorption from Ultrahigh Vacuum to Atmospheric Pressure. *J. Phys. Chem. B* **2002**, *106*, 356-367.

[27] Zeinalipour-Yazdi, C. D.; Willock, D. J.; Thomas, L.; Wilson, K.; Lee, A. F., CO Adsorption over Pd Nanoparticles: A General Framework for IR Simulations on Nanoparticles. *Surf. Sci.* **2016**, *646*, 210-220.

[28] Zhang, Q.; Li, W.; Wen, L.-P.; Chen, J.; Xia, Y., Facile Synthesis of Ag Nanocubes of 30 to 70 nm in Edge Length with CF_3COOAg as a Precursor. *Chem. Eur. J.* **2010**, *16*, 10234-10239.

[29] Li, J.; Liu, J.; Yang, Y.; Qin, D., Bifunctional Ag@Pd-Ag Nanocubes for Highly Sensitive Monitoring of Catalytic Reactions by Surface-Enhanced Raman Spectroscopy. *J. Am. Chem. Soc.* **2015**, *137*, 7039-7042.

[30] Li, J.; Sun, X.; Qin, D., Ag-Enriched Ag-Pd Bimetallic Nanoframes and Their Catalytic Properties. *ChemNanoMat* **2016**, *2*, 494-499.

[31] Li, J.; Wu, Y.; Sun, X.; Liu, J.; Winget, S. A.; Qin, D., A Dual Catalyst with SERS Activity for Probing Stepwise Reduction and Oxidation Reactions. *ChemNanoMat* **2016**, *2*, 786-790.

[32] Wu, Y.; Sun, X.; Yang, Y.; Li, J.; Zhang, Y.; Qin, D., Enriching Silver Nanocrystals with a Second Noble Metal. *Acc. Chem. Res.* **2017**, *50*, 1774-1784.

[33] Bae, S. C.; Lee, H.; Lin, Z.; Granick, S., Chemical Imaging in a Surface Forces Apparatus: Confocal Raman Spectroscopy of Confined Poly(dimethylsiloxane). *Langmuir* **2005**, *21*, 5685-5688.

[34] Mammone, J.; Sharma, S.; Nicol, M., Raman Spectra of Methanol and Ethanol at Pressures up to 100 kbar. *J. Phys. Chem.* **1980**, *84*, 3130-3134.

[35] Yang, T.-H.; Peng, H.-C.; Zhou, S.; Lee, C.-T.; Bao, S.; Lee, Y.-H.; Wu, J.-M.; Xia, Y., Toward a Quantitative Understanding of the Reduction Pathways of a Salt Precursor in the Synthesis of Metal Nanocrystals. *Nano Lett.* **2017**, *17*, 334-340.

CHAPTER 5. CONCLUSIONS AND FUTURE DIRECTIONS

5.1 Conclusions

This dissertation documents the development of synthetic strategies to enrich Ag nanocrystals with a second metal such as Pd or Au for the generation of Ag@Pd-Ag core-frame bimetallic nanocubes or Ag@SiO_2/Au nanoparticles, respectively. By using the synthesis of Ag@Pd core-frame nanocubes as a model reaction system, we discovered the use of 2,6-dimethylphenyl isocyanide (2,6-DMPI) as a spectroscopic probe to study the heterogeneous nucleation and deposition of Pd on Ag nanocubes under different conditions by surface-enhanced Raman scattering (SERS). This *in situ* technique provided opportunity to investigate the roles played by reaction temperature and the type of Pd(II) precursor in influencing the heterogeneous nucleation and growth of bimetallic nanocrystals. The sensitivity of isocyanide group to Pd atoms helps elucidate some of the details on the reduction, deposition, and diffusion processes involved in heterogeneous nucleation. We further demonstrated that Ag@Pd core-frame bimetallic nanocubes and Ag@SiO_2/Au nanoparticles embrace integrated plasmonic and catalytic properties, making them an ideal bifunctional probe to monitor catalytic reactions by *in situ* SERS.

In the typical synthesis of Ag@Pd-Ag nanocubes, we co-titrated Na_2PdCl_4 and $AgNO_3$ into an aqueous suspension of Ag nanocubes in the presence of ascorbic acid (H_2Asc, reductant) and poly(vinyl pyrrolidone) (PVP, a colloidal stabilizer) at pH = 3.2 under ambient condition. It was found that the galvanic replacement between Ag nanocubes and Na_2PdCl_4 could be effectively inhibited because of the involvement of Ag^+ ions and H_2Asc, leading to the co-deposition of Pd and Ag atoms on the surfaces of Ag

nanocubes. By simply increasing the titration volume of precursor solutions added into the reaction system, Pd and Ag atoms would be progressively deposited on the edges, corners, and then side faces of Ag nanocubes in the site-by-site manner. Remarkably, catalytic activity of as-obtained Ag@Pd-Ag nanocubes could be precisely controlled by varying the amount of Pd atoms being deposited on the surfaces of nanocubes. With the inclusion of additional Ag, these Ag@Pd-Ag nanocubes embrace both LSPR and SERS properties similar to those of the original Ag cubes. By optimizing the ratio of Pd to Ag, we demonstrated the utility of Ag@Pd-Ag nanocubes as a dual catalyst for the stepwise conversion of 4-nitrothiophenol (4-NTP) to *trans*-4,4'-dimercaptoazobenzene (*trans*-DMAB) under ambient conditions. Our *in situ* SERS results reveal three sequential processes that include the Pd-catalyzed reduction of 4-NTP to 4-aminothiophenol (4-ATP) by hydrogen, a period during which the 4-ATP remains unaltered until all hydrogen has depleted, and the Ag-catalyzed oxidation of 4-ATP to *trans*-DMAB by the O_2 from air. This work will contribute to the development of an environment-friendly and sustainable approach to the production of aromatic azo compounds.

In the rational synthesis of Ag@SiO_2/Au nanoparticles with an "islands in the sea" configuration, we titrated $HAuCl_4$ solution into an aqueous suspension of Ag@SiO_2 core-shell nanocubes in the presence of NaOH, H_2Asc, and PVP at pH=11.9. The NaOH plays a critical role in creating small pores in the SiO_2 shell *in situ*, followed by the epitaxial growth of Au from the Ag surface through the pores, leading to the generation of Au islands immersed in a SiO_2 sea. By simply maneuvering the amount of $HAuCl_4$ titrated into the reaction system, the Au islands can be made to pass through and protrude from the SiO_2 shell, embracing catalytic activity toward the reduction of 4-nitrophenol (4-NP) to 4-

aminophenol (4-AP) by $NaBH_4$. Although the Ag in the core exhibits a strong SERS activity, the SiO_2 sea helps keep the Au component as compact, isolated, and stabilized islands. The $Ag@SiO_2$/Au nanoparticles can also serve as a bifunctional probe to monitor the stepwise Au-catalyzed reduction of 4-NTP to 4-ATP by $NaBH_4$ and Ag-catalyzed oxidation of 4-ATP to *trans*-DMAB by the O_2 from air in the same reaction system.

Building upon the prior success of Ag@Pd-Ag core-frame nanocubes, we turned the synthesis of core-frame nanocubes into a model system for investigating the fundamentals involved in the heterogeneous nucleation and overgrowth of metal nanocrystals. We demonstrated the use of 2,6-DMPI as a sensitive probe for *in situ* atomic-level tracking of the heterogeneous nucleation of Pd on Ag nanocubes by SERS. Because the isocyanide group binds to Ag and Pd *via* σ-donation and π-back donation, respectively, we can readily watch the deposition of Pd on Ag nanocubes by monitoring the distinctive stretching frequency of 2,6-DMPI, ν_{NC}, using SERS. Remarkably, we discovered that the isocyanide group could bind to one, two, and three adjacent Pd atoms to generate the atop, bridge, and hollow binding configurations, respectively, to exhibit different vibrational frequencies. These unique characteristics make it possible to use 2,6-DMPI as a distinctive reporter for characterizing Pd atoms being deposited onto edges, corners, and side faces of Ag nanocubes with different arrangements on these different facets. In a typical experiment, we followed a standard protocol to synthesize Ag-Pd nanocubes by adding Na_2PdCl_4 into the aqueous suspension of Ag nanocubes in the presence of H_2Asc, PVP, and 2,6-DMPI under ambient condition. We confirmed that the presence of 2,6-DMPI in the reaction solution does not alter the reduction of the precursor, neither the deposition pathway of Pd on Ag nanocubes. By withdrawing samples from reaction solution to collect SERS spectra

at different reaction time points, we demonstrated atomic-level dynamic tracking of heterogeneous nucleation of Pd on Ag nanocubes by monitoring the ν_{NC} bands through time-dependent SERS spectra. This *in situ* tracking method with atomic resolution allows us to investigate the roles played by reaction temperature and the type of Pd(II) precursor in affecting the heterogeneous nucleation and deposition of Pd on Ag nanocrystals. With further development, this technique will also support the rational synthesis of bimetallic nanocrystals involving other noble metals such as Ru, Rh, and Ir.

5.2 Future Directions

5.2.1 Revitalizing Silver Nanocrystals as a Catalyst toward Hydrogenation by Tuning the Electronic Structure with an Isocyanide-Based Compound

Heterogeneous catalysts play a vital role in the pharmaceutical, petrochemical and environmental industries, contributing to the production of more than 85% of all transportation chemicals and fuels. To achieve the production of desired chemicals at high yields while eliminating the production of wastes, it is of paramount importance to have highly active and selective catalysts.[1-2] Previous studies have established that the activity and selectivity of a catalyst can vary vastly depending on the size of the metal nanoparticles when their sizes drop below ~7 nm in diameter.[3] For metal nanocrystals with the same shape, they would present an increasingly larger fraction of low-coordination atoms on the surface as their sizes are reduced. The low-coordination atoms with fewer nearest neighbors would bind to the adsorbates more strongly, causing changes to the catalytic activity. On the other hand, many research groups have demonstrated the ability to engineer the shape of nanocrystals to present the most active and/or selective facet on the surface at

the greatest proportion and thus optimize the activity and/or selectivity of a catalyst.[4] The presence of a well-defined, single type of facet on the surface of a catalyst also makes it much easier to elucidate the reaction mechanism.[5]

In additional to both size and shape, one can also tailor the catalytic activity and selectivity of metal nanocrystals by controlling their interaction with the supporting materials.[6] It has been established that chemical bonding and the associated charge transfer at the interface between a metal nanocrystal and its support could be used to tune the electronic and chemical properties of the metal surface and thus achieve enhanced catalytic performance. To this end, Rodriguez *et al.* have demonstrated that the strong metal−support interaction between Pt nanoparticles and their ceria support could produce large electronic perturbations in the particles and thus significantly enhance the ability of the metal surface to dissociate the O−H bonds in water.[7] Neyman and Lidbuda performed experiments to confirm that the interactions of Pt nanoparticles with ceria could facilitate electron transfer from Pt particles to the support and oxygen transfer from ceria to Pt, contributing to the remarkable catalytic activities of this technologically important Pt-ceria catalysts.[8]

Conceptually, one can also create electronic perturbations to enhance catalytic performance by introducing organic modifiers to the surface of a heterogeneous catalyst.[9] Although organic ligands are often used to stabilize the particles during their synthesis, it has long been considered that the effect of the "leftover" organics could relentlessly "poison" the surface atoms, block the surface active sites, and ultimately deteriorate their catalytic performance. As a result, there are only a limited number of demonstrations with regard to the "positive" effects of surface ligands on the catalytic performance of metal nanocrystals. For example, the industrial Lindlar catalyst ($Pd/CaCO_3$) relies on a

combination of both organic (quinolone) and inorganic (lead) modifiers to enhance the hydrogenation selectivity of alkynes to alkene, without further hydrogenation to the undesirable alkane, through the surface coordination chemistry.[10] A few groups investigated the role of dendrimers,[11] chiral modifiers,[12] and polymers[13] in heterogeneous catalysts and they concluded that the catalytic performance could be extremely sensitive to the structure of the organic species. For example, Medlin and his co-workers used self-assembled monolayers (SAMs) to control the surface environment of Pd/Al_2O_3 catalysts.[14] They demonstrated that the SAMs could control catalytic selectivity by promoting the interaction between organic modifiers and reactants through active site selection, molecular recognition, and steric interaction. Most recently, Zheng and co-workers reported the use of ethylenediamine (EDA)-coated ultrathin Pt nanowires (EDA-Pt NWs) as a model system to demonstrate the interfacial electronic effect induced by an organic modifier for controlling the catalytic selectivity toward the hydrogenation of nitrobenzene.[15] Their findings clearly demonstrate that organic modifiers offer an effective and low-cost strategy for tailoring the electronic structure of metal nanocatalysts, and ultimately for optimizing the catalytic performance.

I propose to use isocyanide compounds to functionalize the surface of Ag nanocrystals and thus alter their catalytic properties. It is well-established that Ag nanocrystals are superior catalysts for oxidation reactions such as ethylene epoxidation, one of the key processes in the petroleum industry,[16-17] but they show limited catalytic activities toward reduction reactions. I propose to change the scenario by tailoring the electronic structure of the surface atoms through chemical modification. Specifically, I will use Ag nanocubes as a model catalyst and focus on the use of 2,6-DMPI and 1,4-phenylene

diisocyanide (1,4-PDI) as the organic modifiers. Because the binding of the isocyanide group (–NC) to a transition metal is similar to that of carbon monoxide (CO) due to their isoelectronic structure,[18-20] we expect to have σ-donation from the anti-bonding σ* orbital of the –NC group to the *d*-band of Ag. I hypothesize that such an electron transfer can make the Ag surface atoms highly electron rich to facilitate a hydrogenation reaction. During catalysis, such an interfacial electronic effect should also make the isocyanide-functionalized Ag nanocubes favor the adsorption of electron-deficient reactants over electron-rich substances, making it possible to tailor the reaction selectivity. On the other hand, the proposed interfacial electronic effect can be experimentally validated by probing the binding strength of the –NC group to Ag nanocubes using SERS.

I will use the hydrogenation of nitroaromatics as a model reaction to evaluate the catalytic performance of the isocyanide-functionalized Ag nanocubes. Specifically, I will investigate the catalytic performance of the isocyanide-functionalized Ag nanocubes toward the reduction of nitrobenzene (NB) with different types of side groups, including 4-nitrophenol (4-NP, with an electron-donating group), 4-fluoronitrobenzene (4-FNB, with an electron-accepting group), and 4-nitrothiophenol (4-NTP, with a binding group). For the reactions involving NB, 4-NP, and 4-FNB, I will separate and analyze the products using techniques such as UV-vis spectroscopy, gas chromatography-mass spectrometry (GC-MS), and nuclear magnetic resonance (NMR) spectroscopy. For the reduction of 4-NTP, I will introduce the reactant into a colloidal suspension of the isocyanide-functionalized Ag nanocubes and then collect SERS spectra at different time intervals. The data should provide "finger-prints" of the chemical species involved, offering mechanistic insights into the stepwise reduction. If successful, this research will lead to the development

of cost-effective catalysts based on Ag nanocrystals for hydrogenation reactions.

5.2.2 Catalytic Nanoreactors through Self-Assembly

Thanks to the progress in controlling the synthesis of colloidal metal nanocrystals, recent years has witnessed the successful development of bifunctional nanocrystals as a unique probe for investigating the mechanisms of catalytic reactions using SERS.[21-23] Although Au or Ag nanocrystals can serve as both catalytic and SERS substrates, one can greatly expand the range of catalytic reactions to be probed by depositing another metal such as Pt, Pd, Rh, and Ir on the surface of Au or Ag nanocrystals to generate bimetallic structures with dual functionality. To this end, many groups have made significant contributions to the fabrication and utilization of Au-M (M = Pt, Pd, and Ag) bimetallic nanocrystals, with Au in the core serving as a SERS substrate and Pd, Pt, or Ag in the shell (complete or incomplete) as a catalytic material.[24-26] All these nanocrystals were further exploited for characterizing the reduction of 4-NTP to 4-ATP by $NaBH_4$ *in situ* and in real time. On the other hand, our group has actively explored the fabrication and use of Ag@M (M=Pt, Pd, Au, and Rh) nanocubes with a core-frame, core-shell, or core-satellite structure for probing various catalytic reactions through SERS fingerprinting.[27-30] As a major advantage over the counterpart built upon a Au core, the system based on a Ag core offers a stronger plasmonic resonance and thus stronger SERS activity in the visible region because of the elimination of inter-band transition.[31] Despite the notable success in applying these bimetallic nanocrystals to monitor catalytic reactions *in situ* by SERS, it remains a grand challenge to unravel the reaction mechanisms due to the heterogeneity of such a catalyst in terms of composition, structure, and reactivity. Additionally, both the catalytic sites and SERS hot spots tend to undergo dynamic changes owing to the shape

instability of individual nanocrystals in a solution phase and the involvement of random aggregation among the particles. Overall, the ensemble-averaged data can hardly be used to elucidate the relationship between the performance and structure of a heterogeneous nanocatalyst.

Here I propose to address the challenge by developing bifunctional nanoreactors from Ag nanocubes through surface functionalization and self-assembly. Molecules bearing di-isocyanide end groups can selectively bind to the Ag atoms of nanocubes, serving as *"*clips*"* to bring two such nanocubes together through self-assembly. The gap region between the two nanocubes can serve as a catalytic nanoreactor (Figure 5.1A), in which Ag atoms will be functionalized with thiol-based reactants for a variety of catalytic reactions. Owing to a strong plasmonic coupling between two Ag nanocubes separated by 1-3 nm, the catalytic nanoreactor naturally offers a SERS hot spot (Figure 5.1B) for monitoring catalytic reactions *in situ* by SERS fingerprinting. As a proof of concept, I will use the hydrogenation of an aromatic nitro compound to produce thermodynamically unfavorable but industrially important compounds such as hydroxylamine and azo compounds to demonstrate the premise of such catalytic nanoreactors in enabling chemical transformations of industrial value.[32] Currently, the commercial production of azo compounds requires stoichiometric amounts of environmentally unfriendly metals or nitrites.[33] There is an urgent need to develop a new catalytic system capable of effectively reducing nitroaromatics to azo compounds. Altogether, this research will not only enable real-time characterization of catalytic reactions based on SERS fingerprinting but also shed light on the rational design of new or improved catalytic materials.

I will leverage di-isocyanide with different lengths as a molecular linker to "glue"

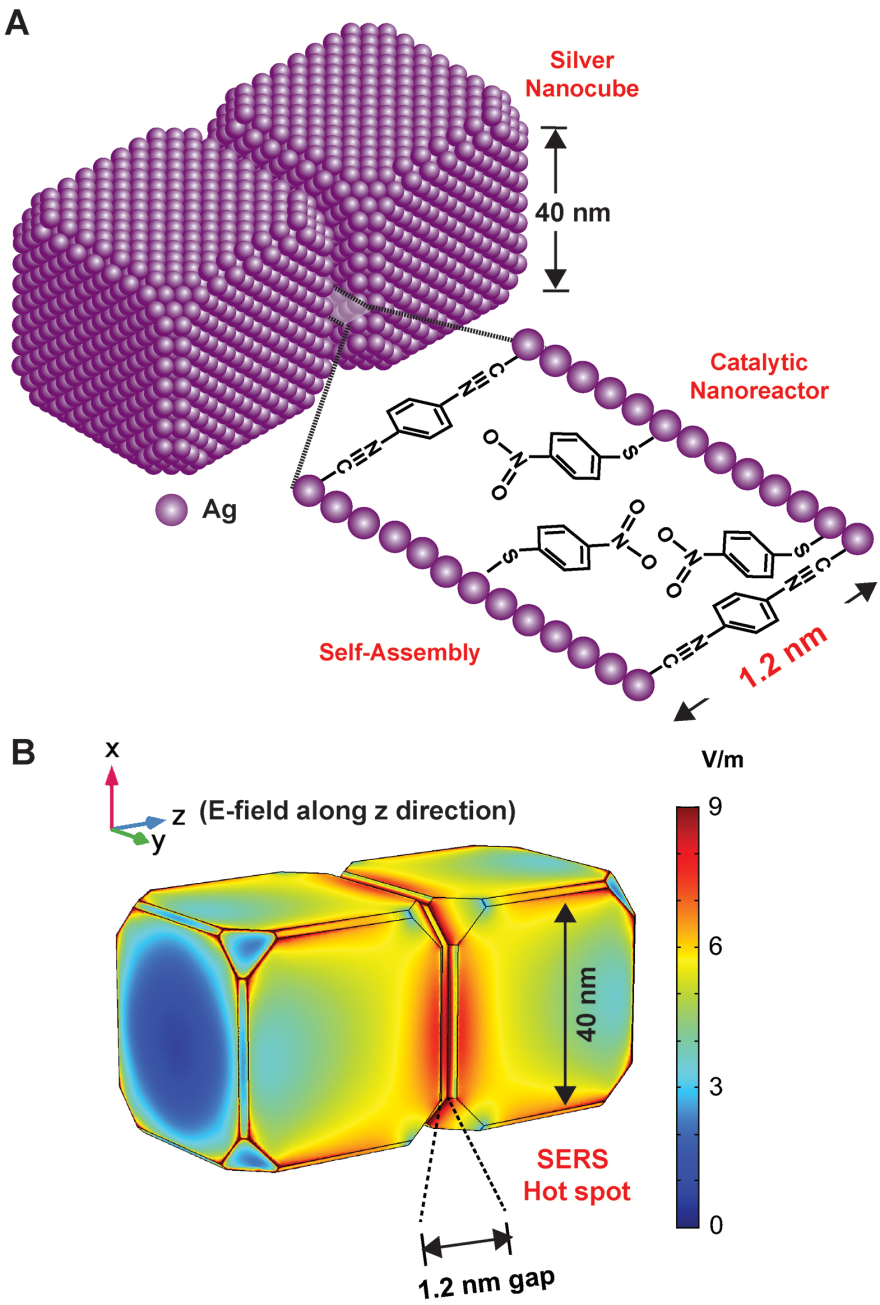

Figure 5.1. (A) Schematic of a catalytic nanoreactor fabricated using self-assembly. (B) The nanoreactor will also support a hot spot for analyzing the catalytic reaction by SERS.

together two Ag nanocubes.[34] This linker offers a number of unique features. Firstly, its molecular structure can be made with a rigid and linear phenylene backbone, making it ideal for creating nanoreactors with a tightly controlled gap between the two Ag side faces.[35] Secondly, it is well-established that the binding of isocyanide group (–NC) to a transition metal is similar to that of carbon monoxide (CO) because of their isoelectronic structure.[18-20] In principle, σ-donation from the anti-bonding σ* orbital of –NC group to the *d*-band of Ag would strengthen the NC bond, resulting in a blue shift for ν_{NC}.[36] Thirdly, I hypothesize that isocyanide group will weakly bind to Ag *via* σ-donation, making it feasible for molecules bearing thiol end groups to selectively displace isocyanide group on the surface of Ag.

The proposed bifunctional nanoreactors share the same operating principle as tip-enhanced Raman spectroscopy (TERS).[37] In TERS, an atomic force microscopy (AFM) tip covered by a thin layer of Ag or Au is typically used to enhance the Raman signal while serving as a catalyst. If the tip is positioned in proximity to a metal substrate, such as an atomically flat Au film, the gap between the tip and the substrate can induce strong Raman scattering at the apex of the tip where the catalytic site is located.[38] In 2012, Weckhuysen and co-workers used TERS to investigate photocatalytic reduction by placing the tip in contact with a monolayer of 4-NTP on a Au nanoplate.[39] Their success provides a strong motivation and support for the proposed work. The proposed nanoreactors, however, offer a number of advantages over TERS for investigating catalytic reactions in real time. First of all, the approach based on orthogonal functionalization and self-assembly allows one to fabricate millions of essentially identical nanoreactors simultaneously in a solution phase rather than just one nanoreactor between a AFM tip and a substrate in the dry state.

Secondly, when the two Ag nanocubes are separated by a di-isocyanide linker of *ca.* 1 nm in length, the volume of the nanoreactor can be as large as 1600 nm^3. In comparison, the detection volume of TERS is not well-defined due to the curvature of an AFM tip. By approximating the apex of an AFM tip as a sphere with a diameter of *ca.* 10 nm and only 1/15 of its surface contributes to the creation of a 1 nm gap with the substrate, the detection volume will only be 21 nm^3. As such, the proposed nanoreactors will be able to accommodate a broader range of reactants with different sizes while retaining the high detection sensitivity of TERS. Thirdly, different di-isocyanide linkers can be used to control the gap between the side faces of two nanocubes with a precision as high as 0.3 nm (the size of a benzene ring) to help optimize the detection sensitivity and volume. In TERS, although it is possible to maneuver the position of the AFM tip and thus alter the gap, it remains a challenge to achieve sub-nm precision. Finally, since the proposed nanoreactors are fabricated in the solution phase *via* orthogonal adsorption of different molecules, the catalytic reactions can be executed and monitored in a liquid phase to potentially resolve the molecular orientation during the course of a catalytic reaction. In contrast, TERS measurement is often conducted with a dry sample. Different from the dimers of Ag nanocrystals reported in literature,[40-42] the Ag surface in the proposed nanoreactors are still available for the adsorption of thiol-based reactants and thereby the execution of various catalytic reactions while the reactants, intermediates, and products can all be scrutinized *in situ* through SERS fingerprinting.

I will characterize catalytic reactions in the nanoreactors through SERS fingerprinting. The size of the nanoreactor, or more precisely, the separation between the two Ag side faces in a nanoreactor will be tuned to optimize the SERS detection sensitivity

while accommodating reactants with different sizes. Specifically, I will evaluate their performance toward the hydrogenation of 4-NTP. As a major advantage of such catalytic nanoreactors, the SERS analysis can be conducted while the particles are suspended in ethanol, making it feasible for real-time measurement. I will use ethanol as the solvent because *i*) most of thiol and isocyanide molecules are soluble in ethanol; and *ii*) the Raman bands of ethanol can serve as an internal reference for *in situ* SERS measurements.

As a major disadvantage of previous studies in the SERS monitoring catalytic reactions, the samples have to go through multiple steps of centrifugation and washing prior to SERS measurements. As such, the particles tend to aggregate to generate random hot spots during sample preparation, making it very difficult to specify the surface on which the chemical reaction occurs. In the proposed study, I will address this issue by switching to catalytic nanoreactors with well-defined side faces of Ag nanocubes. I will also develop a standard protocol for monitoring a reaction *in situ* through SERS fingerprinting. In a typical procedure, I will first prepare an ethanol solution of PDI (10^{-5} M), followed by the introduction of the Ag nanocubes to reach a final concentration of 2×10^{11} particles/mL. After 5 min, an aliquot of 25 μL will be withdrawn from the suspension for SERS analysis. Another SERS spectrum will be collected at $t = 60$ min, and then I will introduce an ethanol solution of 4-NTP (10^{-5} M in concentration). Afterward, an aliquot of 25 μL will be quickly withdrawn from the mixture at different time intervals and subjected to SERS analysis. For SERS measurement, I will fabricate the sample cell by punching a hole, which can hold 25 μL of liquid, in the surface of a polydimethylsiloxane (PDMS) block and having it mounted on a glass slide. Upon the addition of liquid sample, the cell will be carefully covered with a glass coverslip of 0.17 mm in thickness to prevent solvent evaporation. The top surface

of the coverslip can also serve as a reference point, from which the focal plane will be positioned at 0.2 mm into the sample, to aid SERS collection. I will use a 5x objective lens, a laser power of 5 mW for the 532 mn laser, and a collection time of 10 s. Specifically, I will focus on the following two tasks:

Task 1. *I will investigate the role of PDI on the surface of Ag nanocubes in controlling the partial hydrogenation of an aromatic nitro compound by SERS fingerprinting.* Based on the electrochemical model proposed by Haber,[43-44] there are two distinct routes for the hydrogenation of an aromatic nitro compound. In the direct route, the aromatic nitro compound is sequentially reduced to a nitroso compound, hydroxylamine, and finally an aniline derivative. Alternatively, in the indirect route, the nucleophilic hydroxylamine can react with the electrophilic nitroso to produce an azoxy compound, followed by consecutive steps for the formation of azo, hydrazo, and aniline compounds. In this study, I hypothesize that the interfacial electronic effect arising from the modification of Ag atoms of Ag nanocubes by isocyanide group can control the selectivity for the partial hydrogenation of 4-NTP. Because the binding of isocyanide group to Ag relies on the σ-donation from the anti-bonding σ∗ orbital of the isocyanide group to the *d*-band of Ag, I argue that the Ag atoms on the surface will become highly electron enriched and thus accelerate the reduction of an aromatic nitro compound, making it possible to capture the intermediate products such as nitroso, hydroxylamine, and/or azo compounds. During the catalytic reaction, such an interfacial electronic effect should also make the isocyanide-functionalized Ag nanocubes more favorable for the adsorption of different intermediate species, making it possible to optimize the reaction selectivity.

Task 2. *I will investigate the role of photochemical transformation of 4-NTP in the*

nanoreactors. Because the enormously enhanced electromagnetic field is highly localized in the junction between the two Ag nanocubes, the adsorbed molecules can interact with the excited electrons on the surface, as well as with the enhanced field above the surface. Although photochemistry caused by direct molecular excitation on metal surface is normally quenched by the extremely fast rate of molecular excited-state energy transfer to the metal,[45] in some cases, the adsorbed molecules can still undergo photochemical transformation due to optical excitation of electrons on the metal surface, in additional to the SERS effect. As demonstrated by Henglein,[46-47] the exchange and charge-transfer surface electronic processes proposed to account for chemical enhancement of SERS are closely related to the known electrochemical reactivity and photoreactivity of Ag nanocrystals.[48-49] In these studies, it was shown that the Fermi level of Ag would exhibit a shift proportional to the partial charge involved in molecule adsorption, leading to the generation of adsorption-induced polarization at the metal-molecule interface that has a similar effect to that of a voltage applied to an electrode. As a result, it would become easier to oxidize Ag while it would become easier to reduce the adsorbate. Herein, I will evaluate the roles of different excitation wavelength of lasers and the power of incident lasers in affecting the catalytic performance of the nanoreactors for the reduction of 4-NTP by *in situ* SERS. It is expected that the photochemical transformation will be significantly attenuated at an excitation wavelength of 785 nm or at an extremely low power of incident light as very few charge carriers will be generated to instigate the photochemical reactions. A direct comparison of these two sets of data will shed light on the role of gap in controlling the photochemical transformation of 4-NTP.

5.3 Notes to Chapter 5

Part of the chapter is adapted from the article "Enriching Silver Nanocrystals with a Second Noble Metal" published in *Accounts of Chemical Research*.

5.4 References

[1] Somorjai, G. A.; Rioux, R. M, High Technology Catalysts towards 100% Selectivity: Fabrication, Characterization and Reaction Studies. *Catal. Today* **2005,** *100*, 201-215.

[2] Noyori, R., Synthesizing Our Future. *Nat. Chem.* **2009,** *1*, 5-6.

[3] Bell, A. T., The Impact of Nanoscience on Heterogeneous Catalysis. *Science* **2003,** *299*, 1688-1691.

[4] Xie, S.; Choi, S.-I.; Xia, X.; Xia, Y., Catalysis on Faceted Noble-Metal Nanocrystals: Both Shape and Size Matter. *Curr. Opin. Chem. Eng.* **2013,** *2*, 142-150.

[5] Roldan Cuenya, B., Metal Nanoparticle Catalysts Beginning to Shape-up. *Acc. Chem. Res.* **2013,** *46*, 1682-1691.

[6] Campbell, C. T., Catalyst-Support Interactions: Electronic Perturbations. *Nat. Chem.* **2012,** *4*, 597-598.

[7] Bruix, A.; Rodriguez, J. A.; Ramírez, P. J.; Senanayake, S. D.; Evans, J.; Park, J. B.; Stacchiola, D.; Liu, P.; Hrbek, J.; Illas, F., A New Type of Strong Metal-Support Interaction and the Production of H_2 through the Transformation of Water on $Pt/CeO_2(111)$ and $Pt/CeO_x/TiO_2(110)$ Catalysts. *J. Am. Chem. Soc.* **2012,** *134*, 8968-8974.

[8] Vayssilov, G. N.; Lykhach, Y.; Migani, A.; Staudt, T.; Petrova, G. P.; Tsud, N.; Skála, T.; Bruix, A.; Illas, F.; Prince, K. C.; Matolín, V.; Neyman, K. M.; Libuda, J., Support Nanostructure Boosts Oxygen Transfer to Catalytically Active Platinum Nanoparticles. *Nat. Mater.* **2011,** *10*, 310-315.

[9] Liu, P.; Qin, R.; Fu, G.; Zheng, N., Surface Coordination Chemistry of Metal Nanomaterials. *J. Am. Chem. Soc.* **2017,** *139*, 2122-2131.

[10] García-Mota, M.; Gómez-Díaz, J.; Novell-Leruth, G.; Vargas-Fuentes, C.; Bellarosa,

L.; Bridier, B.; Pérez-Ramírez, J.; López, N., A Density Functional Theory Study of the 'Mythic' Lindlar Hydrogenation Catalyst. *Theor. Chem. Acc.* **2011,** *128*, 663-673.

[11] Gross, E.; Liu, J. H.-C.; Toste, F. D.; Somorjai, G. A., Control of Selectivity in Heterogeneous Catalysis by Tuning Nanoparticle Properties and Reactor Residence Time. *Nat. Chem.* **2012,** *4*, 947-952.

[12] Han, D.; Li, X.; Zhang, H.; Liu, Z.; Li, J.; Li, C., Heterogeneous Asymmetric Hydroformylation of Olefins on Chirally Modified Rh/SiO_2 Catalysts. *J. Catal.* **2006,** *243*, 318-328.

[13] Feng, B.; Hou, Z.; Yang, H.; Wang, X.; Hu, Y.; Li, H.; Qiao, Y.; Zhao, X.; Huang, Q., Functionalized Poly (ethylene glycol)-Stabilized Water-Soluble Palladium Nanoparticles: Property/Activity Relationship for the Aerobic Alcohol Oxidation in Water. *Langmuir* **2010,** *26*, 2505-2513.

[14] Schoenbaum, C. A.; Schwartz, D. K.; Medlin, J. W., Controlling the Surface Environment of Heterogeneous Catalysts Using Self-Assembled Monolayers. *Acc. Chem. Res.* **2014,** *47*, 1438-1445.

[15] Chen, G.; Xu, C.; Huang, X.; Ye, J.; Gu, L.; Li, G.; Tang, Z.; Wu, B.; Yang, H.; Zhao, Z.; Zhou, Z.; Fu, G.; Zheng, N., Interfacial Electronic Effects Control the Reaction Selectivity of Platinum Catalysts. *Nat. Mater.* **2016,** *15*, 564-569.

[16] Linic, S.; Piao, H.; Adib, K.; Barteau, M. A., Ethylene Epoxidation on Ag: Identification of the Crucial Surface Intermediate by Experimental and Theoretical Investigation of its Electronic Structure. *Angew. Chem., Int. Ed.* **2004**, *43*, 2918-2921.

[17] Kirk, R. E.; Othmer, D. F., *Encyclopedia of Chemical Technology*, 4th ed.; Wiley: New York, 1994; Vol. 9, p. 915.

[18] Gajdoš, M.; Eichler, A.; Hafner, J., CO Adsorption on Close-Packed Transition and Noble Metal Surfaces: Trends from ab initio Calculations. *J. Phys.: Condens. Matter* **2004,** *16*, 1141-1164.

[19] Robertson, M. J.; Angelici, R. J., Adsorption of Aryl and Alkyl Isocyanides on Powdered Gold. *Langmuir* **1994,** *10*, 1488-1492.

[20] Gruenbaum, S. M.; Henney, M. H.; Kumar, S.; Zou, S., Surface-Enhanced Raman

Spectroscopic Study of 1,4-Phenylene Diisocyanide Adsorbed on Gold and Platinum-Group Transition Metal Electrodes. *J. Phys. Chem. B* **2006,** *110*, 4782-4792.

[21] Zhang, Y.; Wu, Y.; Qin, D., Rational Design and Synthesis of Bifunctional Metal Nanocrystals for Probing Catalytic Reactions by Surface-Enhanced Raman Scattering. *J. Mater. Chem. C* **2018,** *6*, 5353-5362.

[22] Xie, W.; Schlücker, S., Surface-Enhanced Raman Spectroscopic Detection of Molecular Chemo-and Plasmo-Catalysis on Noble Metal Nanoparticles. *Chem. Commun.* **2018,** *54*, 2326-2336.

[23] Wu, Y.; Sun, X.; Yang, Y.; Li, J.; Zhang, Y.; Qin, D., Enriching Silver Nanocrystals with a Second Noble Metal. *Acc. Chem. Res.* **2017,** *50*, 1774-1784.

[24] Huang, J.; Zhu, Y.; Lin, M.; Wang, Q.; Zhao, L.; Yang, Y.; Yao, K. X.; Han, Y., Site-Specific Growth of Au-Pd Alloy Horns on Au Nanorods: A Platform for Highly Sensitive Monitoring of Catalytic Reactions by Surface Enhancement Raman Spectroscopy. *J. Am. Chem. Soc.* **2013,** *135*, 8552-8561.

[25] Jing, H.; Zhang, Q.; Large, N.; Yu, C.; Blom, D. A.; Nordlander, P.; Wang, H., Tunable Plasmonic Nanoparticles with Catalytically Active High-Index Facets. *Nano Lett.* **2014,** *14*, 3674-3682.

[26] Jing, H.; Wang, H., Structural Evolution of Ag-Pd Bimetallic Nanoparticles through Controlled Galvanic Replacement: Effects of Mild Reducing Agents. *Chem. Mater.* **2015,** *27*, 2172-2180.

[27] Zhang, Z.; Ahn, J.; Kim, J.; Wu, Z.; Qin, D., Facet-Selective Deposition of Au and Pt on Ag Nanocubes for the Fabrication of Bifunctional Ag@Au-Pt Nanocubes and Trimetallic Nanoboxes. *Nanoscale* **2018,** *10*, 8642-8649.

[28] Zhang, J.; Winget, S. A.; Wu, Y.; Su, D.; Sun, X.; Xie, Z.-X.; Qin, D., Ag@Au Concave Cuboctahedra: A Unique Probe for Monitoring Au-Catalyzed Reduction and Oxidation Reactions by Surface-Enhanced Raman Spectroscopy. *ACS nano* **2016,** *10*, 2607-2616.

[29] Li, J.; Liu, J.; Yang, Y.; Qin, D., Bifunctional Ag@Pd-Ag Nanocubes for Highly Sensitive Monitoring of Catalytic Reactions by Surface-Enhanced Raman Spectroscopy. . *Am. Chem. Soc.* **2015,** *137*, 7039-7042.

[30] Zhang, Y.; Ahn, J.; Liu, J.; Qin, D., Syntheses, Plasmonic Properties, and Catalytic Applications of Ag-Rh Core-Frame Nanocubes and Rh Nanoboxes with Highly Porous Walls. *Chem. Mater.* **2018,** *30*, 2151-2159.

[31] Beversluis, M. R.; Bouhelier, A.; Novotny, L., Continuum Generation from Single Gold Nanostructures through Near-Field Mediated Intraband Transitions. *Phys. Rev. B* **2003,** *68*, 115433.

[32] Ohe, K.; Uemura, S.; Sugita, N.; Masuda, H.; Taga, T., Sodium Arenetellurolate-Catalyzed Selective Conversion of Nitro Aromatics to Aromatic Azoxy or Azo Compounds and its Application for Facile Preparation of 3,3'- and 4,4'-bis[β-(Aryltelluro) vinyl]azobenzenes from (3- and 4-Nitrophenyl)acetylenes. *J. Org. Chem.* **1989,** *54*, 4169-4174.

[33] Grirrane, A.; Corma, A.; García, H., Gold-Catalyzed Synthesis of Aromatic Azo Compounds from Anilines and Nitroaromatics. *Science* **2008,** *322*, 1661-1664.

[34] López-Tobar, E.; Hara, K.; Izquierdo-Lorenzo, I.; Sanchez-Cortes, S., Plasmonic Effects of Phenylenediisocyanides Linked at Interparticle Junctions of Metal Nanoparticles. *J. Phys. Chem. C* **2014,** *119*, 599-609.

[35] Brus, L., Noble Metal Nanocrystals: Plasmon Electron Transfer Photochemistry and Single-Molecule Raman Spectroscopy. *Acc. Chem. Res.* **2008,** *41*, 1742-1749.

[36] Hu, J.; Tanabe, M.; Sato, J.; Uosaki, K.; Ikeda, K., Effects of Atomic Geometry and Electronic Structure of Platinum Surfaces on Molecular Adsorbates Studied by Gap-Mode SERS. *J. Am. Chem. Soc.* **2014,** *136*, 10299-10307.

[37] Verma, P., Tip-Enhanced Raman Spectroscopy: Technique and Recent Advances. *Chem. Rev.* **2017,** *117*, 6447-6466.

[38] Zhong, J.-H.; Jin, X.; Meng, L.; Wang, X.; Su, H.-S.; Yang, Z.-L.; Williams, C. T.; Ren, B., Probing the Electronic and Catalytic Properties of a Bimetallic Surface with 3 nm Resolution. *Nat. Nanotechnol.* **2017,** *12*, 132-136.

[39] van Schrojenstein Lantman, E. M.; Deckert-Gaudig, T.; Mank, A. J.; Deckert, V.; Weckhuysen, B. M., Catalytic Processes Monitored at the Nanoscale with Tip-Enhanced Raman Spectroscopy. *Nat. Nanotechnol.* **2012,** *7*, 583-586.

[40] Gao, B.; Arya, G.; Tao, A. R., Self-Orienting Nanocubes for the Assembly of Plasmonic Nanojunctions. *Nat. Nanotechnol.* **2012,** *7*, 433-437.

[41] Gurunatha, K. L.; Marvi, S.; Arya, G.; Tao, A. R., Computationally Guided Assembly of Oriented Nanocubes by Modulating Grafted Polymer–Surface Interactions. *Nano Lett.* **2015,** *15*, 7377-7382.

[42] Li, W.; Camargo, P. H.; Lu, X.; Xia, Y., Dimers of Silver Nanospheres: Facile Synthesis and Their Use as Hot Spots for Surface-Enhanced Raman Scattering. *Nano Lett.* **2008,** *9*, 485-490.

[43] Haber, F.; Schmidt, C., The Reduction Procedure with the Electrical Reduction of the Nitrobenzene. *Z. Phys. Chem* **1900,** *32*, 271-287.

[44] Haber, F., Gradual Electrolytic Reduction of Nitrobenzene with Limited Cathode Potential. *Elektrochem. Angew. Phys. Chem.* **1898,** *22*, 506-514.

[45] Nitzan, A.; Brus, L. E., Theoretical Model for Enhanced Photochemistry on Rough Surfaces. *J. Chem. Phys.* **1981,** *75*, 2205-2214.

[46] Gutierrez, M.; Henglein, A., Formation of Colloidal Silver by "Push-Pull" Reduction of Ag^{+}. *J. Phys. Chem.* **1993,** *97*, 11368-11370.

[47] Mulvaney, P.; Linnert, T.; Henglein, A., Surface Chemistry of Colloidal Silver in Aqueous Solution: Observations on Chemisorption and Reactivity. *J. Phys. Chem.* **1991,** *95*, 7843-7846.

[48] Laufer, G.; Huneke, J. T.; Schaaf, T. F., Surface Enhanced Raman Spectroscopy of Cyanide Complexes on Silver Surfaces. *Chem. Phys. Lett.* **1981,** *82*, 571-576.

[49] Persson, B., On the Theory of Surface-Enhanced Raman Scattering. *Chem. Phys. Lett.* **1981,** *82*, 561-565.